High Field Suppression of Bremsstrahlung Emission in High-Intensity Laser-Plasma Interactions

Inaugural-Dissertation

zur Erlangung des Doktorgrades
der Mathematisch-Naturwissenschaftlichen Fakultät
der Heinrich-Heine-Universität Düsseldorf

vorgelegt von

Mahdi Habibi
aus Mashhad, Iran

Düsseldorf, Oktober 2023

Aus dem Institut für Strahlenphysik
des Helmholtz-Zentrum Dresden-Rossendorf

Gedruckt mit der Genehmigung der
Mathematisch-Naturwissenschaftlichen Fakultät der
Heinrich-Heine-Universität Düsseldorf

Berichterstatter:

1. PD. Toma Toncian

2. Prof. Götz Lehmann

Tag der mündlichen Prüfung: 06/10/2023

Dedication

To my loves
Forough and Hannah

Declaration

I declare under oath that I have produced my thesis independently and without any undue assistance by third parties under consideration of the 'Principles for the Safeguarding of Good Scientific Practice at Heinrich Heine University Düsseldorf'.

Abstract

This dissertation investigates the effect of macroscopic electric and magnetic fields on bremsstrahlung emission in high-intensity laser-plasma interactions, specifically in the regime of relativistic-induced transparency. The Particle-in-Cell (PIC) EPOCH simulation code has been updated to incorporate a new suppression mechanism influenced by the presence of intense electric and magnetic fields. The study compared the bremsstrahlung emissions generated under relativistic transparency conditions using three distinct models: the original bremsstrahlung model in the EPOCH code, the model modified by the magnetic suppression (MS) effect, and the newly proposed suppression model by the electric and magnetic suppression (EMS) effect. The results demonstrated that macroscopic electric and magnetic fields have a significant effect on the decrease of bremsstrahlung photons in laser-plasma interactions. In addition, differences in electron dynamics were observed between the EPOCH and EMS models, indicating that the suppression mechanism can influence the dynamics of electron acceleration. The study provides insight into bremsstrahlung emission under extreme conditions, where energetic electrons travel through a relativistically transparent plasma while being deflected by magnetic fields with MT[†]-level strength. On the basis of the results, it is suggested that the implementation of conventional bremsstrahlung in PIC codes be modified to account for the discussed suppression effect.

[†]MT: Mega Tesla

Zusammenfassung

In dieser Dissertation wird die Wirkung makroskopischer elektrischer und magnetischer Felder auf die Bremsstrahlung bei hochintensiven Laser-Plasma-Wechselwirkungen untersucht, insbesondere im Regime der relativistisch-induzierten Transparenz. Der Particle-in-Cell (PIC) EPOCH Simulationscode wurde angepasst, um einen neuen Unterdrückungsmechanismus zu integrieren, der durch das Vorhandensein von intensiven elektrischen und magnetischen Feldern beeinflusst wird. In der Studie wurden die unter relativistischen Transparenzbedingungen erzeugten Bremsstrahlungsemissionen mit drei verschiedenen Modellen verglichen: dem ursprünglichen Bremsstrahlungsmodell im EPOCH-Code, dem durch den magnetischen Unterdrückungseffekt (MS) modifizierten Modell und dem neu vorgeschlagenen Unterdrückungsmodell durch elektrischen und magnetischen Felder (EMS). Die Ergebnisse zeigen, dass makroskopische elektrische und magnetische Felder einen signifikanten Einfluss auf die Erzeugung der Bremsstrahlung in Laser-Plasma-Wechselwirkungen haben. Darüber hinaus wurden Unterschiede in der Elektronendynamik zwischen den EPOCH- und EMS-Modellen beobachtet, was darauf hinweist, dass der Unterdrückungsmechanismus die Dynamik der Elektronenbeschleunigung beeinflussen kann. Die Studie gibt einen Einblick in die Bremsstrahlung unter extremen Bedingungen, bei denen energiereiche Elektronen durch ein relativistisch transparentes Plasma wandern und dabei von Magnetfeldern mit MT-Stärke abgelenkt werden. Auf der Grundlage der Ergebnisse wird vorgeschlagen, die Implementierung konventioneller Bremsstrahlung in PIC-Codes zu modifizieren, um den diskutierten Unterdrückungseffekt zu berücksichtigen.

Contents

List of Tables

List of Figures

Chapter 1

Motivation and Introduction

Many astrophysical phenomena create high-field environments that drive interest in high-field physics [1–6]. Pulsars are an excellent example. These are neutron stars that are strongly magnetized, rotate, and emit beams of electromagnetic radiation [7]. The magnetic fields of pulsars are indeed extremely strong, with magnitudes on the order of a million to a trillion times stronger than the Earth's magnetic field [8]. This is despite the fact that the force exerted by a magnetic field due to several tens of Tesla can be extreme, leading to the metal coil exploding. Because of that, until recently, this field strength has been inaccessible to laboratory experiments. However, recent developments in high-power laser technology [9–12] have enabled multiple concepts that can be employed to generate slowly evolving (compared to the laser period) magnetic fields with a strength reaching the MT-level [13–17].

One such concept considered in this study relies on the phenomenon of relativistically induced transparency [18–25] to facilitate the volumetric interaction of a high-intensity laser pulse with a dense plasma. In this regime, the high-intensity laser electric field energizes plasma electrons, making them relativistic and altering the plasma's optical properties. As a result, a classically opaque plasma can become transparent, allowing the laser pulse to propagate and drive a longitudinal electron current. Due to the high electron density, this current can be intense enough to generate an azimuthal magnetic field at the MT-level. The combination of the oscillating laser fields and the quasi-static plasma magnetic field creates favorable conditions for enhanced energy gain by plasma electrons. Using particle-in-cell (PIC) simulations, it has been demonstrated that the already available laser intensities are sufficient to generate a large population of electrons with energies in the hundreds of MeV range [26].

The energetic electrons have the potential to emit energetic gamma-rays when deflected by magnetic or electric fields, which opens a path for creating an efficient laser-driven gamma-ray source. It has been shown using PIC simulations that electron deflections by the macroscopic strong plasma magnetic field lead to synchrotron emission of multi-MeV photons [17, 27–29]. The photon population can be so energetic and dense that photon-photon collisions yield an appreciable number of electron-positron pairs [30–32]. The electrons can also be deflected by plasma ions, leading to the bremsstrahlung emission of gamma-rays, where the deflection is caused by the microscopic electric field of an ion. The typical implementation of the bremsstrahlung in PIC codes used for laser-plasma simulations ignores any suppression due to the presence of extreme macroscopic fields. The purpose of this study is to examine whether this is justified and, if not, to provide an assessment of possible suppression.

The concept of bremsstrahlung suppression is well-known in the field of high-energy physics. The photon emission during bremsstrahlung takes place over an extended distance called the formation length l_{f0}. If the electron trajectory is disrupted during the time that it travels the formation length, then the emission becomes suppressed as a result of the disruption. The disruption can arise from relatively frequent collisions with atoms or ions in a dense medium, as in the case of the Landau-Pomeranchuk-Migdal effect. A macroscopic magnetic field can be another source of disruption. The resulting magnetic suppression of bremsstrahlung has been extensively examined in Ref. [33]. It is instructive to investigate high-energy physics scenarios where suppression becomes important. While the Earth's magnetic field (50 μT) significantly suppresses high-energy cosmic rays (10^{20} eV), it does not influence the bremsstrahlung emission from electrons generated by the Large Hadron Collider (LHC) [34]. However, the 4 T magnetic field at the Compact Muon Solenoid experiment at the LHC is sufficient to suppress the emission of 1 TeV electrons.

The general trend for magnetic suppression is that the strength of the magnetic field able to induce the effect goes up as the electron energy goes down. This is one of the reasons why the magnetic suppression effect has been so far ignored for the energetic electrons generated in laser-plasma interactions. Even for 10 GeV electrons, which is currently the upper limit of what can be achieved experimentally, the magnetic field strength must be in the range of 10^3 T for the suppression to be noticeable. Such a field is inaccessible to conventional magnets. However, the plasma magnetic fields in the regime of relativistically induced transparency can be much stronger than 10^3 T, as mentioned earlier, which suggests that the effect of magnetic suppression can come into play.

The objective of this investigation is to examine quantitatively the suppression of bremsstrahlung in intense laser-plasma interactions involving MT-level magnetic fields. As such interactions necessitate the presence of both electric and magnetic fields, we have subsequently extended the analysis employed for the magnetic suppression effect to contain a robust electric field. To self-consistently evaluate the suppression, we have upgraded the standard bremsstrahlung module of the EPOCH PIC code [35, 36] to include the suppression effect by a combination of electric and magnetic fields. Two-dimensional PIC simulations performed with this module have revealed that the bremsstrahlung emission inside the laser-irradiated plasma can become noticeably suppressed, with the total emitted energy decreasing by as much as 30% for some electrons. The reduction primarily impacts the sub-MeV part of the emitted photon spectrum. Even though the synchrotron emission dominates over the bremsstrahlung in the considered regime, our results provide new insights into the bremsstrahlung emission in high-intensity laser-plasma interactions. Specifically, our results indicate that the conventional implementation of bremsstrahlung used by PIC codes needs to be adjusted to include the discussed suppression effect.

The rest of the thesis is organized as follows:

- **Chapter 2:** This chapter describes the basic theory of high-intensity laser-plasma interactions and their role in producing high-energy particles and strong magnetic fields. Topics include plasma properties, high-power lasers, relativistically induced transparency, direct laser acceleration, generation of high-energy radiation, and laser-driven magnetic field mechanisms.

- **Chapter 3:** This chapter provides an overview of the EPOCH PIC code, particularly its implementation of the bremsstrahlung routine. It provides an introduction to the PIC methodology and its application to plasma dynamics, paving the way for discussions on the implementation of the magnetic suppression effect in subsequent chapters.

- **Chapter 4:** Here, the various suppression mechanisms of bremsstrahlung emission and their effects are discussed. This includes the Landau-Pomeranchuk-Migdal effect, dielectric suppression effects, magnetic suppression effect, and pair-creation suppression. This chapter serves as a primer for the subsequent exploration of magnetic suppression.

- **Chapter 5:** This chapter presents a mathematical model for the bremsstrahlung process in the presence of macroscopic magnetic and electric fields. It explores the concept of formation lengths, introduces an extended suppression mechanism, and compares derived suppression factors with those in the literature.

- **Chapter 6:** This chapter outlines the technical integration of the magnetic suppression (MS) and electric-magnetic suppression (EMS) models into the EPOCH PIC code. It explores modifications made to the bremsstrahlung module, the construction of a new table associating suppression factors, and connections to the PIC loop, among others.

- **Chapter 7:** This chapter presents a detailed evaluation of the simulation results obtained using the modified bremsstrahlung modules of EPOCH. It assesses the macroscopic and microscopic effects of bremsstrahlung suppression on high-energy electrons in high-intensity laser-plasma interactions.

- **Chapter 8:** This final chapter summarizes the research findings, discusses their implications for the field of high-intensity laser-plasma interactions, and suggests future directions for research.

Chapter 2

Laser-Plasma Interactions

Laser-plasma interactions have emerged as a promising and versatile area of research with the potential to revolutionize the generation of high-energy particles and high fields. High-intensity lasers, operating at intensities of 10^{18} W/cm^2 and higher, can generate unprecedented phenomena when interacting with plasmas. This chapter provides a high-level overview of the basics governing high-intensity laser-plasma interactions, emphasizing their role in producing high-energy particles and generating strong magnetic fields.

We begin by defining plasma and investigating its properties, providing the reader with a basic understanding of this unique state of matter. The focus then shifts to high-power lasers and their integral role in facilitating laser-plasma interactions. The chapter then explores various methods by which lasers and plasmas interact, including the phenomenon referred to as relativistically induced transparency (RIT). This establishes the foundation for understanding the subsequent sections on laser-driven production: energetic electrons, photons, and magnetic fields. In the section on laser-driven particle acceleration, the direct laser acceleration (DLA) mechanism is examined to show how lasers can manipulate and accelerate particles within a plasma.

Then, we focus on the generation of high-energy radiation through laser-driven processes such as synchrotron radiation and bremsstrahlung emission. This part highlights the potential of laser-plasma interactions to serve as a versatile platform for creating high-energy radiation sources. Finally, we discuss the laser-driven magnetic field mechanisms, emphasizing the generation of strong magnetic fields (MT-level) in the RIT regime and in the structured targets. This magnetic field strength range would be required for our inquiry into the magnetic suppression of bremsstrahlung emission through the next chapters.

2.1 Laser-Plasma Interactions

Advancements in high-power lasers and plasma physics have facilitated the exploration of complex phenomena, leading to discoveries in laser-plasma accelerators [37–47], high-energy laser-driven radiation sources [27, 48–57], and laser-driven magnetic fields [27, 58–63]. These investigations involve understanding the complex interplay between electromagnetic waves, predominantly in the form of laser pulses, and the fundamental constituents of plasma: ions and electrons. As the intensity of the incident laser increases, relativistic effects become increasingly important in the dynamics of the laser-plasma interactions. Therefore, non-linear phenomena such as relativistic self-focusing, relativistic transparency, the generation of intense, high-frequency harmonics, and quantum electrodynamics (QED) effects come into play.

Furthermore, high-intensity laser-plasma interactions play a crucial role in laboratory astrophysics, providing a unique platform for simulating and investigating astrophysical phenomena under controlled situations by recreating the extreme conditions found in various astrophysical environments [64–74]. Laboratory astrophysics has emerged as a powerful tool for bridging the gap between theoretical predictions and observational data from space telescopes, ground-based observatories, and satellite missions [74].

One key area of research in laboratory astrophysics is the study of super strong astrophysical magnetic fields, which play a crucial role in the evolution of galaxies, stars, and other celestial objects [61, 75–88]. In laboratory astrophysics, the interaction of high-intensity lasers with plasmas has the potential to generate strong magnetic fields, mimicking the conditions found in astrophysical environments [88]. This regime of interaction allows researchers to investigate the fundamental processes governing the generation, amplification, and even dissipation of magnetic fields, providing valuable insights and constraints on theoretical models and astrophysical observations.

This section provides a concise summary of the basic parameters of lasers and plasma that play an important role in laser-plasma interaction, thereby laying the groundwork for subsequent sections on laser-driven particles and laser-driven magnetic fields.

2.1.1 Definition and Properties of Plasma

Plasma, a unique state of matter, is defined as a mixture of ions, electrons, and neutral particles generated by the ionization process, which involves the extraction of one or more electrons from an atom or molecule [89]. The degree of ionization in a medium determines whether it can be classified as plasma. Under extreme thermal conditions, plasmas usually achieve full ionization, wherein all outer electrons are removed from their respective parent atoms or molecules. This process results in a gas composed entirely of free electrons and bare atomic nuclei, referred to as fully ionized plasma [90].

Plasmas are also described as gases in which charged particles exhibit *collective behavior*. This refers to the coordinated movement of these particles in response to an external field, emerging from long-range Coulombic interactions among the charged particles [91]. An example of collective behavior is plasma oscillations, or plasma waves, where all charged particles oscillate in phase, resulting in a propagating electromagnetic wave. The natural frequency of these oscillations, so-called *plasma frequency*, is dependent on the electron density of the plasma and is crucial for understanding plasma dynamics and wave-particle interactions. This frequency, ω_{pe} is expressed by [89]:

$$\omega_{pe} = \sqrt{\frac{n_e e^2}{\epsilon_0 m_e}}, \tag{2.1}$$

where n_e denotes the electron density, ϵ_0 the permittivity of vacuum, e the elementary charge, and m_e the electron mass. For a typical plasma with an electron density of $n_e = 1 \times 10^{25}$ m^{-3}, common in many laser-plasma experiments, the plasma frequency is $\omega_{pe} = 1.78 \times 10^{14}$ rad/s.

Regarding the interaction of the electromagnetic wave with plasma, when the frequency of the wave, such as a laser's frequency, ω_L, is lower than ω_{pe}, electrons can shield the laser's field, inhibiting its propagation through the plasma. Equating the plasma frequency formula to the laser frequency, $\omega_{pe} = \omega_L$, we can derive the plasma density at which the propagation ceases. This plasma density, known as the *classical critical density* or *cutoff density* denoted by n_{cr}, and is given by:

$$n_{cr} = \frac{m_e \varepsilon_0 \omega_L^2}{e^2}, \tag{2.2}$$

Conversely, when the laser's electric field is exceptionally strong, plasma electrons oscillate at high velocities, nearing the speed of light c. As a result, the effective electron mass increases due to relativistic effects, given by γm_e, where $\gamma = 1/\sqrt{1 - v_e^2/c^2}$ is the Lorentz factor and v_e is the electron velocity. Consequently, the increase in effective electron mass alters the electron plasma frequency, $\omega_{pe}/\sqrt{\gamma}$, causing the electrons to become less responsive to the changing field, in turn effectively altering the critical density value, γn_{cr}. This relativistic correction of the classical critical density allows the laser propagation through the denser plasma [92].

Plasmas can be classified into underdense and overdense categories based on their density in relation to the critical density [93, 94]. At the critical density, the plasma becomes opaque to the incident laser light, transitioning from an underdense plasma ($n_e \ll n_{cr}$) where the laser can propagate to an overdense plasma ($n_e \geq n_{cr}$) where the laser is strongly reflected [95]. For a typical high-intensity laser with a wavelength of $\lambda_L = 800$ nm and $\omega_L = 2.36 \times 10^{15}$ rad/s, the critical density is $n_{cr} = 1.74 \times 10^{27}$ m^{-3}.

Quasineutrality is another essential property of plasmas, arising due to the significant charge separation between positively charged ions and negatively charged electrons [90]. On a sufficiently large spatial scale, the net charge of a plasma is essentially zero, as positive and negative charges tend to balance each other. Mathematically, this can be expressed as:

$$\sum_i q_i n_i = 0, \tag{2.3}$$

where q_i and n_i are the charge and density of the i-th species of particles, respectively. In fully ionized plasmas, the quasineutrality condition can be simplified to $n_e = \sum_i Z_i n_i$, where Z_i is the ion charge in units of the electron charge.

When an externally charged particle is introduced into a plasma, it generates an electric field that attracts oppositely charged particles and repels like-charged particles. This rearrangement of charges forms a cloud around the original charged particle, neutralizing its electric field at a distance from it. This is characterized by the Debye length—a characteristic length scale in plasma that describes the screening length due to the charged particles—given by [96, 97]:

$$\lambda_D = \sqrt{\frac{\epsilon_0 k_B T_e}{n_e e^2}}, \tag{2.4}$$

where T_e is the electron temperature and k_B is the Boltzmann constant. For a typical low-temperature laboratory plasma with an electron density of $n_e = 10^{18}$ m^{-3}, electron temperature $T_e = 1$ eV, and ion charge $Z_i = 1$, the Debye length is approximately 7.43 μm.

Understanding these fundamental properties of plasmas is key to exploring the complex mechanisms governing laser-plasma interactions and their varied applications. While we have highlighted some important characteristics in plasma physics, there are numerous textbooks [89, 92, 96, 97] available in this field for interested readers seeking more detailed information and derivations. In the next section, we provide a brief overview of high-power laser properties involved in laser-plasma interaction experiments.

2.1.2 High-Power Lasers

High-power lasers have attracted considerable attention from the scientific and industrial communities over recent decades. This interest primarily stems from advancements in laser amplification techniques, particularly chirped-pulse amplification (CPA) [98], and their capacity to generate extreme conditions in matter [99]. These potent laser systems can produce peak powers ranging from terawatts (TW) to petawatts (PW), leading to a multitude of applications in fundamental research, such as laser-driven particle acceleration [46, 47], laboratory astrophysics [73, 74], and ultra-fast x-ray science [9, 100–103]. Furthermore, they have practical applications in material processing [104], nuclear fusion [9, 105–108], and medical imaging [109–111]. High-power lasers additionally facilitate a novel regime in the physics of relativistically transparent laser-plasma interaction, which will be explained in more detail in Subsection (2.1.4). Figure (2.1) illustrates the significant role that CPA technology has played in the rapid development of laser technology, leading to the emergence of PW laser facilities and even more sophisticated systems. This escalation in laser power has been accompanied by a substantial increase in laser intensity, potentially expanding the field of laser physics to include energy scales from electronvolt (eV) to megaelectronvolt (MeV), even to the extraordinary teraelectronvolt (TeV) domain.

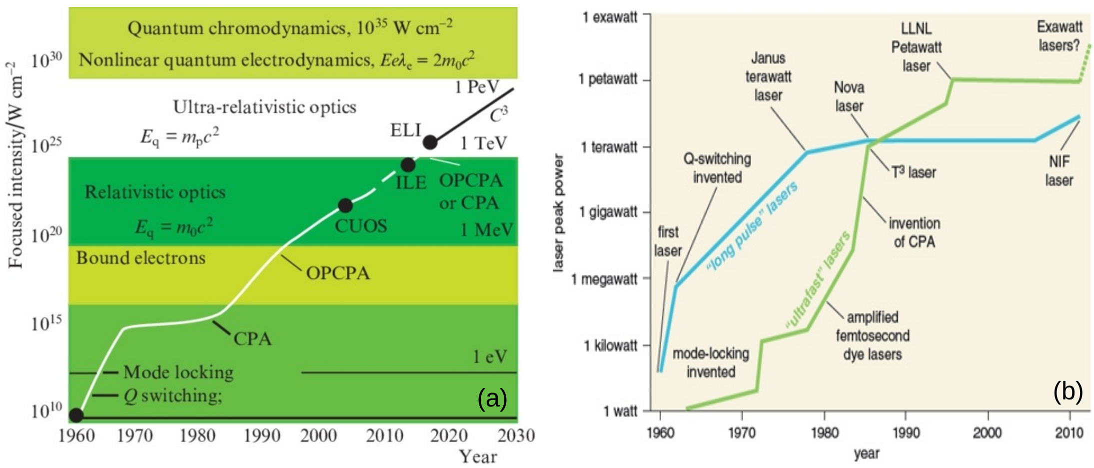

Figure 2.1: Evolution of laser-focused intensity and peak power over time, illustrating the impact of CPA technology on the rise of petawatt (PW) lasers and the expansion of laser physics across various energy scales. Adapted from articles (a) [112] and (b) [113].

Key parameters of high-power lasers include pulse duration τ_L, pulse energy E_L, peak power P_{peak}, and focused intensity I_L. These collectively determine the interaction regimes between lasers and matter and the underlying physical phenomena. Pulse duration, representing the temporal width of the laser pulse, ranges from picoseconds (ps) to femtoseconds (fs) and is typically used to achieve high peak powers [100, 114–116]. Pulse energy describes the total energy within a single laser pulse and is usually measured in joules [J]. The peak power of a laser pulse, given by $P_{peak} = E_L/\tau_L$, represents the maximum power reached during the pulse. The focused intensity, another critical laser parameter, denotes the amount of laser power concentrated within a specific area (A) and is typically expressed in [W/cm^2], calculated using $I_L = P_{peak}/A$.

The refinement and development of high-power laser systems remain an active research area, with ongoing efforts aimed at enhancing the key metrics mentioned above. State-of-the-art facilities, like the Extreme Light Infrastructure (ELI)[†], situated in Europe, are advancing the frontier of laser technology. They offer the scientific community unprecedented access to ultra-high-intensity laser pulses, paving the way for the exploration of novel physical regimes. Among its multiple groundbreaking features, the ELI, for instance, will feature high power, multi-beam capabilities anticipated to deliver an extraordinarily high intensity of 10^{22} W/cm^2 and above. In this dissertation, our objective is to employ a laser with characteristics comparable to those of current and forthcoming PW laser facilities. We will specifically focus on projected intensities around 5×10^{22} W/cm^2, similar to advanced facilities like ELI-NP [117] and the Texas Petawatt Laser [118, 119].

2.1.3 Laser-Plasma Interaction Mechanisms

One of the defining characteristics of lasers is their capacity to generate high electric fields, which can ionize matter and, in the case of high-intensity lasers, produce high-energy-density plasmas [120]. As the intensity of the laser increases, the behavior of the plasma undergoes a significant transformation, transitioning from linear to nonlinear and ultimately to relativistic interactions.

- **Linear Regime:** In the linear regime, typically at intensities below 10^{13} W/cm^2, the interaction of the laser with the plasma can be represented by linear processes. In this context, the electric field of the laser is relatively weak, and the plasma's response can be depicted as linear perturbations from its equilibrium state. Phenomena such as linear plasma waves and linear absorption of laser energy characterize this regime [121].

[†]https://eli-laser.eu/

- **Nonlinear Regime:** When the laser intensity amplifies, typically ranging from 10^{13} to 10^{18} W/cm^2, the electric field of the laser becomes comparable to the electric field within the plasma. The laser-plasma interaction shifts into the nonlinear regime, where the plasma's response to the laser field cannot be represented by a simple linear perturbation. Instead, phenomena such as plasma wave breaking, self-focusing, and harmonic generation become dominant [122].

- **Relativistic Regime:** When the laser intensity exceeds about 10^{18} W/cm^2, the quivering movement of an electron in the light field turns relativistic and approaches the speed of light. This laser intensity is referred to as the threshold of the plasma's relativistic regime [120]:

$$I_{rel} \approx 1.37 \times 10^{18}[\mathrm{W/cm}^2]/\lambda_L^2[\mu m], \tag{2.5}$$

  which leads to a variety of phenomena such as relativistic self-focusing [123], relativistic harmonic generation [124], generation of relativistic plasma waves suitable for particle acceleration, and the production of intense bursts of gamma-ray radiation [54].

During laser-plasma interactions, the laser system generates a weaker pre-pulse due to technological limitations, which interacts with the target material and ablates a thin layer, forming a low-density plasma [125, 126]. This is then impacted by the subsequent main pulse, which is much more intense and exerts significant radiation pressure, boring a hole into the plasma slab and creating a cavity [127]. The deformation of the target front improves the absorption of the laser pulse in these regions, resulting in more efficient transmission of energy from the pulse to the plasma. This is a crucial component for processes such as electron acceleration and high-energy radiation generation [128, 129].

However, at very high intensities, such as 5×10^{22} W/cm^2 (which we have employed in this study), the dynamics of laser-plasma interactions can indeed be different. This intensity range is associated with what is often referred to as ultra-relativistic laser-plasma interactions. In this regime, the laser field can become sufficiently intense to readily ionize matter, converting it into plasma. This process almost instantaneously accelerates the free electrons within the plasma to relativistic speeds.

2.1.4 Relativistic Induced Transparency (RIT)

In the nonrelativistic regime of plasma electrons, as explained in subsection (2.1.1), there is an upper limit for the electron density $(n_e \ll n_{cr})$ that can be transparent to a laser. In this regime, the critical density depends only on the laser's frequency, given by $n_{cr} = m_e \varepsilon_0 \omega_L^2 / e^2$. A laser with a frequency lower than the plasma frequency is unable to penetrate the plasma since the refractive index of the plasma, $n = \sqrt{1 - n_e/n_{cr}}$, becomes imaginary. This constraint, however, undergoes a dramatic shift in the ultra-high intensity regime, where the target's electrons become relativistic due to an increase in effective mass. In such a situation, the critical density also increases, approximated by an average relativistic factor of $\gamma_{ave} \sim a_0$, with a_0 representing a normalized laser amplitude [130]:

$$a_0 = \frac{|e|E_0}{m_e \omega_L c} = 0.855\lambda_L[\mu m]\sqrt{I_L[\mathrm{W/cm^2}]/(1 \times 10^{18})}, \tag{2.6}$$

Here, E_0 denotes the electric field amplitude, ω_L is the frequency of the laser pulse, I_L signifies the peak laser intensity, and λ_L defines the laser wavelength. This normalized parameter fundamentally measures how relativistic electrons become in a laser pulse of a given amplitude. Under these conditions, the refractive index of the plasma also adjusts, leading to a revised refractive index expression that incorporates relativistic effects [24]:

$$n_{rel} = \sqrt{1 - \frac{n_e}{\gamma_{ave} n_{cr}}} \tag{2.7}$$

As a consequence, the laser can penetrate deeper into the plasma, a phenomenon known as relativistically induced transparency (RIT). For instance, a laser pulse with an intensity of $I_L = 5 \times 10^{22}$ W/cm^2 and $\lambda_L = 0.8$ μm, it can be estimated that $a_0 \approx 150$. Note that this relativistic modification significantly broadens the transparency range, expanding the density domain from $0 < n_e < n_{cr}$ to $0 < n_e < a_0 n_{cr}$, thereby rendering the classically overdense plasma highly transparent to the laser pulse[17].

This scenario is depicted in Figure (2.2) for typical parameters in overdense plasmas as a function of laser frequency (ω_L). The blue line represents the electron density (n_e), which varies between $0.1n_{cr}$ and $1.5n_{cr}$, shown by the red line. The black line represents the relativistic critical density (γn_{cr}), which takes into account the relativistic effects induced by the intense laser pulse. The gray-shaded region indicates the range of transparency due to relativistic effects when $n_e < \gamma n_{cr}$. The yellow-shaded region represents the range of transparency in the absence of relativis-

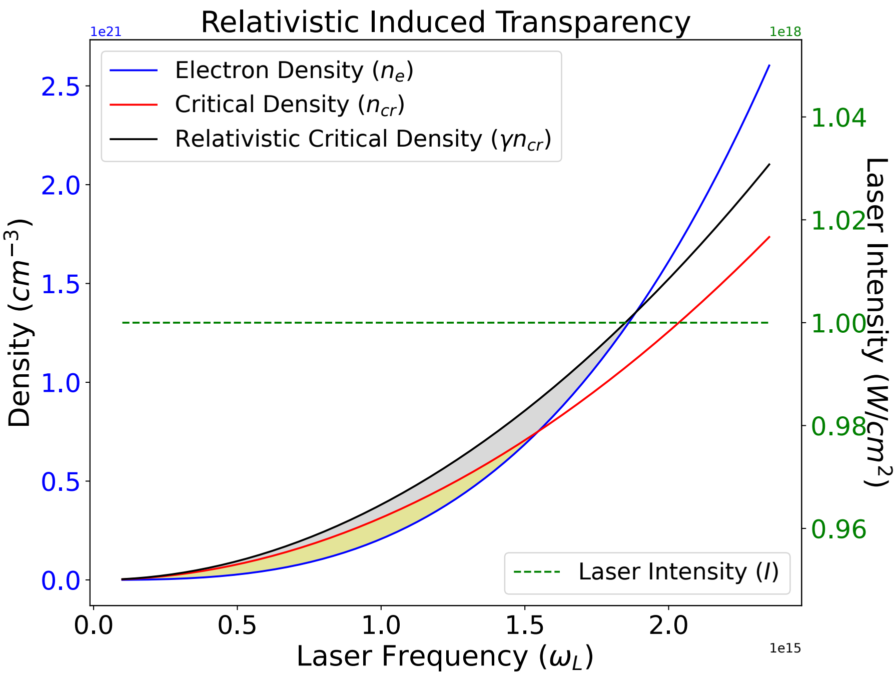

Figure 2.2: Relativistic Induced Transparency. Plotted are electron density (n_e, blue), classical (n_{cr}, red), and relativistic critical densities (γn_{cr}, black) as functions of laser frequency (ω_L). Yellow and gray-shaded regions represent non-relativistic and relativistic transparency ranges, respectively. The green dashed line shows the laser intensity (I_L).

tic effects, $n_e < n_{cr}$. A secondary y-axis on the right side of the plot displays the laser intensity ranges, highlighting ($I_L \sim 1 \times 10^{18}$ W/cm^2) by the green dashed line. This plot effectively illustrates the interplay between the classical and relativistic critical densities as well as the electron density, highlighting the conditions under which the RIT process occurs.

2.2 Laser-Driven Electron Acceleration

In recent years, significant progress has been made in the field of laser-driven electron acceleration, driven by advances in short-pulse and high-power laser technology and the growing demand for compact, cost-effective particle accelerators. Traditional accelerator technologies, such as radiofrequency (RF) cavities and linear accelerators, utilize oscillating electric fields to transfer energy to charged particles. However, the maximum electric fields these technologies can generate are limited, resulting in facilities that become progressively larger and costlier as the required particle energies increase. In contrast, laser-driven accelerators leverage the intense electric fields generated during laser-plasma interactions to accelerate particles over much shorter distances, offering potential reductions in size and cost. The development has led to the investigation of two primary mechanisms: laser wakefield acceleration (LWFA) and direct laser acceleration (DLA).

In LWFA, an intense, ultra-short laser pulse (typically with $\tau_L \sim$ fs) interacts with an underdense plasma, causing electron displacement, which leads to the formation of a plasma wave. This process also results in the generation of an intense plasma electric field due to the separation between electrons and ions, commonly referred to as a "Wakefield" [120, 131]. This wakefield can accelerate some electrons to relativistic energies with a monoenergetic spectrum over short distances. Factors such as laser intensity, pulse duration, and plasma density critically influence the LWFA mechanism's efficiency [132–141].

While the LWFA technique has made significant contributions to the field of particle acceleration, this section will specifically focus on the DLA mechanism, which offers a complex yet intriguing mechanism for accelerating charged particles, especially electrons, by the fields of an intense laser pulse. Moreover, the research conducted in this thesis was specifically carried out within this interaction regime, where the DLA mechanism serves as the primary method of electron acceleration.

2.2.1 Direct Laser Acceleration (DLA)

Direct Laser Acceleration (DLA) is a complex process where the energy from a laser's electric field is directly transferred to electrons, causing them to accelerate [142, 143]. Unlike the LWFA technique, DLA typically generates a broader energy spectrum of electrons but can yield a higher total 'charge' – signifying a larger total number of accelerated electrons ($\sim 100s$ of nC) [144].

According to Equation (2.6), if the laser intensity $I_L \geq 1 \times 10^{18}$ W/cm^2, the work conducted by the laser field during a single period is comparable to the electron's rest mass and can lead to the electron's acceleration [26]. In such a situation, when a relativistic laser pulse irradiates a uniform plasma target for longer than the characteristic electron response time ($1/\omega_{pe}$), a quasi-steady-state structure (ion channel) is established in the plasma [145]. This channel possesses quasi-static fields that respond to the laser pulse [146]. In 2D, the transverse force exerted by these electric and magnetic fields on an electron moving forward in an ion channel with velocity, v_x, is always directed toward the axis [26]:

$$F_y = -|e| \left(\bar{E}_y - \frac{v_x}{c} \bar{B}_z \right) \approx -m_e \omega_L c \left(\frac{\Delta n_i}{n_{cr}} + \frac{v_x}{c} \frac{|j_x|}{|e| n_{cr} c} \right) \frac{y \omega_L}{c} \leq 0, \tag{2.8}$$

where $j_x < 0$ is the electron current density, n_i the ion density, and y is a distance from the axis ($y = 0$). In this instance, the charge separation within the ion channel (i.e., the transverse electric field produced by the ions) prevents accelerated electrons from being expelled by a transverse gradient of the ponderomotive pressure exerted by the laser pulse, thereby confining them within the channel [26].

During this process, as the electron velocity approaches the speed of light within one laser cycle, it acquires a substantial amount of energy. This energy is then converted into longitudinal momentum $p_{\|}$ (in the direction of laser propagation) via the $\mathbf{v}_{\perp} \times \mathbf{B}_{laser}$ force. This energy gain can be considerably greater than the laser's ponderomotive potential, which is denoted by $\sim \frac{1}{2} m_e c^2 a_0$ [144].

Note that electrons with small initial pitch angles (the angle between their velocity and the magnetic field lines) are subject to the combined influence of radial electric and azimuthal magnetic fields, causing them to oscillate (betatron oscillation) within the fields [147, 148]. A resonant condition is reached when the electron oscillation frequency matches the Doppler-shifted oscillation frequency of the laser light and the phases of the electron and laser fields align. Arefiev et al. [146] demonstrated that the longitudinal field decreases the dephasing rate without significantly transferring energy during the interaction. The electron gains substantial energy after the interaction with the longitudinal field, where the extra energy is transferred from the laser pulse rather than from the longitudinal field directly. Moreover, Gong et al. [26] using a specific structured target (i.e., hollow-core target) reported a new method for achieving collimated laser-accelerated energetic electrons in which the quasi-static electric and magnetic fields induce a transverse force that is given by [26],

$$F_y = -|e| \left(\bar{E}_y - \frac{v_x}{c} \bar{B}_z \right) \approx -m_e \omega_L c \frac{n_e}{n_{cr}} \left(1 - \frac{v_x u}{c^2} \right) \frac{y \omega_L}{c} \geq 0, \tag{2.9}$$

where u is the effective electron's velocity inside the channel. Notably, these fields compensate each other for ultra-relativistic electrons ($u \to c$) moving in a forward direction.

DLA primarily occurs in underdense plasmas in which the plasma density is below the critical density for a given laser frequency. However, in the RIT regime, DLA can also occur in optically opaque plasmas. Recent numerical simulations of laser-plasma interactions revealed DLA assisted by extreme self-generated magnetic fields in the RIT regime [27, 149]. Figure (2.3) illustrates such an interaction schematically in a plasma channel, depicting the acceleration of a single electron through the plasma channel in the forward direction and the magnetic fields that contribute to acceleration.

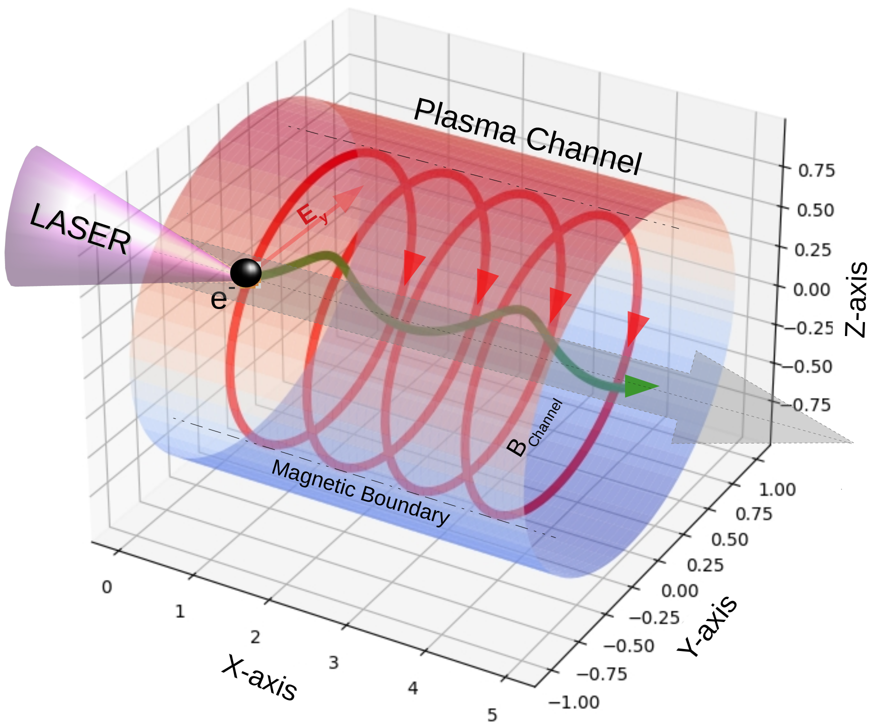

Figure 2.3: This 3D plot provides a schematic representation of the direct laser acceleration mechanism in a plasma channel. The cylinder represents the plasma channel created when the laser hits and energizes the electrons. The green wavy curve illustrates the trajectory of an accelerated electron within the channel. The red rings depict the azimuthal magnetic fields generated due to electron currents inside the plasma channel, contributing to the acceleration of the electrons.

2.3 Laser-Driven High-Energy Radiation

Laser-driven particle acceleration techniques have the potential to generate high-energy radiation with energies ranging from MeV to GeV, enabling the investigation of phenomena that cannot be studied using conventional sources [27, 52, 92, 150–152]. Two primary schemes, including synchrotron radiation and bremsstrahlung emission, are capable of producing this kind of radiation. Understanding how laser-plasma interactions generate high-energy radiation is crucial for improving these sources and developing novel applications. Following is a concise summary of these schemes, including references for further study.

2.3.1 Synchrotron Radiation

Synchrotron radiation is a type of electromagnetic radiation in the form of X-rays and gamma-rays produced when energetic electrons travel through the magnetic filament and experience transverse deflection [153]. This radiation is forward-directed in the direction of electron motion with the emission angle $\sim 1/\gamma$, where γ is the relativistic factor. In the context of the laser-plasma interactions, this kind of electron's trajectory can be due to the magnetic fields present in the plasma [154, 155]. The characteristics of this radiation (like its spectrum, direction, and polarization) depend on the properties of the electron beam (such as its energy and the curvature of its path) and on the magnetic fields in the plasma [153]. The power of radiation, denoted as P_{rad}, is influenced by the acceleration of electrons in an instantaneous rest frame. It follows a scaling relation, where $P_{\mathrm{rad}} \propto \eta^2$ [156], and in a more general context, this normalized parameter for any Lorentz frame can be expressed using the generalized form [27]:

$$\eta = \frac{1}{E_{cr}} \sqrt{\left(\gamma \mathbf{E} + \frac{1}{m_e c} [\mathbf{p}_e \times \mathbf{B}]\right)^2 - \frac{1}{m_e^2 c^2} (\mathbf{p}_e \cdot \mathbf{E})^2} \tag{2.10}$$

In this equation, $\mathbf{E}$ and $\mathbf{B}$ represent the electric and magnetic fields, respectively; $\mathbf{p}_e$ is the electron's momentum; and E_{cr} is the Schwinger limit. The Schwinger limit is a theoretical threshold of the electric field strength, $m_e^2 c^3 / e\hbar \sim 1.32 \times 10^{18}$ V/m, above which electron-positron pairs can be generated from a vacuum. In comparison to the Schwinger limit, the parameter η quantifies the intensity of the electric field felt by the electron in its rest frame, formulated as $\eta \sim \gamma E_{\perp} / E_{cr}$, where $E_{\perp}$ denotes the transverse electric field experienced by the electron. As η increases, the average energy of the emitted photons represents a significant fraction of the electron's kinetic energy [157]. Therefore, laser intensities exceeding 10^{23} W/cm^2 are required to attain a regime that produces copious emissions of multi-MeV photons.

Recently, Stark et al. [27] highlighted the possibility of producing highly efficient, collimated multi-MeV synchrotron radiation through an all-optical single-beam setup, utilizing a self-generated magnetic field in the interaction of the laser (5×10^{22} W/cm^2) with the structured plasma target. They demonstrated that the self-generated magnetic field significantly enhances the acceleration of electrons moving along a plasma channel and that such a magnetic field's force is not counterbalanced by an electric field, unlike in the case of a laser pulse. In this instance, they estimated $\eta^2 \approx 4 \times 10^{-3}$ for the characteristic strength of the self-generated magnetic field of $B \sim 0.2 B_0$; however, this estimation dropped significantly to $\eta^2 \approx 10^{-13}$ when an accelerated electron moving in the same direction as the laser pulse was considered. This decrease takes place as a result of the magnetic field of the laser pulse counteracting the force of the electric field.

Figure 2.4 shows their simulation of the sample emitting electron trajectory in the plasma channel. This demonstrates how a magnetic field, generated by the plasma, constrains the electron to a specific channel. When the electron encounters the intense quasi-static magnetic field at the edges of this channel, it deflects at its turning points. This interaction triggers the emission of synchrotron radiation. These advancements offer new horizons for compact, high-intensity radiation sources, thus making a significant contribution to fields relying on high-energy radiation.

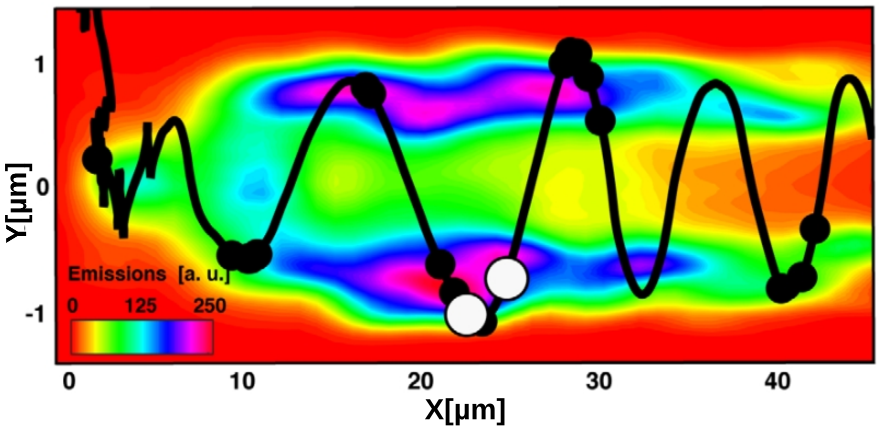

Figure 2.4: An example electron path (depicted in black) demonstrates emissions exceeding 2 MeV (represented by black circles) and those exceeding 30 MeV (illustrated by white circles) as it moves across the channel. The emission count for photons exceeding 30 MeV is indicated by the background color gradient in each cell. Adapted from article [27]

2.3.2 Bremsstrahlung Radiation

Bremsstrahlung mechanism refers to the deflection or deceleration of a charged particle, such as an electron, by another charged particle, such as an atomic nucleus [158], thereby losing energy and emitting radiation. Bremsstrahlung radiation forms a continuous spectrum because the degree of deflection or deceleration of the incident particle can differ, resulting in the radiation of varying frequencies.

In laser-plasma interactions, bremsstrahlung can occur when the laser field accelerates high-energy electrons that are deflected or decelerated by the electric field of the plasma's ions [49, 50, 152, 159–163]. This method allows MeV electrons produced by laser-plasma accelerators to be converted into MeV photons via bremsstrahlung and collision with high Z solid targets [36, 164].

The characteristics of bremsstrahlung radiation, including its intensity, energy, and spectrum, are influenced by several parameters, such as the intensity and frequency of the laser pulse, the density and temperature of the plasma, and the energy of the accelerated electrons. Consequently, this radiation serves as a pivotal diagnostic tool for hot-electron detection, with applications spanning various disciplines such as nuclear fusion research and astrophysics. In the realm of hot plasma physics, bremsstrahlung radiation is a definitive signature of hot electron generation. As hot electrons traverse through colder, denser media, they frequently engage in bremsstrahlung interactions, resulting in the emission of high-energy photons. The detection and subsequent analysis of this emitted radiation allow scientists to ascertain crucial properties of the hot-electron population, including their energy distribution and density [165, 166].

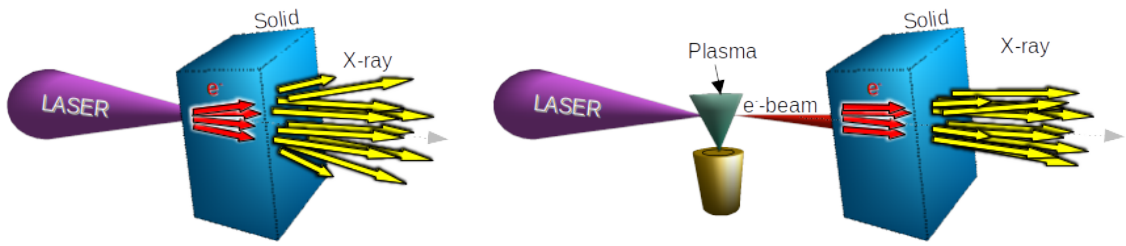

(a) Solid-Target (b) Gas-Jet-Target

Figure 2.5: Bremsstrahlung generation in laser-matter interactions, depicting (a) the solid target and (b) the gas jet-solid target configurations Each configuration employs a unique electron acceleration mechanism, leading to varying efficiencies of bremsstrahlung radiation production.

Figure (2.5) presents two distinct target configurations designed for the generation of bremsstrahlung radiation. The first configuration involves solid targets [see 2.5(a)], where the ponderomotive acceleration process, resulting from the non-uniformity of the laser electric field, generates high-energy electrons. These electrons, moved at a broad range of angles, interact with the atomic structures within the solid target, leading to the emission of bremsstrahlung radiation. The second configuration employs a gas jet-solid target [see 2.5(b)]. In this setup, a short, intense laser pulse activates the LWFA mechanism, producing a highly collimated, high-energy electron beam. This energetic electron bunch hits a solid target, resulting in a more efficient generation of bremsstrahlung radiation.

Note that despite the prevalent use of these setups in bremsstrahlung generation, this thesis will concentrate on the generation of bremsstrahlung in structured targets, as previously mentioned in the context of the DLA mechanism. Further details concerning the bremsstrahlung process will be explored in Chapter (4).

2.4 Laser-Driven Magnetic Fields

Understanding cosmic magnetic fields is essential in astrophysics for explaining the complex mechanisms involved in the formation, evolution, and interaction of celestial objects. In some cases, these magnetic fields can reach immense strengths, influencing the behavior of matter and radiation in their vicinity. At one extreme, magnetars—a rare subset of neutron stars—exhibit extraordinarily powerful magnetic fields of up to 10^{11} T[†], one of the most intense known in the universe [168]. Comparatively less extreme but still significant, a non-magnetar neutron star emits beams of electromagnetic radiation due to their magnetic fields on the order of 10^6 T.

These enormous field strengths also raise intriguing questions about the quantum electrodynamics effects, particularly regarding the Schwinger limit. The Schwinger critical magnetic field, denoted as B_{cr}, which is roughly 4.41×10^9 T, represents a crucial threshold beyond which a vacuum could destabilize, leading to the spontaneous creation of electron-positron pairs, an effect known as the Schwinger effect. This quantum phenomenon, mathematically described by the Schwinger pair production rate formula, is expected in a sustained, uniform field of this strength, but direct experimental confirmation remains elusive due to the tremendous field strengths required.

Surprisingly, high-power laser-plasma interaction experiments can offer a valuable way to explore these magnetic fields in a controlled laboratory environment and simulate key aspects of the behavior and properties seen in the cosmos [27, 69, 75, 88, 169]. Through these interactions, researchers can generate strong magnetic fields on the order of kT to MT, which are several orders of magnitude stronger than those typically achievable using conventional techniques [61].

Two mechanisms in particular, the Biermann battery effect and Weibel instability, have been instrumental in generating magnetic fields in laser-plasma interactions. The Biermann battery effect allows for the creation of magnetic fields in regions with steep electron density and temperature gradients, which are often the product of the interaction of a high-intensity laser pulse with a solid target [84]. Due to these gradients, there is a differential pressure experienced by the electrons and ions in the plasma, which leads to a net current. According to Ampere's law, this current then generates a magnetic field.

On the other hand, the Weibel instability describes resistive magnetic field generation due to the growth of resistive instabilities in plasmas with anisotropic electron pressure [170]. The resulting instability can lead to collective behavior among

[†]1 Tesla = 10^4 Gauss [167]

charged particles, forming current filaments and generating quasi-static magnetic fields [75].

Although the laser-driven mechanisms mentioned above are primarily investigated numerically and experimentally in laser-solid interactions, the highest magnetic field predicted numerically is around less than a few hundred kT [16, 27, 171], and experimentally observed on the order of 1.5 kT, for example, in Ref. [61]. Figure (2.6) illustrates a range of magnetic field strengths, from 58 μT at the Earth's surface to the intense fields observed on neutron stars. The new approach of employing structured targets in high-intensity laser-plasma interactions represents a promising advance in the generation of such strong magnetic fields at the MT-level [17, 26, 27, 88, 172, 173]. This range of magnetic field strength is quite impressive, as it is at least three orders of magnitude higher than the maximum values ever measured in a laboratory. Although we have not yet observed the experimental creation of an MT-level magnetic field, the configuration of high-intensity laser-structured target interactions outlined here offers a potential method for generating extremely strong magnetic fields in laboratories. In the following section, we will explain how this is possible under the RIT regime.

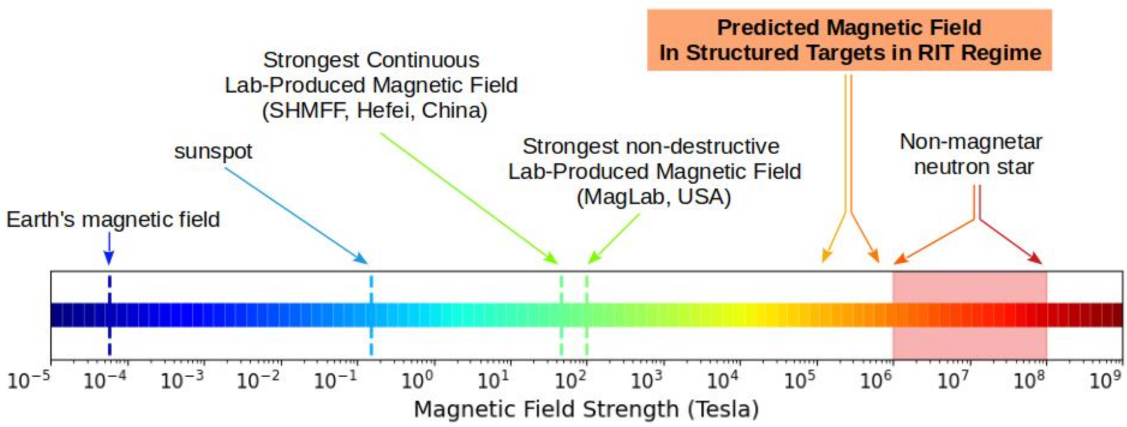

Figure 2.6: Magnetic field strength variations in different environments: A comparison with the RIT regime's high-intensity laser pulse-irradiated structured targets.

2.4.1 Strong Static Magnetic Field via RIT regime

This technique primarily focuses on the regime wherein a high-intensity laser pulse propagates through a relativistically transparent plasma channel in a structured target utilizing the RIT regime. This channel is surrounded by a bulk that is relativistically near critical ($n_e \sim a_0 n_{cr}$). The physical explanation for this technique stems from the interaction regime's ability or inability to generate a sufficiently strong current density necessary for generating a strong magnetic field. Assume that the propagation of a laser pulse through the plasma exerts a force on the electrons, thereby driving this current density.

$$|j| \approx |e|n_e v_e < |e|n_e c, \tag{2.11}$$

where v_e is the directed electron velocity, e is the electron charge, and n_e is the electron density. As stated in subsection (2.1.1), the density of nonrelativistic electrons is limited by the cutoff density, $n_e \ll n_{cr} \equiv m_e \pi c^2/\lambda_L^2 e^2$, which is set solely by the laser's wavelength. As noted in the RIT regime, however, an ultra-intense laser pulse can energize electrons, turning them relativistic and thereby increasing their effective mass by a factor $\gamma \sim a_0$. Due to the relativistic effect, the laser pulse can propagate in a classically dense plasma ($n_e \geq n_{cr}$) because the plasma's optical properties change from classically opaque to relativistically transparent. The upper limit on electron density consequently linearly depends on the laser's amplitude, $n_e \ll a_0 n_{cr}$ [17]. Thus, increasing a_0 (to attain transparency) and plasma density can result in higher current densities, as shown in the following equation [17]:

$$j \approx \frac{n_e}{n_{cr}} \frac{0.05}{(\lambda_L[\mu m])^2} \text{ MA}/\mu m^2, \tag{2.12}$$

where $\lambda_L = 2\pi c/\omega_L$ is the vacuum wavelength of the laser, with ω_L as the laser frequency. Note that in uniform dense plasmas, the laser pulse's propagation can become unstable due to hosing instability†. This instability can be mitigated by employing structured targets that guide the laser pulse along a predictable trajectory [172].

The plasma channel in this structured target remains filled with dense plasma, allowing for effective volumetric interaction between the laser and the dense plasma over the long term. The laser's transverse electric field continually extracts electrons from the channel wall, thereby replenishing the electron population. The laser pulse then forces the electrons forward, generating a longitudinal electron current that is volumetrically distributed. Given the high electron density, this current can be sufficiently strong, exceeding the non-relativistic Alfvén current $J_A = m_e c^3/|e| \approx$ 17 kA [17]. Note that the upper limit of the electron current in the RIT regime is γJ_A [175].

This intense electron current has the potential to produce a magnetic filament with a field strength proportional to the amplitude of the laser ($> 10^5$T) [27, 173],

†Transverse asymmetries in the phase velocity near the pulse's centroid can cause a tilt in the pulse's wavefront and its direction of propagation, a phenomenon known as hosing instability [174].

as presented by [17],

$$B[kT] \approx 3.4\alpha r[\mu m]\lambda_L^{-2}[\mu m], \tag{2.13}$$

where $\alpha = \pi\lambda_L^{-2} j_0/J_A$ and r is the distance from the channel's axis. As illustrated in the two-dimensional snapshot of the simulation of such a mechanism in Figure (2.7), this azimuthally oriented field produces a magnetic filament that can coil around the laser beam. Interestingly, although this field is quasi-static, its strength is comparable to the oscillating field of the laser beam (e.g., estimated $B \approx 0.3B_{laser}$ in Ref. [27], where $B_{laser} \approx 2 \times 10^6$ T is the laser's magnetic field.)

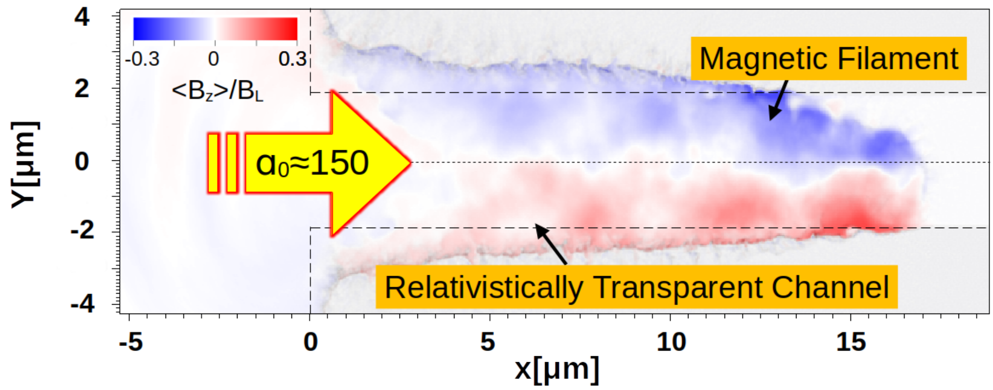

Figure 2.7: Strong static magnetic filament generated in the structured target in the RIT regime.

Notably, structured channels can also play a significant role in the detection of powerful magnetic fields using the Faraday rotation technique. Wang et al. [172] investigated the feasibility of employing an X-ray beam from the European XFEL to detect a strong quasi-static azimuthal magnetic field in a classically over-critical plasma. Faraday rotation is the rotation with the greatest angular momentum and takes place when X-ray propagates parallel to magnetic field lines. Despite the fact that the RIT regime decreases the Faraday rotation, it is possible to increase it by using structured targets that have a relativistically transparent channel surrounded by relativistically near-critical material.

2.5 Summary

In this chapter, we examined several important aspects of laser-plasma interactions and investigated how these interactions serve as a pathway to high-energy radiation sources. We began by defining plasma characteristics and the conditions necessary for their formation. Following that, we provided a brief discussion of high-power lasers and their crucial function in inducing laser-plasma interactions.

The chapter then sheds light on a variety of laser-plasma interaction mechanisms, with a particular emphasis on relativistically induced transparency (RIT). This method permits an intense laser pulse to penetrate an overly dense plasma, resulting in a number of significant effects. The next part of the chapter offered a brief overview of laser-driven particle acceleration. We discussed two primary mechanisms for this process: laser wakefield acceleration (LWFA) and direct laser acceleration (DLA). Each of these mechanisms has its own unique characteristics and conditions, leading to diverse applications and phenomena in the field of plasma physics.

Then, the generation of high-energy radiation through laser-driven processes was discussed. We looked at synchrotron Radiation, which involves electromagnetic radiation from charged particles deflected by a magnetic field. Then, we briefly explained the bremsstrahlung mechanism. In the context of laser-plasma interactions, these mechanisms can convert MeV electrons into MeV photons.

Lastly, we conducted a brief review of several common mechanisms for generating laser-driven magnetic fields. We emphasized that recent advancements in high-power laser technology, combined with key concepts such as relativistically induced transparency, have made it possible to simulate strong magnetic fields similar to those found in outer space within terrestrial astrophysical laboratories.

Chapter 3

Bremsstrahlung in Particle-in-Cell Simulations

Particle-In-Cell (PIC) codes have emerged as a significant computational resource, enabling the simulation of plasma dynamics across a variety of research fields. Among these codes, the EPOCH PIC code [35] has been particularly instrumental due to its wide-ranging applicability in various domains of plasma physics.

In this chapter, we aim to provide an overview of the EPOCH PIC code and its implementation of the bremsstrahlung routine. We begin by explaining the essentials of the PIC methodology and highlighting its role in facilitating the simulation of complex plasma dynamics. Following this, we will investigate the bremsstrahlung routine within the EPOCH code. A key focus of this chapter is to pave the way for understanding the routines for implementation of the magnetic suppression effect within the bremsstrahlung module of the EPOCH code, which will be the subject of discussion in Chapter (6).

3.1 Introduction to Particle-in-Cell (PIC) Simulations

Particle-in-Cell (PIC) simulation is a powerful computational method for exploring plasma dynamics in a variety of research areas such as cosmology [176, 177], plasma thrusters [178, 179], laser-plasma interactions [35, 142, 180–182], and fusion [183, 184]. That was initially introduced in plasma physics in the late 1950s by Buneman [185] and Dawson [186]. The technique involves partitioning the plasma into small "macro-particles," each representing a group of real particles, which are then tracked through their interactions with each other and the electromagnetic fields.

A key strength of the PIC method is its ability to resolve these fields in a self-consistent manner. This feature enables the method to capture plasma's collective behavior, including phenomena such as wave formation and instabilities. This strength is particularly beneficial when studying laser-plasma interactions, where plasma may exhibit substantial non-uniformity and the interactions could be highly nonlinear. Moreover, the PIC method accommodates the simulation of a broad range of plasma parameters. It thus enables the study of both collisional and collisionless plasmas, providing a comprehensive view of plasma dynamics.

However, the PIC method is not without its drawbacks. A major constraint is a computational cost; simulating numerous macro-particles over long time scales can demand significant computational resources. Additionally, the method may be prone to numerical noise and other numerical artifacts, which can potentially affect the accuracy of the simulations. Despite these limitations, the PIC method remains a crucial tool in simulating plasma dynamics, with wide-ranging applications across diverse research fields.

3.1.1 Basic principles of PIC method

Vlasov-Maxwell equations form the basis for the PIC approach for simulating collisionless plasmas. The Vlasov equation, a partial differential equation, characterizes the temporal evolution of the distribution function of an N-particle system, $f^N(\mathbf{r}_N, \mathbf{p}_N, t)^\dagger$. In its simplest form, the evolution of the single-particle distribution function is described as follows [120]:

$$\frac{\partial f}{\partial t} + \frac{\mathbf{p}}{m\gamma}\bigtriangledown f + \frac{\mathbf{F}_L}{m}\frac{df}{d\mathbf{p}} = 0. \tag{3.1}$$

†Phase-space distribution function $f^N(\mathbf{r}_N, \mathbf{p}_N, t)$ represents the probability of locating an N-particle system in a particular configuration in 6N-dimensional phase space at time t [187].

where $\gamma = \sqrt{(1 + (p/mc)^2}$ is the relativistic factor and $\mathbf{F}_L$ is the Lorentz force exerted on the particles due to electromagnetic fields,

$$\mathbf{F}_L = q\left(\mathbf{E} + \frac{\mathbf{p}}{m\gamma} \times \mathbf{B}\right) \tag{3.2}$$

where $\mathbf{E}$ and $\mathbf{B}$ are the electric and magnetic fields, respectively. The direction of the magnetic force is perpendicular to both the magnetic field and the charged particle's momentum, in accordance with the right-hand rule, which is advantageous for research involving azimuthal magnetic fields.

In addition, Maxwell's equations govern the behavior of electromagnetic fields in the presence of charged particles. These equations determine the generation and temporal evolution of electric and magnetic fields:

$$\begin{cases} \bigtriangledown \times \mathbf{B} = \mu_0 \left(\mathbf{J} + \epsilon_0 \frac{\partial \mathbf{E}}{\partial t}\right), & \text{Ampere's Law.} \\ \bigtriangledown \times \mathbf{E} = -\left(\frac{\partial \mathbf{B}}{\partial t}\right), & \text{Faraday's Law.} \\ \bigtriangledown \cdot \mathbf{E} = \frac{\rho}{\epsilon_0}, & \text{Gauss's Law.} \\ \bigtriangledown \cdot \mathbf{B} = 0, & \text{Gauss's Law.} \end{cases} \tag{3.3}$$

These fields are influenced by the particles' charges, ρ, and currents, $\mathbf{J}$, which are determined by the distribution function of each particle species (s) derived from the Vlasov equation.

$$\begin{cases} \rho(\mathbf{r}, t) = \sum_s q_s \int f_s(\mathbf{r}, \mathbf{p}, t) d\mathbf{p}, & \text{Charge density.} \\ \mathbf{J}(\mathbf{r}, t) = \sum_s q_s \int \left(\frac{\mathbf{p}_s}{m\gamma}\right) f_s(\mathbf{r}, \mathbf{p}, t) d\mathbf{p}, & \text{Current density.} \end{cases} \tag{3.4}$$

Solving the Vlasov-Maxwell Equations (3.1-3.4) necessitates a self-consistent approach, wherein the fields and particle motion are iteratively solved until convergence is achieved. Given the enormous number of real particles in plasmas, solving these equations can be challenging. The PIC method is a powerful tool for addressing this difficulty and solving partial differential equations effectively. [142, 188–191]. By substituting real particles with macro-particles, the PIC method substantially reduces computational demand, making simulations more efficient and practical. In fact, given the same charge-to-mass ratio, these macro-particles would behave similarly to real particles under the Lorentz force in such a scenario.

In this methodology, macro-particles are distributed on a grid or mesh [190], interacting only through averaged fields and excluding direct particle-particle interactions via the Coulomb force. The existing electric and magnetic field components serve as boundary conditions on a computational grid [192] with finite-sized cells, typically on the order of a Debye length $\lambda_D = (\epsilon_0 k_B T_e / n_e e^2)^{1/2}$. This length scale, detailed in Subsection (2.1.1), dictates how plasma electrons redistribute themselves to shield electric fields. It is crucial to consider this limitation to avoid numerical self-heating [193]. In the following section, we briefly overview the common numerical algorithms employed in PIC simulations.

3.2 Numerical algorithms for PIC simulations

Numerical algorithms are at the heart of PIC simulations, and understanding their complexity is essential for accurate and efficient simulations. This section presents an overview of the key numerical algorithms used in PIC simulations, with an emphasis on the charge deposition, field solver, and particle pusher algorithms. Figure (3.1) provides a visual guide to these important phases, illustrating the progression of a particle system within a PIC simulation.

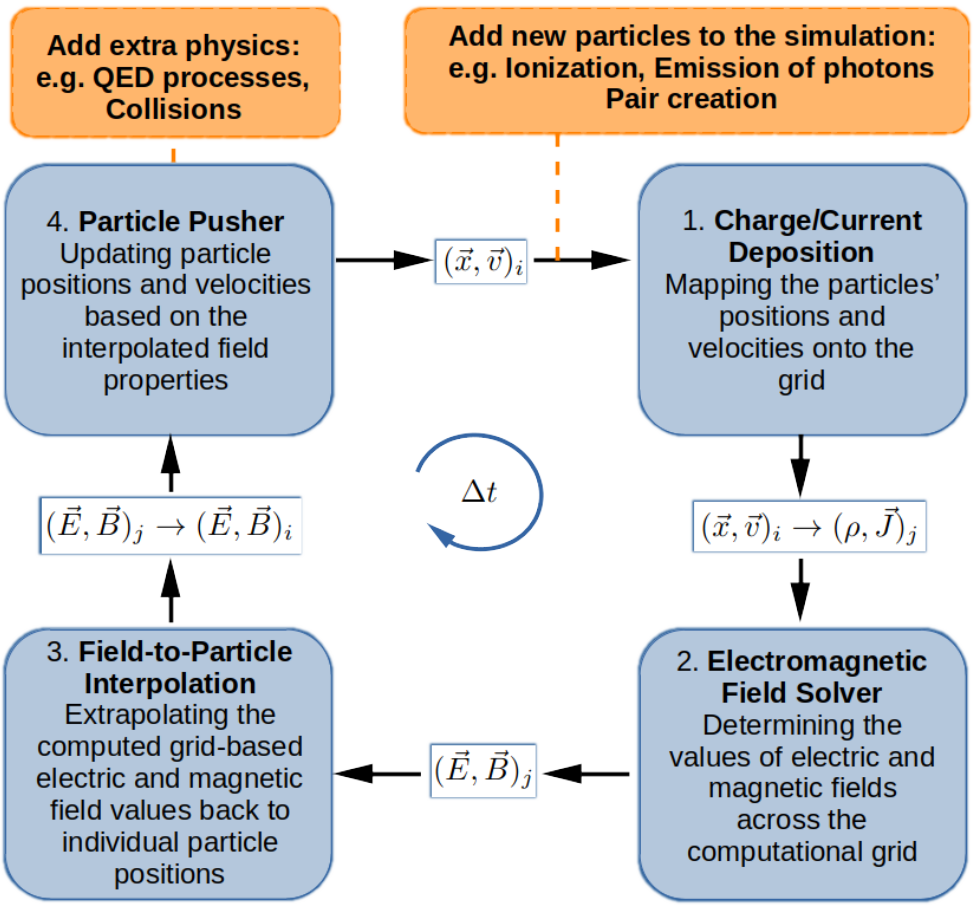

Figure 3.1: Visualizing the PIC Algorithm: A Step-by-Step Progression.

In the following, we will discuss in more detail each stage and the associated algorithms within the PIC simulation process.

3.2.1 Charge Deposition

In the PIC simulations, the initial phase involves the computation of the charge density distribution on a discretized grid, a process commonly referred to as charge deposition [see figure (3.2)]. This critical step involves distributing the charge of each macro-particle over the surrounding grid points, following the equation [120]:

$$\rho(x) = \sum_p q_p S(x - x_p) \tag{3.5}$$

where q_p represents the charge of the macro-particle, x_p represents the particle's position, and S represents the shape function, which is determined by the specific charge deposition scheme in use. This distribution accounts for the spatial extent of macro-particles, thereby ensuring a smoother charge density profile. Moreover, it is crucial to mention that the choice of deposition scheme can significantly impact the numerical stability and accuracy of the simulation.

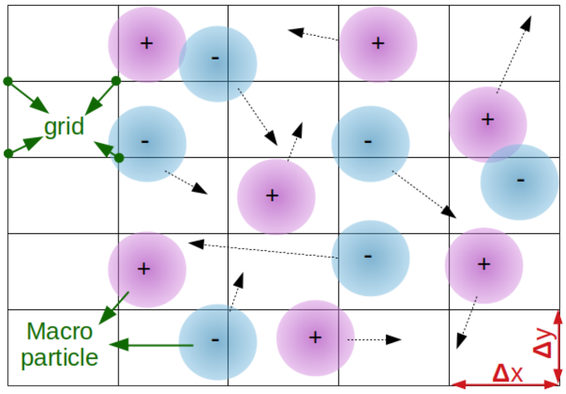

Figure 3.2: Visual representation of charge deposition in a 2D-PIC simulation: Distribution of macro-particle charges over the discretized grids.

Nearest grid point (NGP) and cloud-in-cell (CIC) are the most widely used charge deposition techniques. The NGP method, as the name suggests, assigns the entire charge and mass of a macro-particle to the closest grid point [194], following the equation:

$$S_{NGP}(x - x_p) = \delta(x - x_p) \tag{3.6}$$

where δ represents the Dirac delta function. This method, while straightforward and computationally inexpensive, can generate considerable numerical noise due to its abrupt approximation of the charge density. In contrast, the CIC scheme spreads the charge of a macro-particle between the adjacent grid points, leading to a smoother charge distribution and hence less numerical noise [195]. This is represented by the equation:

$$S_{CIC}(x - x_p) = \max\left(0, 1 - |x - x_p|\right) \tag{3.7}$$

The choice between these methods depends on the specific requirements of the simulation, balancing between computational efficiency and the accuracy of the results.

3.2.2 Field Solver

In the process of PIC simulations, upon establishing the charge density distribution, the subsequent stage involves solving Maxwell's equations. This step is critical as it allows the calculation of the electric and magnetic fields, which significantly influence the motion and interactions of the plasma particles. The numerical techniques employed to solve Maxwell's equations in PIC simulations are referred to as field solvers. These solvers can primarily be categorized into two types: finite-difference time-domain (FDTD) methods and spectral methods.

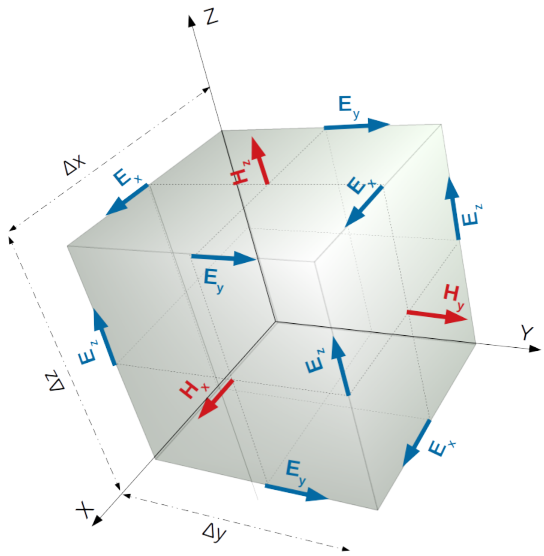

Figure 3.3: Visualization of the Yee grid structure in finite-difference time-domain (FDTD) simulations: Electric fields are assigned to the edges of the grid cells, while magnetic fields are defined on the faces of the cells.

The FDTD method, often implemented using the Yee algorithm, is perhaps the most widely used due to its simplicity and versatility [192, 196]. They involve discretizing the simulation domain into a finite grid and approximating the derivatives in Maxwell's equations with finite differences. This leads to a set of algebraic equations that can be used to explicitly compute the fields at every grid point and time step. The two fundamental Maxwell's curl equations that form the basis of the

FDTD method are:

$$\frac{\partial \mathbf{E}}{\partial t} = c^2 \nabla \times \mathbf{B} - \frac{1}{\epsilon_0}\mathbf{J}, \tag{3.8}$$

$$\frac{\partial \mathbf{B}}{\partial t} = -\nabla \times \mathbf{E}, \tag{3.9}$$

These equations should be normalized and discretized using central-difference approximations. For example, in 1D, they can be rewritten as:

$$\mathbf{E}_i^{n+1} = \mathbf{E}_i^n + \Delta t \left(\frac{\mathbf{B}_{i+\frac{1}{2}}^{n+\frac{1}{2}} - \mathbf{B}_{i+\frac{1}{2}}^{n-\frac{1}{2}}}{\Delta x} - \mathbf{J}_i^{n+\frac{1}{2}} \right), \tag{3.10}$$

$$\mathbf{B}_{i+\frac{1}{2}}^{n+\frac{3}{2}} = \mathbf{B}_{i+\frac{1}{2}}^{n+\frac{1}{2}} + \frac{\Delta t}{\Delta x}\left(\mathbf{E}_{i+1}^{n+1} - \mathbf{E}_i^{n+1}\right), \tag{3.11}$$

where Δt is the time step and $i = 1 \ldots N_{cell}$. Consistent with the layout of the Yee grid (as depicted in Figure 3.3), $\mathbf{E}$ is assigned at the edges of each grid cell, while $\mathbf{B}$ is assigned on the cell faces. This arrangement facilitates the accurate computational representation of electromagnetic interactions. The algorithm then proceeds in a leapfrog manner: the $\mathbf{E}$ field is updated at each half-time step and full spatial step, while the $\mathbf{B}$ field is updated at each full-time step and half-spatial step. This is repeated until the desired simulation duration is reached. Note that despite its widespread application, the FDTD method is subject to numerical dispersion errors, especially when the grid resolution is insufficient.

On the other hand, spectral methods solve Maxwell's equations in the frequency domain or with a basis of functions [197]. These basis functions can be high-order polynomials or other appropriate functions like trigonometric functions, and they are defined globally over the entire domain. Unlike finite difference methods, spectral methods do not discretize the spatial domain into grids. Instead, they express the solution as a series expansion in terms of basis functions that span the whole domain. This is the key feature that differentiates spectral methods from other discretization methods. This method can provide more accuracy and resolution than FDTD, especially for problems with smooth solutions or periodic boundary conditions. Nevertheless, this is typically more computationally demanding and could involve more complex algorithms. The choice between FDTD and spectral methods depends on the specific requirements of the simulation, including its scale, complexity, and the desired balance between accuracy and computational efficiency.

3.2.3 Particle Pusher or Mover

The final step of a PIC simulation is the adjustment of the positions and velocities of the particles in accordance with the calculated electric and magnetic fields. This crucial process is termed the "particle pusher or mover". In many cases, it is the most time-consuming component of PIC simulations. It is essentially the mechanism through which the responses of individual particles to the local electromagnetic fields are accounted for, which in turn affects the subsequent evolution of the fields themselves. This iterative interaction is at the heart of PIC simulations, allowing them to accurately model the self-consistent dynamics of plasma systems.

The particle pusher phase of the simulation employs a variety of numerical algorithms designed to efficiently and accurately integrate the equations of motion for the particles. The Boris algorithm [198] and leapfrog method [190] are two of the most widely used particle pushers in the PIC method. The Boris algorithm, an implicit solver, calculates the particle velocity from the updated field. This method is especially notable for its time-reversal symmetry and bounded energy error[†], characteristics that make it a robust choice for many PIC simulations.

On the other hand, the leapfrog algorithm is an explicit solver that utilizes the force from the previous time step to calculate particle velocity. The selection of the appropriate particle pusher can have significant implications for the accuracy and stability of the simulation, and is hence a key aspect of PIC methodology.

3.2.4 Additional Physical effects in PIC Simulation

In a typical collisionless PIC simulation, the electromagnetic fields and particle motion are calculated without directly simulating particle-particle collisions. This approximation is used when individual binary collisions are either negligible or can be statistically modeled, simplifying the simulation and reducing the computational load. In certain plasma conditions, such as high-frequency or short-wavelength phenomena, this approximation adequately represents the physics. However, in other situations where collisions play a significant role, additional models or algorithms may be required [190]. The Monte-Carlo algorithm is often employed to account for such cases [200, 201]. In this instance, collisions within the cell between randomly

[†]The "bounded energy error" refers to the algorithm's stability in conserving the total energy of the system over time [199]. In many numerical schemes, small errors can accumulate over time and lead to a nonphysical increase or decrease in the total energy of the system, which can lead to nonphysical results. The Boris algorithm, however, maintains a bounded (or limited) energy error over time, which means it does a good job of conserving energy and producing physically realistic results.

paired macro-particles are considered, and the collision rate and deflection angle for each pair are computed [201].

Nevertheless, even in a collisionless simulation, other physical processes, including ionization, radiation, and quantum electrodynamics (QED) effects like pair creation, may need to be modeled [35, 202, 203]. These processes are not traditional "collisions" but involve interactions between particles or between particles and fields, and they can be addressed similarly using a Monte-Carlo method [201, 204]. Depending on the specific problem under study, these modules, as depicted in Fig. (3.1), are typically included as additional processes in the main loop of the PIC simulation.

An additional aspect of physics that can be incorporated into the main loop involves QED processes such as nonlinear Thomson and Compton scattering, pair-creation, and bremsstrahlung emission, which can alter particle dynamics [202, 205, 206]. Consequently, it becomes necessary to adjust the force applied to each particle to align with the momentum generating new particles.

$$\frac{d\mathbf{p}}{dt} = \mathbf{F}_L + \{\text{probabilistic term}\}$$

Then, these newly generated particles (e.g., photons from intense radiation) need to be incorporated into the simulation. We must track these photons, which can interact with other particles or the background fields, thereby creating new particles. If these new particles bear an electric charge, this charge must be deposited onto the grid.

3.3 Analysis Techniques for PIC Simulations

The outcomes of the PIC simulations can be interpreted and examined utilizing a range of techniques, including particle tracking, field visualization, and statistical analysis, all of which have been extensively employed in Chapter (7).

Particle tracking is a technique that monitors the paths of individual particles within the simulation. This technique is invaluable for studying the behavior of particles across different regions of plasma. Field visualization, another key technique, involves the graphical representation of the electric and magnetic fields within the simulation domain. This approach is useful for identifying wave formation and instabilities within the plasma environment.

Statistical analysis, on the other hand, is primarily concerned with the computation of distribution functions for various plasma parameters. These parameters include, but are not limited to, particle density and velocity distribution functions.

This analytical method is vital for studying the transport mechanisms of energy and particles within the plasma.

Beyond these techniques, our analysis has also involved tracing the high fields present within our simulation. We will delve further into this aspect in the succeeding chapters, providing a comprehensive insight into our investigative methods and findings. By employing these techniques, we can gain a comprehensive understanding of the complex dynamics at play within plasma environments as modeled by PIC simulations.

3.4 The EPOCH PIC Code and its Capabilities

The EPOCH (Extendible PIC Open Collaboration) is a robust PIC simulation code designed for plasma physics research. It offers a diverse range of functionalities such as QED physics packages, particle collisions, bremsstrahlung radiation, and ionization routines that enable scientists to model intricate plasma phenomena effectively [35]. Owing to its adaptability, performance, and user-friendly nature, EPOCH has become a preferred tool for investigating high-intensity laser-matter interactions, laser-plasma interactions, and relativistic particle acceleration.

EPOCH employs the FDTD methodology to solve Maxwell's equations on a discrete grid. The Boris algorithm, recognized for its precision and stability, is utilized for particle push operations. Moreover, EPOCH incorporates an array of built-in models and user-provided routines to manage ionization, collisions, and other forms of particle interactions.

The EPOCH code supports various boundary conditions, such as reflective, absorbing, and periodic boundaries. This adaptability enables users to simulate a broad range of physical scenarios, from infinite periodic systems to finite-sized plasmas with different confinement types [35]. EPOCH also offers an extensive selection of diagnostic options for outputting quantities of interest, encompassing electromagnetic fields, derived quantities like energy spectra and currents, and particle distributions. The code allows these outputs to be saved at specific time intervals or upon the occurrence of particular conditions.

The input for EPOCH is provided in a text file named `input.deck`. This file includes all the essential information required to configure the code, such as the domain size, boundary conditions, particle species to simulate, and output settings. The data outputted from EPOCH simulations is written in a new file format known as a self-describing file (SDF). This format allows for analysis and visualization using software such as VisIt or Paraview, both of which offer sophisticated multi-dimensional rendering and analysis capabilities [35].

Designed with high-performance computing in mind, EPOCH can be executed on clusters using MPI for parallelization and is optimized for both GPU and CPU architectures. This design allows researchers to exploit the latest hardware technologies for their simulations, further augmenting EPOCH's utility in the field of plasma physics research.

The PIC loop in the EPOCH is similar to the one depicted in Figure (3.1), beginning with advancing the electric and magnetic fields in the half-time-step [35],

$$\mathbf{E}^{n+\frac{1}{2}} = \mathbf{E}^n + \frac{\Delta t}{2}\left(c^2\nabla\times\mathbf{B}^n - \frac{\mathbf{j}^n}{\epsilon_0}\right),$$
$$\mathbf{B}^{n+\frac{1}{2}} = \mathbf{B}^n - \frac{\Delta t}{2}\left(\nabla\times\mathbf{E}^{n+\frac{1}{2}}\right)$$

Using the Lorentz force, the position and momentum of the particle are updated (i.e., $\mathbf{v}^n \to \mathbf{v}^{n+1}$ and $\mathbf{r}^{n+\frac{1}{2}} \to \mathbf{r}^{n+\frac{3}{2}}$). Then, the second half-step of magnetic field calculation is performed to obtain $\mathbf{B}^{n+1}$, allowing the calculation of the full-step of the electric field.

$$\mathbf{E}^{n+1} = \mathbf{E}^{n+\frac{1}{2}} + \frac{\Delta t}{2}\left(c^2\nabla\times\mathbf{B}^{n+1} - \frac{\mathbf{j}^{n+1}}{\epsilon_0}\right)$$

In this stage, additional physics, such as QED emissions, are accounted for by assigning each particle an optical depth and then checking for emission using the cross-section. The recoil energy of the emitting particle is then considered by reducing $\mathbf{v}^{n+1}$ in order to conserve the system's energy. Following this stage, the code repeats the loop to complete the simulation.

In the following section, we will focus on the examination of the bremsstrahlung module in EPOCH, which serves as a foundation for our implementation in the succeeding chapter.

3.4.1 Bremsstrahlung Routine in EPOCH

EPOCH uses a combination of techniques by Vyskocil et al.[36] and Wu et al. [207] to simulate bremsstrahlung radiation[†]. The technique of Vyskocil et al. relies on Seltzer and Berger's pre-computed data tables [208] containing cross-sections of bremsstrahlung for electrons with energies between 1 keV and 10 GeV. Their procedures are based on the PENELOPE Monte Carlo code [209]. Using the following equation, this approach converts the scaled bremsstrahlung differential cross-section

[†]Note that we have used a version of (epoch4.17.12) in our simulations.

(DCS) to a differential cross-section,

$$\frac{d\sigma}{d\varepsilon_\gamma} = \frac{Z^2}{\beta^2}\frac{1}{\varepsilon_\gamma}\chi(Z, \varepsilon_e, y), \tag{3.12}$$

where $\beta = v_e/c$ is the normalized electron velocity, and $y = \varepsilon_\gamma/\varepsilon_e$ is defined as reduced photon energy. Their routine addresses the collective effects that occur during electron transport, particularly in situations involving high-energy electron sources with extremely high current densities. To accomplish this, they directly incorporated bremsstrahlung emission into the PIC loop, employing a technique comparable to that described in Ref. [210]. These extensive tables enable the simulation to accurately model the behavior of electrons over a broad energy spectrum.

The technique developed by Wu et al. modifies these cross-sections to accommodate plasma screening effects. Plasma screening occurs when the presence of other charged particles in a plasma shield reduces the effective charge of a particle. This can affect the probability of interactions like bremsstrahlung and, therefore, the energy and trajectory of the particles. By implementing this into their simulation, EPOCH is able to more precisely simulate plasma conditions. The combination of these two techniques within the EPOCH code ensures a comprehensive and realistic simulation of bremsstrahlung radiation within a plasma environment. This takes into account a wide range of electron energies and the effect of plasma screening on the interactions between particles.

Before entering the main PIC loop, the subroutine `setup_tables_bremsstrahlung` within the bremsstrahlung module collects the required information. According to the atomic number Z already specified by the user for the target material in the simulation input data, the information is collected from the aforementioned tables. This information consists of electron energies ε_e incident on the neutral atom with the atomic number Z, photon energies ε_γ, cross-sections, and cumulative distribution functions (CDFs).

The Monte Carlo method is utilized within the time loop of the PIC simulation to simulate the stochastic nature of quantum emission [211]. This technique involves assigning each electron a uniformly random emission probability, $\mathscr{P}(\tau_{em}) = 1 - e^{-\tau_{em}}$, ranging from 0 to 1, prior to emission. This probability is then inverted to derive τ_{em}, the optical depth at which the electron emits a photon. This depth is initially calculated by,

$$\tau_{em} = -\log(1 - \mathscr{P}(\tau_{em})) \tag{3.13}$$

The algorithm inside the PIC loop first calculates the ion density n_i of the target at the electron's position in a given cell. Then, during the first Monte Carlo step, the evolution of the optical depth is numerically resolved through first-order Eulerian integration [212]:

$$\tau(t) = \int_0^t n_i v_e \sigma_t(\varepsilon_e) dt'. \tag{3.14}$$

When the optical depth meets the value assigned to the emission probability, $\tau > \tau_{em}$, a photon with momentum parallel to v_e. Upon emission, a new optical depth is sampled for the next emission event of the electron. In the second Monte Carlo step, the photon energy is computed by solving the sampling equation [213],

$$\frac{1}{\sigma} \int_{\varepsilon_{\gamma_{min}}}^{\varepsilon_{\gamma_{max}}} \frac{d\sigma}{d\varepsilon_\gamma'} d\varepsilon_\gamma' = \xi. \tag{3.15}$$

where ξ is a new random number, interpreted as the cumulative distribution function, between 0 and 1.

3.4.2 Setting Bremsstrahlung Parameters in EPOCH

The EPOCH simulation code is predominantly controlled via a text file known as "input.deck" [214]. Within this file, users can manipulate the parameters of the bremsstrahlung features through the bremsstrahlung block. This block determines the settings and parameters specifically associated with the bremsstrahlung model, as demonstrated in Box (3.1).

In this block, the `use_bremsstrahlung` flag determines if bremsstrahlung processes are included in the simulation, and the `start_time` parameter establishes the point in the simulation timeline at which these processes begin. Furthermore, the `produce_photons` flag manages the production and tracking of photons in the simulation. If set to false, the simulation continues to account for the recoil effect on electrons due to photon emission but ceases to track the photons. Additional parameters, such as `photon_energy_min` and `photon_weight`, set the minimum energy required for a photon to be tracked and control the macro-particle weight of the produced photons, respectively. The `photon_weight` parameter, which must fall within the range 0.0 < `photon_weight` ≤ 1.0, allows the sampling of a larger number of photons.

In cases where the emphasis is on the location of photon generation rather than propagation, the `photon_dynamics` flag can be used to halt the core code from moving the photons, thus improving the speed of the simulation. Furthermore, the `use_bremsstrahlung_recoil` flag dictates whether the simulation includes the recoil of electrons following photon emission.

Listing 3.1: Exemplary bremsstrahlung block from an EPOCH input deck

```
begin:bremsstrahlung
use_bremsstrahlung = T
start_time = 0
produce_photons = T
photon_energy_min = 1 * keV
photon_weight = 1.0
photon_dynamics = F
use_bremsstrahlung_recoil = T
use_plasma_screening = F
end:bremsstrahlung
```

Finally, the `use_plasma_screening` flag permits the simulation to calculate the cross-section enhancement resulting from the diminished screening of the nuclear charge in ionized atoms. If this flag is set to false, the simulation omits this effect. The extensiveness of these parameters and flags gives users substantial flexibility in customizing the simulation of bremsstrahlung radiation and its effects within the EPOCH code.

3.5 Summary

In this chapter, we provided an overview of the methodologies and tools used in the analysis of PIC simulation codes. We discussed the EPOCH PIC code and elaborated on its capabilities and advanced computational features.

We then focused on the bremsstrahlung routine integrated within the EPOCH code, describing the two methodologies it employs based on the work of Vyskocil et al. [36] and Wu et al. [207]. Furthermore, we explained how the bremsstrahlung process is incorporated into the PIC loop using the Monte Carlo method and the calculation of the optical depth for photon emission. Finally, we discussed the bremsstrahlung block in the EPOCH input file, which allows users to manipulate bremsstrahlung features in the simulation.

Chapter 4

Suppression of Bremsstrahlung: Mechanisms and Effects

Studying high-energy physics phenomena requires understanding the various mechanisms by which particles interact with their surroundings. Bremsstrahlung emission is one such mechanism. In this process, a charged particle, typically an electron, emits radiation when accelerated or decelerated in the presence of another charged particle, such as a nucleus. This mechanism is crucial in various physical contexts, from particle accelerator operations to interpreting astrophysical observations. However, it has been demonstrated that the kinematics of this process necessitate the formation of high-energy electron radiation at a finite distance, known as the formation length. It has been found that various environmental factors have the potential to influence this process throughout the formation length, resulting in a variable bremsstrahlung cross-section.

This chapter begins with an explanation of the bremsstrahlung mechanism and its cross-section. The formation length is then examined, both in classical and quantum mechanical approaches, and the suppression factor, a quantity parameter for determining the extent of suppression, is defined. The chapter then examines common suppression mechanisms for bremsstrahlung emission, such as the Landau-Pomeranchuk-Migdal (LPM) effect, dielectric suppression effects, magnetic suppression effects, and pair-creation suppression. By analyzing their individual characteristics, we hope to provide an overview of the factors that influence bremsstrahlung emissions. We also hope to encourage and inspire readers to delve into subsequent chapters that investigate the magnetic suppression effect in greater detail, particularly in the context of high-intensity laser-plasma interactions.

4.1 Bremsstrahlung Mechanism

As described in Subsection (2.3.2), bremsstrahlung refers to the radiation emitted when a charged particle, such as an electron, is decelerated or deflected with another charged particle, such as a nucleus of an atom. The electrostatic force between a positively charged nucleus and an electron with a negative charge causes the electron to modify its trajectory and slow down, thereby releasing energy. This energy is emitted as electromagnetic radiation through a process known as bremsstrahlung. Figure 4.1 illustrates the basic process of electron-nucleus bremsstrahlung emission that takes place when an electron with energy ε_e is deflected by the microscopic electric field of a positively charged heavy nucleus. The electron loses energy and manifests as a photon with energy, $\varepsilon_\gamma = \varepsilon_e - \varepsilon_e'$ where ε_e' is the electron energy after the interaction. In this scattering process, the impact parameter b in the figure represents the perpendicular distance between the trajectory of an incoming particle and the center of the target particle, assuming no deflection.

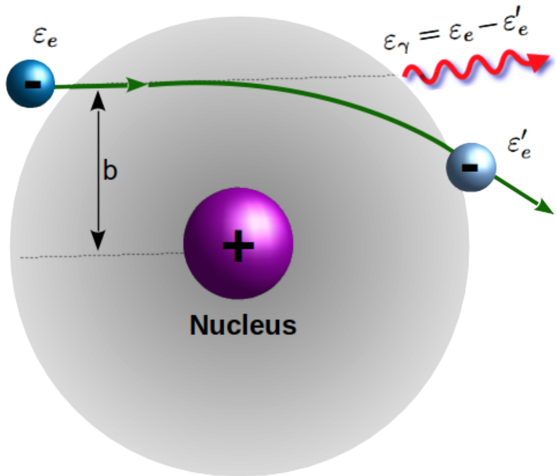

Figure 4.1: A schematic representation of the fundamental mechanism of electron-nucleus bremsstrahlung emission.

The nucleus can be screened by the charge distribution of atomic electrons, which may result in a reduced cross-section due to a decrease in the observed effective charge of the electron scattering by the atom. In the case of electron-ion bremsstrahlung, electrons are considered the primary emitters because relative accelerations are inversely proportional to masses [215]. The photon energies emitted during bremsstrahlung may vary from zero to the energy of the incoming electron. If the electron is only slightly deflected and loses a negligible amount of kinetic energy, the photon's energy could be extremely close to zero. This represents the minimum threshold. Theoretically, the photon's energy could be as high as the electron's initial kinetic energy (minus any residual kinetic energy if the electron does not stop completely). In other words, if the electron were to come to a complete halt after the interaction (a highly improbable occurrence), its entire kinetic energy would be converted into the energy of the photon. This is the maximum, or "cutoff" amount of energy.

The number of photons produced by a bremsstrahlung mechanism is highly dependent on the energy of the incident electron. The electrons with more energy generate a larger number of photons. The photon flux decreases monotonically as photon energy increases, reaching zero at the cutoff energy. The emission angle of these photons, relative to the direction of the incident electrons, also affects the spectrum. An increasing angle leads to a rapid decrease in intensity for all photon energies and a broadening of the spectrum, as the decrease with emission angle is more pronounced for high-energy photons.

In the case of non-relativistic particles, the energy loss resulting from radiation is negligible compared to the energy loss caused by collisions. Conversely, for ultra-relativistic particles, the situation is reversed: radiation-induced energy loss can surpass collisional energy loss and become the principal mechanism of energy loss [216].

In 1959, Koch and Motz [217] compiled and reviewed various cross-section calculations, measurements, and theoretical formulas along with their respective limits, primarily based on cross-sections computed in the first Born approximation[†], enabling analytical integration over the angles of the outgoing electrons and photons. The comprehensive information they gathered simplifies the process of making accurate predictions and offers a detailed overview of the diverse aspects of the bremsstrahlung process. Gluckstern and Hull [218] developed the Born approximation for the linear polarization of electron-nucleus bremsstrahlung. Kim and Pratt [219] calculated the classical bremsstrahlung spectrum, angular distribution, and polarization of scattered electrons in screened atomic potentials numerically. They observed noticeable differences in the calculated electron trajectories for cases with and without the screening effect. Since the plasma examined in this thesis is fully ionized, the influence of the screening effect on bremsstrahlung will not be discussed.

[†]The Born approximation is a perturbation method that assumes the interaction between the incident electron and the target nucleus is weak, thereby justifying the neglect of higher-order effects. In this approximation, the wave function of the incident electron is treated as a plane wave, with the radiation being emitted due to the electron's interaction with the Coulomb field of the target nucleus [see Appendix (A)].

4.1.1 Bremsstrahlung Cross-Section

The bremsstrahlung cross-section quantifies the probability that bremsstrahlung radiation will be emitted. In the non-relativistic regime, the energy of the participating charged particles is significantly less than their rest mass energy. As such, the bremsstrahlung radiation cross-section can be evaluated using classical electrodynamics [216]. Within this framework, an electron, when accelerated due to an inelastic collision with a nucleus carrying charge Z, emits bremsstrahlung of intensity [33] as expressed by the following equation:

$$\frac{d^2 I}{d\omega d\Omega} = \frac{Z^2 e^2 \omega^2}{4\pi^2 c^3} \left| \int \boldsymbol{n} \times d\boldsymbol{r} e^{i[\omega t - \boldsymbol{k}.\boldsymbol{r}(t)]} \right|^2, \tag{4.1}$$

where c represents the speed of light, ω is the radiation frequency, $\boldsymbol{n}$ is a unit vector pointing from the position of the charge towards the point of observation, and $d\Omega$ is an infinitesimal solid angle. Assuming, radiation is emitted when there is a sudden change in the velocity direction of an incident particle passing at an impact parameter of b. In the classical regime, its lower limit is determined by the classical radius of the particle $b^{(c)}_{min} = Ze^2/m_e v_e^2$, whereas its upper limit is approximated by $b^{(c)}_{max} \approx v_e/\omega$. Integrating over $d\Omega$ yields the following expression for the classical radiation cross-section of bremsstrahlung [216]:

$$\chi^{(c)}(\omega) = \int I(\omega, b)\ 2\pi b\ db \approx \frac{16}{3} \frac{Z^2 e^6}{c(m_e c^2)^2} \frac{1}{\beta^2} \ln\left(\frac{\lambda m_e v_e^3}{Ze^2 \omega}\right), \tag{4.2}$$

where λ is a unity order factor that arises due to uncertainty in the exact limits on impact parameters, and $\beta = v_e/c$. This equation is only valid when ($b^{(c)}_{max} \gg b^{(c)}_{min}$), setting a classical upper limit on the frequency spectrum to approximately $\sim m_e v_e^3/Ze^2$. By considering a quantum-mechanical lower limit on the impact parameter ($b^{(q)}_{min} \approx \hbar/m_e v_e$), the modified radiation cross-section can be expressed as follows:

$$\chi^{(q)}(\omega) \approx \frac{16}{3} \frac{Z^2 e^6}{c(m_e c^2)^2} \frac{1}{\beta^2} \ln\left(\frac{\lambda m_e v_e^2}{\varepsilon_\gamma}\right), \tag{4.3}$$

where $\varepsilon_\gamma = \hbar\omega$ represents the energy of the emitted photon. With this modification, the frequency spectrum of the quantum cross-section extends up to a maximum frequency ($\omega^{(q)}_{max} \sim m_e v_e^2/\hbar$). By considering the average velocity of the electron during the collision and assuming $\lambda = 2$, the bremsstrahlung cross-section can be represented by [216]:

$$\sigma_{BS}(\varepsilon_\gamma) \approx \frac{16}{3} \frac{1}{\varepsilon_\gamma} \frac{Z^2 e^6}{\hbar c(m_e c^2)^2} \frac{1}{\beta^2} \ln\left(\frac{(\sqrt{\varepsilon_e} + \sqrt{\varepsilon_e'})^2}{\varepsilon_\gamma}\right), \tag{4.4}$$

where ε_e and ε_e' correspond to the initial and final kinetic energies of the incident electron, respectively. Here, the interaction between the charged particle (emitter) and the nucleus is considered a perturbation problem, and the Born approximation is typically employed to describe the differential cross-section of bremsstrahlung radiation [220]. The non-relativistic formula is applicable for electron energies much smaller than the electron rest mass energy ($\varepsilon_e \ll m_e c^2$).

In contrast, the bremsstrahlung radiation for relativistic particles involves charged particles with energies comparable to or exceeding their rest mass energy. Hans Bethe and Walter Heitler in 1934 [221] proposed the first relativistic calculation of the cross-section of the bremsstrahlung process using the Born approximation. The theory assumes that the energy loss of a charged particle due to its interaction with atomic electrons in a medium can be treated as a series of independent interactions, each of which results in the emission of a photon. This simplification allows solving the bremsstrahlung problem in two steps rather than having to calculate the entire process all at once. The first step considers the electron's deflection in the atomic field, and the second step considers its interaction with the radiation field.

For an electron with energy ε_e radiating a photon with energy ε_γ, the Bethe-Heitler differential cross-section is calculated as follows [222]:

$$\frac{d\sigma_{BH}}{d\varepsilon_\gamma} = \frac{4\alpha r_e^2}{3\varepsilon_\gamma}\left[A(y) \times B(Z)\right] \tag{4.5}$$

where $d\sigma_{BH}$ is the Bethe-Heitler differential cross-section, $\alpha \approx 1/137$ is the fine-structure constant, and r_e is the classical electron radius. The resulting spectrum is proportional to ε_γ^{-1} and exhibits a sharp cutoff at high energies. The expression is a result of combining the contributions from scattering off atomic nuclei and atomic electrons. Here, $A(y)$ represents the contribution due to the dimensionless photon energy, $y = \varepsilon_\gamma/\varepsilon_e$,

$$A(y) = \left(y^2 + 2\left[1 + \left(1 - y^2\right)\right]\right) \tag{4.6}$$

and $B(Z)$ represents the dependence on the atomic number of the target, Z,

$$B(Z) = Z^2 \ln\left(184 Z^{-1/3}\right) + Z \ln\left(1194 Z^{-2/3}\right) + (1-y)\frac{Z^2 + Z}{3} \tag{4.7}$$

The first two terms in $B(Z)$ describe the logarithmic dependence on the atomic number, Z, which accounts for the different target materials' atomic structures. The third term accounts for the energy loss due to the interaction of the photon with the atomic nuclei and electrons, which is also dependent on the atomic number, Z. By integrating the differential cross-section over all possible photon energies, the total cross-section for bremsstrahlung radiation can be expressed as

$$\sigma_{BH} = \int_0^{\varepsilon_e} \frac{d\sigma_{BH}}{d\varepsilon_\gamma} d\varepsilon_\gamma. \tag{4.8}$$

Despite its common application and validation, the Bethe-Heitler formula has limitations. One such limitation is that the formula, in essence, is derived by considering radiation processes occurring in an individual, isolated atom. However, when extended to the radiation process within a medium at sufficiently high energies, the validity of the Bethe-Heitler theory can come into question [223]. Furthermore, the Bethe-Heitler formula does not account for environmental effects, even though the cross-section of the bremsstrahlung process can significantly vary based on the environment where the interaction occurs [224]. As a result, the formula might be insufficient for accurately describing the interaction when it takes place in a dense medium—where electrons might scatter multiple times—or in environments where macroscopic magnetic fields have a substantial influence on the interaction.

4.2 Formation Length and Suppression Factor

During the early 1950s, it became apparent that the classical model, which assumed the photon generated in the bremsstrahlung process by high-energy electrons to be instantaneous, was incomplete. The seminal work by Ter-Mikaelian [225] showed that bremsstrahlung can occur over significant path lengths along the particle's trajectory, particularly through relativistic particle scattering and radiation in a crystal. He demonstrated that as the energy of the incoming particle increases or the frequency of the photon decreases, the length at which bremsstrahlung occurs can extend to macroscopic dimensions. In addition, as the electron approaches the lattice spacing, the impact of the periodic structure becomes significant and requires consideration.

These studies demonstrated that photon emission is not a single-point, instantaneous event, but rather requires both time and space for the electron and photon to separate before the photon can be considered a "formed" particle [33, 226, 227]. This separation time is referred to as the formation time, t_{f0}, and its corresponding spatial domain is called the "formation (coherence) length", l_{f_0}. The 'f_0' subscript represents the length of an unsuppressed formation.

This refers to the distance that the final-state particles—specifically the scattered electron and the generated photon—require to separate and act as distinct particles. In order to precisely model the bremsstrahlung distribution, it becomes necessary to take formation length into account. In the following subsections, we will present a detailed explanation of the concept of formation length from both classical and quantum mechanical perspectives.

4.2.1 Classical Formation Length

In classical electrodynamics, the formation length is defined as the distance over which a charged particle emits radiation [228]. A photon is considered to be formed or created when it has traveled a distance equal to one reduced wavelength, $\lambda/2\pi$, from the electron [224]. This is essentially the point where the photon becomes separated from the electron due to a slight difference in velocities between the electron and the photon [224]. In this case, the relation between the electron and the photon is represented by:

$$\begin{aligned} ct_{f_0} &= l_{f_0} + \frac{\lambda}{2\pi} \\ v_e t_{f_0} &= l_{f_0} \end{aligned} \tag{4.9}$$

Here, $v_e = c\sqrt{1 - 1/\gamma^2}$ and c represent the electron's velocity and the speed of light, respectively. From Equation (4.9), the distance traveled by the electron is derived as:

$$l_{f_0} = \left(l_{f_0} + \frac{\lambda}{2\pi} \right) \left(1 - \frac{1}{\gamma^2} \right)^{1/2} \tag{4.10}$$

For a high-energy electron with $\gamma \gg 1$, this expression can be simplified as:

$$l_{f_0} \approx \frac{2\gamma^2 c}{\omega} \tag{4.11}$$

It is worth noting that the Expression (4.11) for the formation length can also be derived for low-energy photon emission by adopting another classical approach that considers the electron-photon coherence concept during the emission process. In classical electrodynamics, the radiation energy emitted by a charged particle moving along a trajectory $\boldsymbol{r}(t)$ is governed by Equation (4.1). The integral term on the right-hand side of Expression (4.1) describes how the motion of the charged particle leads to radiation emission. In fact, the phase factor, $\Phi = \exp[i(\omega t - \boldsymbol{k} \cdot \boldsymbol{r}(t))]$, is the main contributor to this integral over the formation time, t_{f_0} [33]. From this perspective, the phase factor of the electromagnetic process maintains coherence over the formation length, allowing the electron and photon to separate gradually [34].

From this hypothesis, the formation time can be derived as [229]:

$$t_{f_0} \approx \frac{1}{\omega}\left(1 - \frac{v_e}{c}\cos(\alpha)\right)^{-1}, \tag{4.12}$$

Here, α denotes the angle between the emitting electron's velocity and the direction of the photon radiation. Consequently, the longitudinal formation length (when $\alpha \to 0$) can be derived as:

$$l_{f_0} \approx \frac{1}{\omega}\left(1 - \frac{v_e}{c}\right)^{-1} v_e \approx \frac{2\gamma^2 c}{\omega}, \tag{4.13}$$

Note that the Expression (4.13) indicates that the formation length increases as the energy of the primary particle rises and as the energy of the photon decreases.

4.2.2 Quantum Formation Length

In quantum mechanics, the formation length refers to the minimum distance over which an electron interacts with a nucleus to emit a real photon. As the electron accelerates, a part of the virtual photon field that surrounds it shakes loose, resulting in the emission of a real photon [34]. According to the momentum conservation law, the longitudinal momentum transfer during this process can be expressed as [230],

$$q_{\parallel} = p_e - p'_e - p_\gamma, \tag{4.14}$$

where p_e and p'_e denote the electron's momenta before and after the interaction, respectively, and p_γ is the momentum of the emitted photon. For high-energy electrons emitting low-energy photons ($\varepsilon_e \gg \varepsilon_\gamma$), disregarding the photon emission angle and electron scattering results in a simplified expression for $q_{\parallel}$, given as,

$$q_{\parallel} = \frac{\varepsilon_\gamma m_e^2 c^3}{2\varepsilon_e(\varepsilon_e - \varepsilon_\gamma)}, \tag{4.15}$$

where m_e is the electron mass, c is the speed of light, and ε_e is the energy of the incident electron. Using the uncertainty principle† in the quantum-mechanical approach, the formation length l_{f_0} can be obtained as,

$$l_{f_0} \approx \frac{\hbar}{q_{\parallel}} = \frac{2\gamma^2 \hbar c}{\varepsilon^*_\gamma}, \quad \text{where} \quad \varepsilon^*_\gamma = \frac{\varepsilon_\gamma}{(1-y)} \tag{4.16}$$

†The uncertainty principle, known as Heisenberg's Uncertainty Principle, is one of the fundamental concepts in quantum mechanics. It states that it is impossible to simultaneously measure the exact position and momentum of a particle [231]. In other words, the more precisely one property is measured, the less precisely the other can be controlled or determined. The uncertainty principle can be mathematically expressed as: $\Delta x \Delta p \geq \frac{\hbar}{2}$ where $\hbar$ is the reduced Planck constant.

where $y = \varepsilon_\gamma/\varepsilon_e$. This expression shows the relation between the formation length and the momentum transfer in the longitudinal direction of a scattering event. In the limit of $\varepsilon_e \gg \varepsilon_\gamma$, Equation (4.16) coincides with Equation (4.13), which is a requirement of the correspondence principle. Both expressions were derived by considering the longitudinal component of the momentum transfer to the ion, emphasizing the significant role the longitudinal dimensions of the region play in bremsstrahlung processes. Moreover, these expressions demonstrate that the formation length for low-energy photons ($\varepsilon_\gamma \ll \varepsilon_e$) is identical under both quantum and classical analysis.

4.2.3 Suppression Factor

The cumulative emission amplitude over the formation length generates an emission probability, leading to the emission of bremsstrahlung photons by high-energy particles. In this context, the emission probability is significantly influenced by the particle's interaction with its surroundings during the formation period. Any interaction during the travel of the electron or photon through the formation length can disrupt coherence, thereby decreasing the effective formation length and the probability of emission. Even minor forces due to environmental factors acting over a formation length can destroy the required emission coherence. These mechanisms operate by modifying and reducing the total cross-section, thereby considerably diminishing the radiation yield.

Such modifications should be incorporated into the calculation of $q_\parallel$, and subsequently, the formation length. Note that in order to differentiate between unsuppressed and suppressed formation lengths, we represent the suppressed formation length as l_f. In Figure (4.2), we can see a schematic representation of the formation length in the bremsstrahlung process. The high-energy electron interacts with its surroundings, leading to multiple small deflections (for example), with angles exaggerated for better visualization.

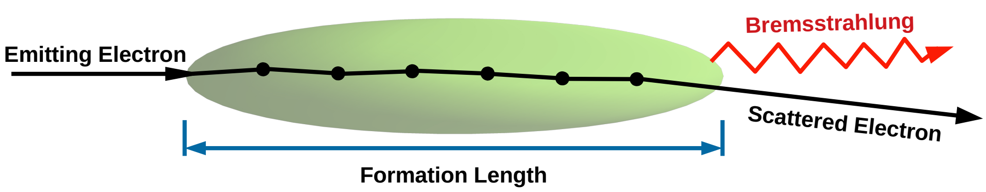

Figure 4.2: Illustration of formation length in the bremsstrahlung process, where a high-energy electron interacts with its surroundings, undergoes multiple small deflections (angles exaggerated for clarity), and emits nearly collinear bremsstrahlung radiation.

Given that the emission probability (i.e., differential cross-section) is proportional to the formation length, these adjustments often lead to a suppression of the Bethe-Heitler differential cross-section. This is achieved by multiplying the ratio of the suppressed formation length, l_f, by the unsuppressed one, l_{f0} [232],

$$S_{fac} = \frac{d\sigma_{fac}/d\varepsilon_\gamma}{d\sigma_{BH}/d\varepsilon_\gamma} \approx \frac{l_f}{l_{f0}}, \tag{4.17}$$

where S_{fac} is defined as a suppression factor that is influenced by environmental factors, and σ_{fac} represents the suppressed cross-section. Consequently, the measure of suppression could be estimated by analyzing the suppression factor.

4.3 Bremsstrahlung Suppression Mechanisms

The classification of Bremsstrahlung suppression mechanisms is based on environmental factors that disturb electrons or photons. These are examples of typical suppression effects:

4.3.1 Landau-Pomeranchuk-Migdal Effect

Landau and Pomeranchuk [223] found that bremsstrahlung and pair production formulas require revisions not only for crystalline materials but also for conventional amorphous substances. They identified limitations in the Bethe-Heitler theory regarding high-energy bremsstrahlung electrons, particularly when a high-energy particle traverses a dense medium. Under these circumstances, the particle is not just interacting with a single atom but encounters multiple 'soft' scatterings with a multitude of atoms within the medium. This leads to interference effects, as the quantum amplitudes from different interaction paths can either constructively or destructively interfere with each other. Such interference significantly alters the resultant radiation spectrum from what the Bethe-Heitler theory predicts for an isolated atom. This sequence of interactions results in a notably shorter mean free path of the electron compared to the formation length, subsequently leading to a reduction in the cross-section for bremsstrahlung.

To extend the theory of radiation from single-point scattering to radiation from total scattering within a single formation zone, Migdal employed quantum statistical methods to determine the cross-sections for pair production and radiation as a function of photon and electron energy. The multiple scattering effects on bremsstrahlung emission in high-energy physics are known as the Landau–Pomeranchuk–Migdal effect, or the LPM effect for short.

According to Molière's theory† of multiple scattering [233], the scattering process is the result of many small-angle scatterings, which can be treated as independent events. The charged particles do not lose a significant amount of energy while traversing the medium, meaning their velocity remains approximately constant. The deflection angles from individual scatterings are small compared to the total deflection angle. Based on these assumptions, Molière's theory derives an expression for the root-mean-square angle of multiple scattering, θ_0, as [233]:

$$\theta_0 \sim \frac{13.6, \mathrm{MeV}}{\beta c p_e}\sqrt{\frac{d}{X_0}}\left(1+0.038\ln\frac{d}{X_0}\right), \tag{4.18}$$

where $\beta = v_e/c$, p_e is the momentum of the electron, d is the thickness of the medium, and $X_0 = [4Z^2\alpha n r_e^2 \ln(183Z^{\frac{1}{3}})]^{-1}$ is the radiation length, which characterizes the length over which an incident particle statistically loses energy by emission of bremsstrahlung. In the case of an electron ($\beta \approx 1$), traveling through a thickness l_f, the angle of multiple scattering can be derived as [33]:

$$\theta_{MS} \sim \frac{\varepsilon_s}{\varepsilon_e}\sqrt{\frac{l_f}{X_0}}, \tag{4.19}$$

where ε_e is the energy of the electron. The term $\varepsilon_s = m_e c^2\sqrt{4\pi/\alpha}$ is approximately equal to 13.6 MeV, where $m_e c^2$ is the electron rest mass energy, and α is the fine-structure constant. Under the LPM effect, the entire formation zone functions as a single emitter, with radiation determined by the mean-square angle of scattering on a formation length, $\langle\theta_{MS}^2\rangle = (\varepsilon_s/\varepsilon_e)^2 l_f/X_0$. Upon considering this mechanism in the calculation of longitudinal momentum transfer and formation, one could obtain [232],

$$l_f = l_{f0}\sqrt{\frac{\varepsilon_\gamma E_{LPM}}{\varepsilon_e(\varepsilon_e-\varepsilon_\gamma)}}, \tag{4.20}$$

where $E_{LPM} = m_e^4 c^7 X_0/\hbar\varepsilon_s^2$. Thus, the multiple scattering suppression factor can be given as,

$$S_{LPM} = \sqrt{\frac{\varepsilon_\gamma E_{LPM}}{\varepsilon_e(\varepsilon_e-\varepsilon_\gamma)}}, \tag{4.21}$$

For $\theta_{MS} > \theta_{rad}$, the multiple scattering suppression effect becomes significant for $\varepsilon_\gamma < \varepsilon_{\gamma,LPM} = \varepsilon_e(\varepsilon_e-\varepsilon_\gamma)/E_{LPM}$. Here, θ_{rad} is the typical width of the photon

†The multiple scattering theory of Molière is a statistical model that defines the angular deflection of charged particles as they pass through a medium, such as a thin foil or a gaseous target. German physicist Gerhard Molière developed the theory in the late 1940s, based on the Coulomb scattering of charged particles by nuclei and electrons in the medium. It provides a method for estimating the angular dispersion of charged particles after they have traversed a given material thickness.

emission angle caused by the relativistic transformation of radiation from the frame of instantaneous rest to the frame of the laboratory [224].

The LPM effect has been extensively discussed in some literature [234–240], and confirmed by experiments conducted at higher energies. It became a crucial concept in the development of particle physics, especially in cosmic ray air showers [232, 241–245]. The first quantitative measurement of the suppression of 5 to 500 MeV photons from 8 and 25 GeV electrons due to the LPM effect was carried out by Anthony et al. [235] in the Stanford Linear Accelerator Center (SLAC) E-146 collaboration. They found that the LPM and Bethe-Heitler models predict contradictory results, and the LPM theory accurately predicts the suppression of bremsstrahlung to within 5%. They also concluded that if a target's thickness is equal to or less than the length of the LPM formation zone, suppression of the LPM should not occur.

4.3.2 Dielectric Suppression Effects

When a charged particle emits photons, these photons can interact with the atomic electrons in the medium through Compton scattering [33]. As a result, the contributions from different regions of the formation zone cease to add coherently, leading to a reduction in photon amplitude [230], which is known as the "dielectric suppression effect." This decrease in photon amplitude causes a decline in bremsstrahlung radiation from media with high dielectric constants. Consequently, the radiation spectrum, instead of following the Bethe-Heitler form in Equation (4.5), $1/\varepsilon_\gamma$, transitions to the spectrum defined by, ε_γ [246],

$$\frac{d\sigma}{d\varepsilon_\gamma} = \frac{16\alpha r_e^2 Z^2}{3\gamma^2\hbar^2\omega_p^2}\varepsilon_\gamma \ln\left(184Z^{-1/3}\sqrt{1+\frac{\gamma^2\hbar^2\omega_p^2}{\varepsilon_\gamma^2}}\right) \tag{4.22}$$

where α represents the fine-structure constant, r_e indicates the classical electron radius, Z is the atomic number of the medium, γ is the Lorentz factor of the charged particle, ω_p shows the plasma frequency of the medium, and ε_γ represents the energy of the emitted photon.

As a photon propagates through a medium characterized by a dielectric constant, $\epsilon(\varepsilon_\gamma) = 1 - (\varepsilon_p/\varepsilon_\gamma)^2$, where $\varepsilon_p = \hbar\sqrt{4\pi NZe^2/m_e}$, the interactions between the photon and the electrons present within the medium (with N representing the number of atoms per unit volume and Z the atomic number) can induce alterations in the photon's properties. Consequently, the relation between the photon's energy (ε_γ) and momentum (p_γ) is modified from $\varepsilon_\gamma = p_\gamma c$ in a vacuum to $\epsilon\varepsilon_\gamma = p_\gamma c$ within the medium. By incorporating this modification into Equation (4.14), the formation length can be derived as [230]:

$$l_f = \frac{2\hbar c \varepsilon_\gamma \gamma^2}{\varepsilon_\gamma^2 + \gamma \varepsilon_p^2} \tag{4.23}$$

Thus, the dielectric suppression, S_{die}, is given by:

$$S_{die} = \frac{\varepsilon_\gamma^2}{\varepsilon_\gamma^2 + \gamma^2 \varepsilon_p^2} \tag{4.24}$$

For $\varepsilon_\gamma < \varepsilon_{\gamma,die} = \gamma \varepsilon_p$, the dielectric suppression becomes significant; otherwise, the suppression factor does not alter the differential cross-section.

Experimental studies have measured the intensity of X-rays emitted by electrons passing through different materials and observed a suppression of the X-ray intensity emitted by electrons in these materials. For instance, in 1996, Anthony and his colleagues [230, 247] measured bremsstrahlung cross-sections for photons with energies ranging from 200 keV to 20 MeV produced by 8 and 25 GeV electrons interacting with carbon and gold targets. Their measurements indicate that the level of dielectric suppression predicted by theory is observed, with the measured cross-section reduced by up to 75% due to this effect.

4.3.3 Magnetic Suppression Effect

Bremsstrahlung emission can be effectively reduced by the presence of an external magnetic field, which introduces perturbations to the electron trajectory within the formation length. In such cases, the influence of strong macroscopic fields, which serve as significant environmental factors in the interaction region, can alter the high-energy electron path by deviating it more than the characteristic radiation angle, $\theta_{B/2} > \theta_{rad} \sim 1/\gamma$. Here, $\theta_{B/2} = \Delta p_e/p_e = eBl_f \sin\varphi_B / 2\varepsilon_e$ represents the deflection angle of an electron in a distance $l_f/2$ in a uniform magnetic field, with φ_B being the angle between the electron trajectory and the magnetic field [33]. The governing criteria for the magnetic suppression probability can be derived as follows:

$$\frac{\varepsilon_\gamma}{\varepsilon_e} < \varepsilon_{\gamma,B} = \gamma \frac{B}{B_{cr}} \tag{4.25}$$

where $B_{cr} = m_e^2 c^2 / e\hbar = 4.4 \times 10^9$ T is the Schwinger critical magnetic field. It is evident that significant probabilities for the magnetic suppression mechanism require both a strong magnetic field and high electron energies [34]. Consequently, as $\varepsilon_{\gamma,B}\varepsilon_e$ increases, the radiated photon spectrum becomes harder. This condition is crucial for various applications, such as the effective development of air showers in astrophysics studies [248, 249].

By considering $\theta_{B/2}$, treated similarly to $\theta_{MS/2}$ in the LPM effect, the formation length can be obtained as [33],

$$l_f = l_{f_0}\left[1+\left(\frac{m_e c B l_f}{\hbar B_{cr}}\right)\right]^{-1} \tag{4.26}$$

Subsequently, the magnetic suppression factor can be determined by [33]:

$$S_{MS} = \frac{l_f}{l_{f_0}} = \left(\frac{\varepsilon_\gamma m_e c^2 B_{cr}}{B\varepsilon_e(\varepsilon_e-\varepsilon_\gamma)}\right)^{2/3} \tag{4.27}$$

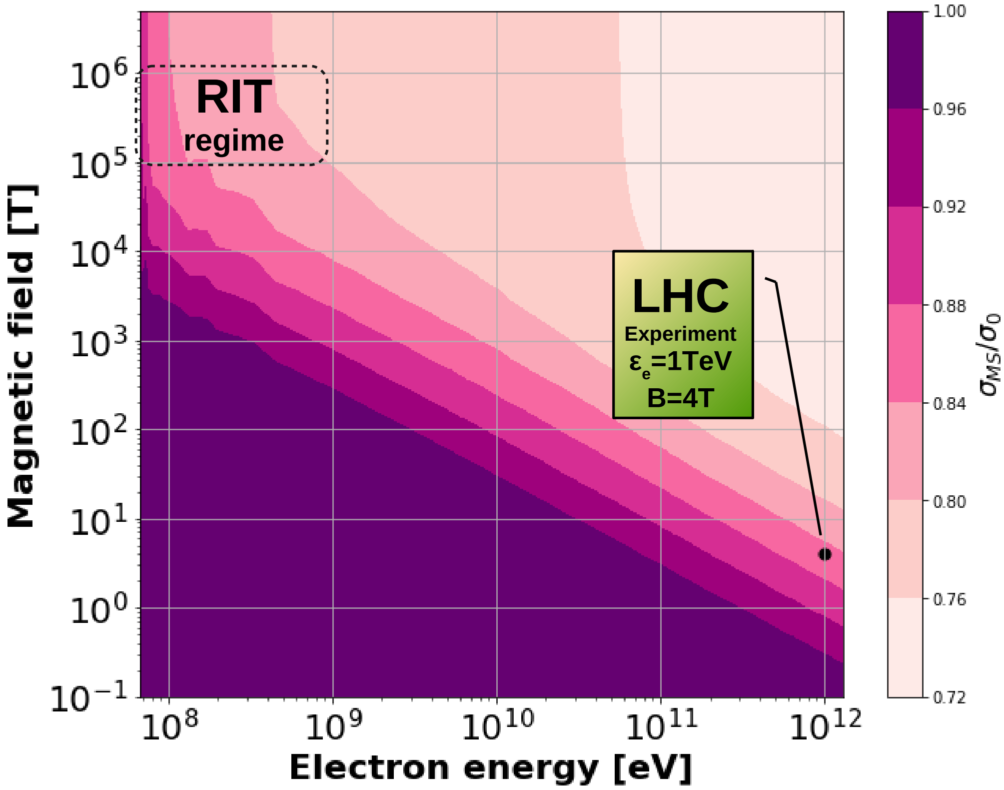

Figure 4.3: Magnetic suppression of bremsstrahlung emission. Color-coded is the relative reduction of the bremsstrahlung cross-section as a function of the electron energy and macroscopic magnetic field experienced by the electron, where σ_{MS} is the cross-section in the presence of the magnetic field (MS stands for the magnetic suppression effect) and σ_0 is the cross-section in the absence of the field. Highlighted are 1) the parameters at the Compact Muon Solenoid (CMS) experiment campaign at the Large Hadron Collider (marked as LHC) and 2) the parameters expected for high-intensity laser-plasma interactions due to the relativistically induced transparency (marked as RIT).

Figure (4.3) shows how the total bremsstrahlung cross-section changes for a given electron energy in the presence of a static uniform magnetic field due to the suppression. The plotted ratio is the relative reduction in the total emission due to magnetic suppression. It has been demonstrated that the suppression is significant for high-energy cosmic rays (10^{20} eV) in the earth's magnetic field (50 μT) [243]. In contrast to that, the bremsstrahlung emission by the electrons generated by the Large Hadron Collider (LHC) is unaffected by the earth's magnetic field. As marked over the figure (4.3), the 4 T magnetic field at the Compact Muon Solenoid experiment at the LHC is sufficient to suppress the emission of 1 TeV electrons.

By noting the changing counterlines on the figure, one can conclude that the general trend for magnetic suppression is that the strength of the magnetic field able to induce the effect goes up as the electron energy goes down. This is one of the reasons why the magnetic suppression effect has been so far ignored for the energetic electrons generated in laser-plasma interactions. Even for 10 GeV electrons, which is currently the upper limit of what can be achieved experimentally, the magnetic field strength must be in the range of 10^3 T for the suppression to be noticeable. Such a field is inaccessible to conventional magnets. However, the plasma magnetic fields in the regime of relativistically induced transparency (RIT) can be much stronger than 10^3 T, as already discussed in Chapter (1), which suggests that the effect of magnetic suppression can come into play. In Figure (4.3), the region corresponding to the RIT regime has been highlighted as well. The bremsstrahlung cross- section for 300 MeV electrons, the energy is not uncommon for high-intensity laser-plasma interactions, and should be suppressed by 20% in a 200 kT plasma magnetic field. The examination of magnetic suppression mechanisms within the RIT regime serves as the foundation for our research in this thesis.

4.3.4 Pair-Creation Suppression

If l_{f_0} reaches X_0, partially created photons can pair create, $\gamma \to e^+e^-$, disrupting coherence [34]. In this case, the pair creation suppression can be attributed to the multiple scattering. The longitudinal momentum transfer during this process can be expressed as [33],

$$q_{\|} = p_\gamma - p_e^+ - p_e^-, \tag{4.28}$$

where p_e^+ and p_e^- represent the momenta of the particles, respectively. Two separate pairs of particles should be subjected to multiple scattering in this situation. The lower-energy particle scatters further, which changes the longitudinal momentum transfer. Thus, the formation length can be obtained,

$$l_f = l_{f0}\sqrt{\frac{\varepsilon_\gamma E_{LPM}}{\varepsilon_e(\varepsilon_\gamma - \varepsilon_e)}}, \tag{4.29}$$

The suppression factor of pair creation influenced by the multiple scattering can be then derived as,

$$S_{p^{\pm},LPM} = \sqrt{\frac{\varepsilon_\gamma E_{LPM}}{\varepsilon_e(\varepsilon_\gamma - \varepsilon_e)}}, \tag{4.30}$$

Note that this suppression can be detected when

$$\varepsilon_e > E_p \sim \frac{X_0 \omega_{pe} \varepsilon_s}{\hbar c} \tag{4.31}$$

With this condition, a specific range of photon energy exists where this mechanism can be applied, $\varepsilon_{\gamma,e^-} \approx X_0\omega_p^2/2\hbar c < \varepsilon_\gamma < \varepsilon_{\gamma,e^+} \approx 2\hbar c \varepsilon_e(\varepsilon_e - \varepsilon_\gamma)/X_0\varepsilon_s^2$ [34]. Within this region, the photon spectrum is suppressed by ε_γ, resulting in a constant $d\sigma/d\varepsilon_\gamma$. Dielectric suppression is the dominant effect when $\varepsilon_\gamma < \varepsilon_{\gamma,e^-}$, whereas the LPM effect becomes dominant for $\varepsilon_\gamma > \varepsilon_{\gamma,e^+}$.

In addition to the LPM effect, the presence of a strong magnetic field can also be attributed to pair suppression [33]. The strong magnetic field can cause pair deflection, reducing coherence. The suppression factor of pair creation influenced by the magnetic field is expressed as [33],

$$S_{p^{\pm},B} = \left(\frac{\varepsilon_\gamma m_e c^2 B_{cr}}{B_{ext}\varepsilon_e(\varepsilon_\gamma - \varepsilon_e)}\right)^{2/3} \tag{4.32}$$

where $B_{cr} = 4.4 \times 10^9$ T is the Schwinger critical magnetic field.

4.4 Suppression Mechanisms and Their Interplay

As seen in the previous section, bremsstrahlung emission is influenced by various suppression mechanisms that each shape the emitted photon spectrum in different energy regions. This section illustrates these mechanisms and how they collectively determine the emitted photon spectrum. Figure (4.4) schematically depicts the expected bremsstrahlung spectrum $d\sigma/d\varepsilon_\gamma$, considering mentioned suppression mechanisms. It highlights five specific regions of photon energy, each dominated by a distinct suppression mechanism.

In the first region and for the lowest photon energy range ε_{γ,e^-}, dielectric suppression is the primary determinant, modifying the spectrum such that $d\sigma/d\varepsilon_\gamma \propto \varepsilon_\gamma$. Between ε_{γ,e^-} and ε_{γ,e^+}, the domination shifts to pair creation suppression. As we move further, between ε_{γ,e^+} and $\varepsilon_{\gamma,B}$, the magnetic suppression effect is pronounced, and from $\varepsilon_{\gamma,B}$ to $\varepsilon_{\gamma,LPM}$, the Landau-Pomeranchuk-Migdal (LPM) effect becomes most influential, altering the photon spectrum to $d\sigma/d\varepsilon_\gamma \propto 1/\sqrt{\varepsilon_\gamma}$. Above $\varepsilon_{\gamma,LPM}$,

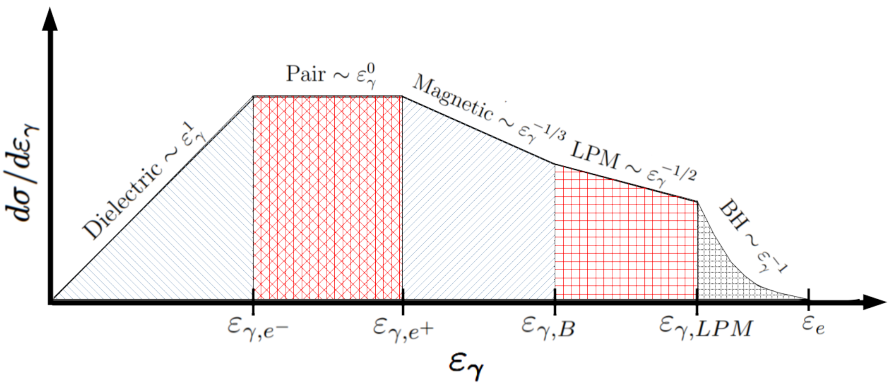

Figure 4.4: Diagram illustrating the expected bremsstrahlung spectrum $d\sigma/d\varepsilon_\gamma$ with multiple suppression factors involved.

as the photon energy approaches the energy of the incoming electron, the spectrum resembles the Bethe-Heitler regime.

However, it is crucial to stress that the conditions for each suppression mechanism to occur depend on several factors, including the target material. These factors could alter the boundaries or even render one or more mechanisms insignificant. For instance, for low-Z targets, the threshold for the dielectric effect might exceed the threshold for the LPM effect. In such cases, no LPM suppression occurs [250].

Table 4.1: Summary of different bremsstrahlung suppression mechanisms.

Mechanism	**Factor**	$d\sigma/d\varepsilon_\gamma$ **Scaling**	**Maximum** ε_γ
Bethe-Heitler	-	ε_γ^{-1}	ε_e
LPM	Multiple scattering	$\varepsilon_\gamma^{-1/2}$	ε_{LPM}
Magnetic	Magnetic field	$\varepsilon_\gamma^{-1/3}$	$\varepsilon_{\gamma,B}\varepsilon_e$
Pair Creation	Pair creation	ε^0	$\varepsilon_{\varepsilon_\gamma,e^+}$
Dielectric	Photon interactions	ε_γ^1	$\varepsilon_{\gamma,\text{die}}$

Table (4.1) summarizes the main characteristics of bremsstrahlung suppression mechanisms, including the scaling of the emitted photon spectrum and the maximum photon energy associated with each mechanism.

4.5 Summary

This chapter provided an analysis of the suppression mechanisms of bremsstrahlung emission and their effects on the emitted photon spectrum. The key concepts discussed include the bremsstrahlung mechanism, cross-section, formation length, and suppression factor. We had an overview of the various suppression mechanisms that can impact bremsstrahlung emissions. The Landau-Pomeranchuk-Migdal (LPM) effect and the dielectric suppression effect were discussed, both of which involve multiple scattering of electrons leading to a reduction in bremsstrahlung emission. The chapter also covered the magnetic suppression effect, which occurs when an external magnetic field disrupts the electron's path within the formation length. The influence of macroscopic fields can deviate the high-energy electron path by more than the characteristic radiation angle, thus suppressing bremsstrahlung emission. This concept holds significant importance in cosmic ray behavior, and the design and operation of particle accelerators, among others. In addition, it provides a concise overview of this effect as the primary suppression mechanism studied in this thesis. In the following chapters, we discuss this topic in more detail. Finally, the interplay between these mechanisms was examined, revealing distinct regions in the emitted photon spectrum dominated by specific suppression mechanisms.

Chapter 5

Modeling Magnetic Suppression of Bremsstrahlung

The objective of this chapter is to present a physics-based mathematical model for magnetic suppression of bremsstrahlung. As discussed in the preceding chapter, the presence of the macroscopic field can affect the formation length of the emitted radiation and, consequently, the bremsstrahlung cross-section. In addition, because we intend to apply this model to the laser-plasma interaction simulations, which involve both electric and magnetic fields, we have extended the analysis employed for the magnetic suppression to include the electric field.

Our analysis begins by determining the formation lengths under two scenarios: unsuppressed and suppressed. This step allows us to define the suppression factor, an essential measure for evaluating the decrease in emission probability. Following this, we introduce and derive an extended suppression factor for the electric-magnetic suppression mechanism Finally, we compare our derived suppression factors and those previously reported in the literature, emphasizing the similarities and differences between them.

5.1 High-Field Bremsstrahlung Suppression Model

In this section, we present a derivation of the suppression factor for bremsstrahlung from a quantum mechanical perspective, taking into account the presence of a macroscopic field as an environmental factor. Our approach follows that of Ref. [33]. First, we derive a general form of the suppression factor capable of modeling the macroscopic high-field suppression of bremsstrahlung emission. Then, we demonstrate that the derived formula can reproduce the suppression factors found in the literature under the conditions of no electric field and small angle approximation.

Before beginning the process of derivation, it is essential to first consider that the formation length of the bremsstrahlung process in our derivation is determined by the uncertainty principle in quantum mechanical calculations. The underlying physical reason is that the bremsstrahlung process kinematics necessitate a transfer of a small amount of longitudinal momentum to the ion. This, in turn, requires the interaction to occur over a large longitudinal distance scale according to the uncertainty principle, as illustrated in Equation (4.16). To distinguish between the formation length in the undisturbed state and that in the disturbed state due to external fields, we denote l_{f_0} as the undisturbed formation length and l_f as the disturbed formation length, respectively. Moreover, throughout this derivation, we assume that the transferred longitudinal momentum to the ion is in the direction of the emitting electron.

5.1.1 Derivation of the Formation Length

Let us begin with the case of a non-relativistic electron in the bremsstrahlung process. As seen in Figure 5.1(a) the emitting electron is influenced by a multiple scattering due to an external factor (e.g., LPM mechanism) and finally has emitted a photon. Note that all deflections depicted in Figure (5.1) have been exaggerated for the sake of visibility. The point here is that the emitted photon cannot resolve features smaller than its wavelength. In the context of the bremsstrahlung process at extremely high energies, the application of a Lorentz boost transformation[†] results in two primary changes: an increase in the photon formation length and a decrease in the emitted photon's wavelength, as illustrated schematically in Figure 5.1(b). The formation length increases by a Lorentz factor due to time dilation in special relativity, causing the photon emission process to appear extended in the boosted

[†]A Lorentz boost is a mathematical transformation used to convert the measurements of physical properties (such as position, time, and velocity) from one reference frame to another. It is particularly crucial when examining objects moving at speeds approaching the speed of light, where simple velocity addition fails due to special relativity effects.

frame and subsequently increasing the formation distance [227]. This phenomenon can also be observed in Equation (4.16).

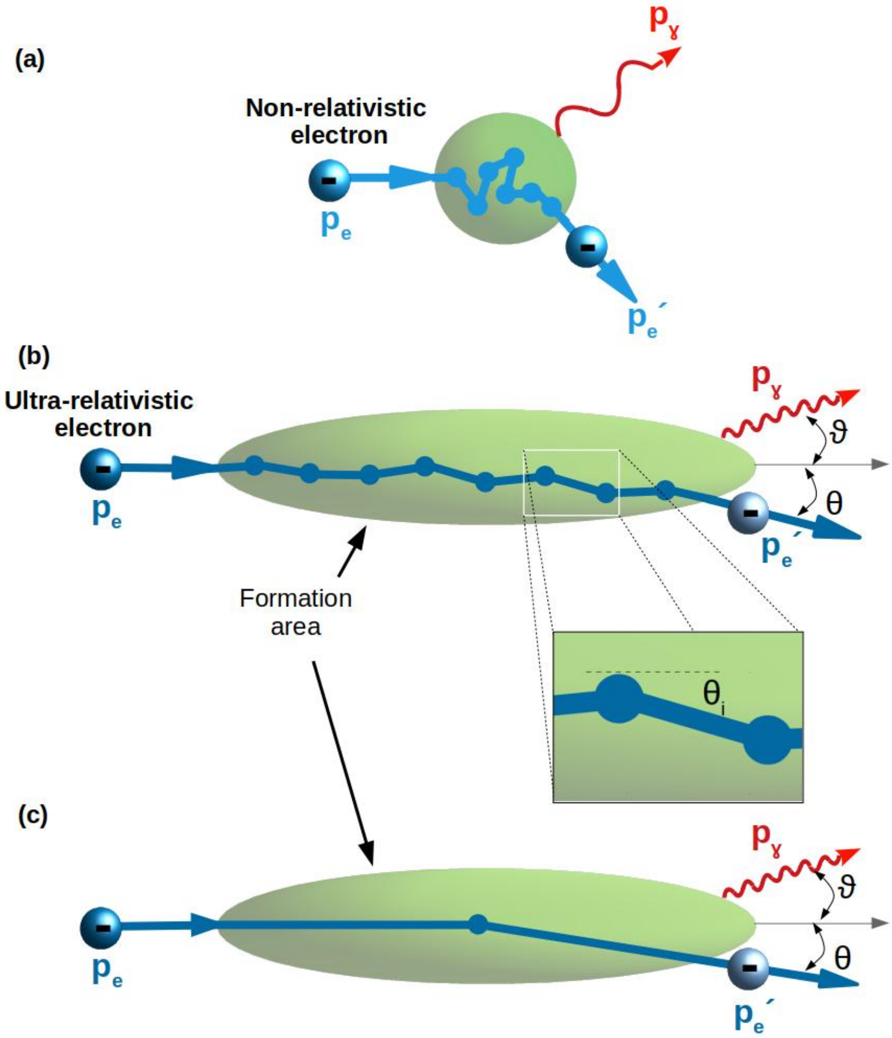

Figure 5.1: Diagram depicting the bremsstrahlung process impacted by typical multiple scattering in (a) non-relativistic and (b-c) relativistic settings. Scattering angles are purposely exaggerated in this illustration for clarity. An enlarged detail in (b) displays the ith scattering of an electron within the formation length, where θ_i is much smaller than ϑ. It is noteworthy that the photon cannot distinguish between scenarios (b) and (c).

Simultaneously, the wavelength of the emitted photon in the boosted frame contracts by the same Lorentz factor. This change arises from the relativistic Doppler effect, which occurs when a radiation source, such as the electron-ion collision in this case, moves relative to an observer. Consequently, the photon cannot distinguish between the situations depicted in Figure 5.1(b), which displays the accumulated deflections of the electron throughout the entire formation length, and Figure 5.1(c), which illustrates the scattered electron deflected by the net angle, θ, within the formation length. It is important to note that a photon emitted at an angle ϑ from an ultra-relativistic electron is not highly sensitive to the electron's local minor deviations (θ_i) throughout the electron's trajectory within the formation length, as these deviations are considerably smaller than ϑ. Consequently, the photon emission angle will be smaller or equivalent to the net deflection angle of the electron along the formation length, $\vartheta \approx \theta$. For a more comprehensive discussion regarding the treatment of the bremsstrahlung process in QED with respect to the formation length, readers are encouraged to refer to Arnold's extensive study in Ref. [227].

The significance of the formation length is further emphasized when environmental factors (such as high fields) can disrupt the electron's trajectory noticeably. Such disturbances result in an increase in the electron's local deviations (θ_i), making the photon emitted from the electron sensitive to these deflections. Consequently, as $\theta > \vartheta$ increases, momentum transfer to the ion increases, and the formation length decreases. The shortening of the formation length can undermine the coherence of the bremsstrahlung process, diminishing the emission probability. In such a scenario, the electron's deflection is influenced not only by the ion's Coulomb force but also by the macroscopic fields. Consequently, the electron scattering angle becomes non-negligible, as illustrated in figure (5.2).

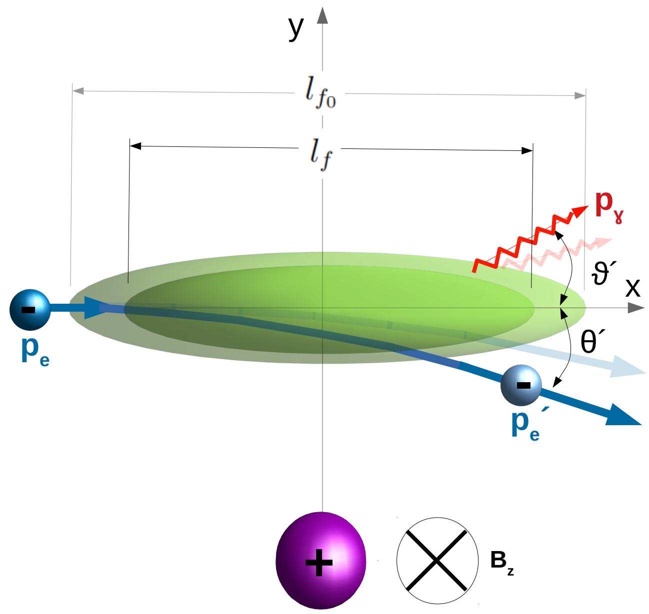

Figure 5.2: Representation of the bremsstrahlung process in an electron-ion collision in the presence of a macroscopic magnetic field, leading to increasing electron deflection and reducing formation length.

Building upon Klein's methodology for deriving the formation length for multiple scattering mechanisms in both classical and quantum approaches, as detailed in Ref. [33], we partition the interaction zone into two sections: before and after radiation.This approach is employed because a high-energy electron experiences a non-negligible deflection within a region defined by the formation length (due to the combined influence of the ion's electric field and external magnetic field). Bremsstrahlung amplitudes can interfere with one another before and after scattering, lowering the amplitude of bremsstrahlung photon emission. A strategic choice in evaluating such an effect is to divide the interaction zone into two sections (i.e., situate the origin of the coordinate system at the center of the formation length).

Let's first consider the conservation of energy and momentum when this ultra-relativistic electron with energy ε_e collides with an initially immobile ion and emits a forward-directed, low-energy photon with energy ε_γ:

$$\varepsilon_e = \varepsilon_e' + \varepsilon_\gamma + \varepsilon_i', \tag{5.1}$$

$$\mathbf{p}_e = \mathbf{p}_e' + \mathbf{p}_\gamma + \mathbf{p}_i', \tag{5.2}$$

Here, $\mathbf{p}_e$ is the momentum of the electron prior to the collision, and $\mathbf{p}_e'$, $\mathbf{p}_\gamma$, and $\mathbf{p}_i'$ are the momenta of the electron, emitted photon, and ion after the collision. It is worth noting that the recoil energy of an ion in the case of elastic scattering can be estimated to be on the order of $\mathcal{O}(10^{-4} \times \varepsilon_e/\gamma^2)$ for relativistic electron scattering at a small angle, $\theta = \mathcal{O}(1/\gamma)$, from a Carbon ion. This energy is even smaller for inelastic scattering and will therefore be neglected for the rest of the derivation.

It is assumed that this process occurs in an xy-plane, with the incoming electron propagating in the x direction. By designating θ as the scattering angle of a relativistic electron and ϑ as the angle of photon emission with respect to x direction†, Equation (5.2) can be decomposed into its constituent x and y components,

$$\begin{cases} p_{e,x} - p_{i,x}' = p_e' \cos(\theta) + p_\gamma \cos(\vartheta), \\ \qquad\quad p_{i,y}' = p_e' \sin(\theta) - p_\gamma \sin(\vartheta), \end{cases} \tag{5.3}$$

Rearranging Equation (5.3) and incorporating Equation (5.1) we obtain, for relativistic particles ($\varepsilon_e, \varepsilon_e' \gg m_e c^2$),

$$\begin{aligned} \frac{p_{i,x}'}{m_e c} \approx{}& \frac{1}{2}\frac{\varepsilon_\gamma m_e c^2}{\varepsilon_e(\varepsilon_e - \varepsilon_\gamma)} \\ &+ \left(1 - \frac{\varepsilon_\gamma}{\varepsilon_e}\right)\frac{\varepsilon_\gamma}{m_e c^2}[1 - \cos(\Theta_{def/2})], \end{aligned} \tag{5.4}$$

where m_e is the electron mass, c is the speed of light, and $\Theta_{def/2} = \theta + \vartheta$. The maximum probability of emitting a bremsstrahlung photon is associated with the

†Note that, for the sake of simplicity, the prime symbol used for angles (depicted in Figure (5.2)) has been omitted.

maximum coherence length and, according to the uncertainty principle, the corresponding minimum momentum transfer to the ion. The minimum value of $p'_{i,x}$ is achieved when $\theta = \vartheta = 0$. Under these conditions, equation (5.4) simplifies as follows:

$$\frac{p'_{i,min}}{m_e c} \approx \frac{1}{2} \frac{\varepsilon_\gamma m_e c^2}{\varepsilon_e(\varepsilon_e - \varepsilon_\gamma)}. \tag{5.5}$$

Using the uncertainty principle, this maximal coherence length is defined as distance l_{f0} and is known as the undisturbed formation length.

$$l_{f0} \approx \frac{\hbar}{p'_{i,min}} = \frac{2\hbar}{m_e c} \frac{\varepsilon_e(\varepsilon_e - \varepsilon_\gamma)}{\varepsilon_\gamma m_e c^2}, \tag{5.6}$$

where $\hbar$ is the Planck constant. Note that $\hbar/m_e c \approx 3.86 \times 10^{-13}$ m is the Compton wavelength of the electron. For $\varepsilon_e = 100$ MeV and $\varepsilon_\gamma = 0.1$ MeV, we have $l_{f0} \approx 0.15\ \mu m$, so the formation length is a non-negligible fraction of the wavelength ($\sim 1\ \mu m$) for an optical laser.

To calculate the suppressed formation length, we apply the uncertainty principle to equation (5.4),

$$l_f \approx \frac{\hbar}{p'_{i,x}} = l_{f0} \left[1 + \frac{2(\varepsilon_e - \varepsilon_\gamma)^2}{m_e^2 c^4}[1 - \cos(\Theta_{def/2})]\right]^{-1}, \tag{5.7}$$

It is noteworthy that due to the substantially larger transverse momentum transfer in comparison to the longitudinal one, i.e., $p'_{i,y} \gg p'_{i,x}$, the associated transverse formation length $\sim \hbar/p'_{i,y}$ becomes significantly smaller. Therefore, it is generally considered less relevant in this specific context.

Equation (5.7) offers a method for calculating the suppressed formation length in a radiation process by taking into account the initial formation length (unsuppressed) and the energy and angular characteristics of the involved particles, which are influenced by the presence of macroscopic high fields in the surrounding environment. Note that for relativistic electrons ($\varepsilon_e \gg m_e c^2$), and when the electron scattering angle exceeds the emission angle $\theta > \vartheta \sim 1/\gamma$ due to additional deviations resulting from macroscopic fields, $\Theta_{def/2} \approx \theta$ can be considered. The suppression factor's dependence on the deflection angle serves as a valuable tool for investigating the influence of external fields on the bremsstrahlung suppression.

5.1.2 Suppression Factor in High Fields

As detailed in Section (4.2.3), the suppression factor, S_{fac}, given by Equation (4.17), is defined as the ratio of the suppressed (reduced) formation length, l_f, to the formation length in vacuum (unsuppressed), l_{f0}. To estimate the electric-magnetic suppression (EMS) effect, which is the suppression of bremsstrahlung caused by the concurrent presence of electric and magnetic fields, we substitute l_f from Equation (5.7) into Equation (4.17). The suppression function in high fields, S_{HF}, can be obtained as follows:

$$S_{HF}(\varepsilon_e, \varepsilon_\gamma, \Theta_{def/2}) = \frac{l_f}{l_{f0}} = \left[1 + \alpha_1[1 - \cos(\Theta_{def/2})]\right]^{-1}, \tag{5.8}$$

where $\alpha_1 = 2(\varepsilon_e - \varepsilon_\gamma)^2/m_0^2c^4$. As seen in this expression, the suppressed factor is a function of electron and photon energies as well as the deflection angle, which serves as an indicator of the environmental macroscopic fields. It essentially quantifies the extent to which the medium reduces the formation length and, consequently, the emission probability in comparison to that in an unsuppressed state. If $S_{HF} < 1$, it indicates that the formation length has been shortened compared to that in an unsuppressed one, leading to the suppression of the bremsstrahlung cross-section.

The variation of the suppression factor with the angle of deflection proves to be a valuable method for investigating the influence of external fields on bremsstrahlung suppression. To accomplish this, we initially define $\tilde{\mathscr{E}}_{ext}$ as a factor representing electron deflection due to the Lorentz force's transverse electric and magnetic fields. In this case, it is possible to reformulate Equation (5.8) by replacing $\Theta_{def/2}$ with deflection angle due to $\tilde{\mathscr{E}}_{ext}$,

$$\Theta_{\tilde{\mathscr{E}}/2} = \arctan(\frac{\Delta p_\perp}{p}) = \arctan(\frac{e\tilde{\mathscr{E}}_{ext}l_f}{2\gamma m_e c^2}), \tag{5.9}$$

where γ is the relativistic factor, and we assumed that $v_e \sim c$. Consequently, the electric-magnetic suppression factor for ($\Theta_{\tilde{\mathscr{E}}/2} > 1/\gamma$) can be expressed as follows:

$$\begin{aligned} S_{\tilde{\mathscr{E}}}\left(\varepsilon_e, \varepsilon_\gamma, \tilde{\mathscr{E}}_{ext}\right) &= \left[1 + \alpha_1\left(1 - \frac{1}{\sqrt{1 + (\alpha_2 l_f)^2}}\right)\right]^{-1} \\ &= \left[1 + \alpha_1\left(1 - \frac{1}{\sqrt{1 + (\alpha_2 l_{f0} S_{\tilde{\mathscr{E}}/2})^2}}\right)\right]^{-1}, \end{aligned} \tag{5.10}$$

where $\alpha_2 = \tilde{\mathscr{E}}_{ext} m_e c/2\gamma E_{cr}\hbar$ and $E_{cr} = m_e^2c^3/e\hbar = 1.3 \times 10^{18}$ V/m denotes the Schwinger critical electric field. In the equation above, we have obtained a concise form for the electric-magnetic suppression function by simplifying the expression utilizing the trigonometric equation $\cos(\arctan(x)) = 1/\sqrt{1 + x^2}$, which relates the tangent and cosine functions. It is crucial to recognize that the suppression function,

$S_{\tilde{\mathcal{E}}}$, is an implicit function, meaning it cannot be explicitly expressed in terms of the other variables. To determine its value, one must employ numerical methods, which are explained in Chapter (6).

It is important to note that the suppression function should be applied as a multiplicative correction factor to the original Bethe-Heitler differential cross-section:

$$\frac{d\sigma_{\tilde{\mathcal{E}}}}{d\varepsilon_\gamma} = S_{\tilde{\mathcal{E}}}\left(\varepsilon_e, \varepsilon_\gamma, \tilde{\mathcal{E}}_{ext}\right) \frac{d\sigma_{BH}}{d\varepsilon_\gamma}, \tag{5.11}$$

Here, $\sigma_{\tilde{\mathcal{E}}}$ represents the total cross-sections with the electric-magnetic suppression effect. In the limit of the electric field, the suppression mechanism depends only on the presence of the magnetic field, and the suppression factor is calculated by selecting the angle of electron deflection in the external magnetic field:

$$\Theta_{B/2} = \arctan(\frac{eB_{ext}l_f}{2\gamma m_e c}), \tag{5.12}$$

Analogous to Equation (5.10), we can derive the magnetic suppression function, which is expressed as follows:

$$S_B\left(\varepsilon_e, \varepsilon_\gamma, B_{ext}\right) = \left[1 + \alpha_1 \left(1 - \frac{1}{\sqrt{1 + (\alpha_2^* l_{f_0} S_{B/2})^2}}\right)\right]^{-1}, \tag{5.13}$$

where $\alpha_2^* = B_{ext} m_e c / 2\gamma B_{cr}\hbar$ and $B_{cr} = m_e^2 c^2 / e\hbar = 4.4\times10^9$ T denotes the Schwinger critical magnetic field. The modified differential cross-section is given by,

$$\frac{d\sigma_B}{d\varepsilon_\gamma} = S_B\left(\varepsilon_e, \varepsilon_\gamma, B_{ext}\right) \frac{d\sigma_{BH}}{d\varepsilon_\gamma}, \tag{5.14}$$

5.2 Comparison with Previous Work: Klein's Suppression Function

It is worth emphasizing that the momentum transfer derived in the previous section, given by Equation (5.4), represents a general form. This expression can be simplified by employing a small-angle approximation if one wants to neglect higher-order terms in the deflection angle and assuming ($\varepsilon_e \gg \varepsilon_\gamma$), similar to the approach in Ref. [33]. Consequently, we obtain:

$$\frac{p'_{ion,x}}{m_e c} \approx \frac{1}{2} \frac{\varepsilon_\gamma m_e c^2}{\varepsilon_e(\varepsilon_e - \varepsilon_\gamma)} + \frac{1}{2} \frac{\varepsilon_\gamma}{m_e c^2} \Theta^2_{def/2}, \tag{5.15}$$

Upon substituting the deflection angle for the magnetic field, as given by Equation (5.12), one can retrieve the derivation presented by Klein in Ref. [33] in the limit of strong magnetic suppression ($l_f \ll l_{f_0}$):

$$S_B^* \left(\varepsilon_e, \varepsilon_\gamma, B_{ext}\right) = \left[\frac{\varepsilon_\gamma E_B}{\varepsilon_e(\varepsilon_e - \varepsilon_\gamma)}\right]^{2/3}, \tag{5.16}$$

where $E_B = m_e c^2 B_{cr}/B_{ext}$. Let us now compare our derived suppression fac-

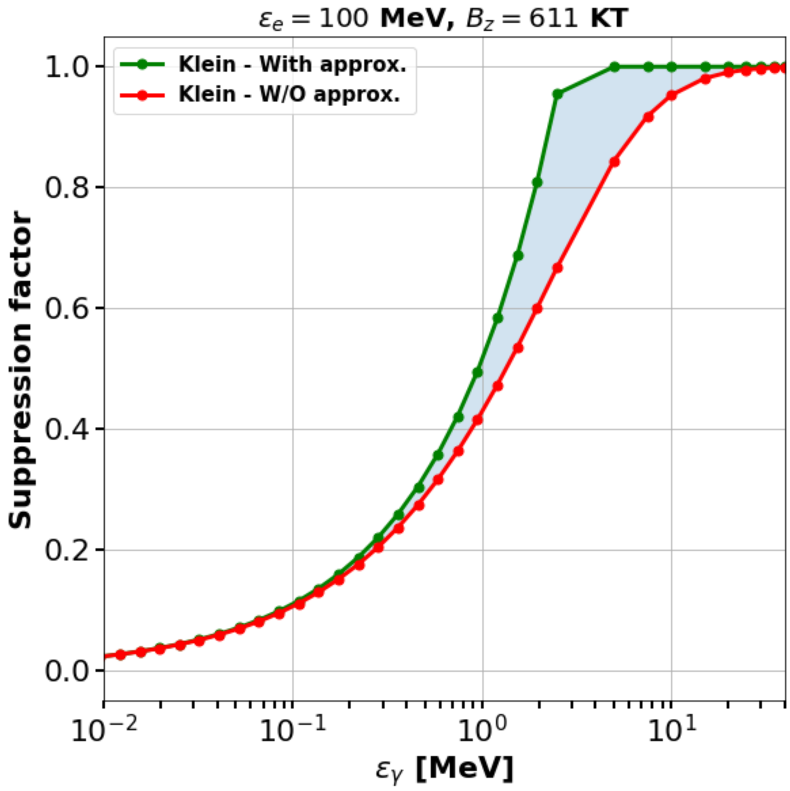

Figure 5.3: Comparing the suppression factor obtained from Klein's formula with (5.16) and our formula (5.13) without small-angle approximation for ε_e = 100 MeV and $B_z = 611$ KT.

tor (5.13), with that obtained by Klein (Ref. [33]) similar to factor (5.16). To visualize the similarities and differences between the two functions, we have plotted both suppression factors as a function of photon energy, ε_γ, for specific electron energy, $\varepsilon_e = 100$ MeV, and an external magnetic field, $B = 611$ kT, in Figure (5.3).

This figure illustrates the key features and deviations between our approach and Klein's. It can be observed that both factors exhibit a similar overall trend, with the suppression increasing as the photon energy decreases, as we have already expected from Expression (4.17). However, there are noticeable differences in the behavior of the functions at certain energy ranges, especially when it is increasing. This may be attributed to the distinct approximations such as small-angle approximation by which the higher orders are ignored and or other assumptions employed in each derivation like assuming strong magnetic suppression, $(l_f \ll l_{f_0})$ in Klein's derivation.

The implications of these discrepancies are twofold. Firstly, they highlight the importance of understanding the underlying assumptions and approximations in the derivation of suppression factors, as these can significantly impact the results. Secondly, the differences may provide insights into possible refinements or alternative formulations of the suppression factor that could be explored in future research.

5.3 Summary

In this chapter, we introduced the high-field bremsstrahlung suppression model, which is essential for understanding the impact of external fields on the emission of bremsstrahlung radiation. We derived the unsuppressed formation length, which represents the formation length in an unsuppressed state, and the suppressed formation length, which accounts for the presence of high fields. This allowed us to establish the suppression factor in high fields, a crucial quantity for determining the extent to which the emission probability is reduced compared to that in an unsuppressed state.

To illustrate the applicability of our model, we derived the electric-magnetic suppression factor and the magnetic suppression factor, which can be utilized to compute the suppression factor for various electric and magnetic fields. These suppression factors were formulated by considering the impact of electron deflection in the presence of external fields.

We then compared our derived suppression factors with the well-established Klein's suppression factor. Although both factors exhibited similar overall trends, we observed differences in their behavior at certain energy ranges, which were attributed to the distinct approximations and assumptions employed in each derivation.

Chapter 6

Implementation of Bremsstrahlung's Suppression into PIC code

This chapter explains the technical development and integration of the magnetic suppression (MS) and electric-magnetic suppression (EMS) models into the EPOCH particle-in-cell code, particularly into its bremsstrahlung module.

We will initiate the discussion by outlining how the suppression models were integrated into the EPOCH code and how this integration affected the bremsstrahlung module. During this procedure, the suppression factor tables will be incorporated into the EPOCH code.

Thereafter, we will explore how we refined the derived data from the bremsstrahlung tables and how these modifications were incorporated into the PIC loop. Finally, we will present the modifications made to the electron deflection angle, the statistical evaluation of the photon spectral energy distribution, and the correction of optical depth for a photon.

6.1 Implementing Bremsstrahlung Suppression into EPOCH

Understanding the significance of the magnetic suppression (MS) and electric-magnetic suppression (EMS) models in the context of laser-plasma interactions necessitates their effective implementation within the plasma simulations. To do so, we implemented the established suppression models in Chapter [5] into the bremsstrahlung module of the EPOCH code. This section explains the modifications made to the EPOCH code, particularly focusing on the bremsstrahlung module, to accommodate these suppression models.

6.1.1 Suppression Factors for Tabular Data

As discussed in subsection (3.4.1), the bremsstrahlung module of EPOCH employs predefined data, which includes electron and photon energies, cross-sections, and cumulative distribution functions for photons. This extensive data allows users to explore a wide range of potential interactions associated with the bremsstrahlung process, including the use of different materials as targets and the investigation of bremsstrahlung emission from various electron energies. This data is retrieved during the initial stage, specifically within the "`setup_tables_bremsstrahlung`" subroutine of the bremsstrahlung simulation algorithm, and aligns with the chosen target material. As such, this subroutine is an apt place to incorporate changes to the bremsstrahlung cross-sections and introduce the suppression requirements, as we have previously modeled.

In the first phase of our implementation, we added a new table that links suppression factors with ranges of electric and magnetic fields, photon energies, and electron energies to the existing data in the original bremsstrahlung module. The variables for photon and electron energies were extracted directly from the original bremsstrahlung tables in the EPOCH code. The range for the selected magnetic field was based on typical values in laser-driven magnetic fields, from a few Teslas to higher field strengths expected in scenarios involving relativistic-induced transparency regimes, which can reach several MT-level. In the EMS model, we simply multiplied the magnetic field values from the generated table by the speed of light (c), invoking the $E = cB$ relationship that illustrates the interaction between electric and magnetic fields in electromagnetism. It is crucial to note that the selection of the field range is entirely dependent on the simulation's objectives. For instance, considering MT-level magnetic field strength in a laser-solid interaction would be impractical, as such strength is not typically observed in these interactions.

Considering the implicit nature of the suppression factor (5.10), as derived in Subsection (5.1.2), a direct analytical solution is not possible, thus requiring a numerical solution. To that end, we first used the iterative Newton-Raphson numerical method† outside of EPOCH via Python script, to compute the suppression values for the specified parameters, including electron and photon energies, and magnetic fields. These calculated suppression factors were then implemented into the tables in the bremsstrahlung module. Note that we executed additional modifications, particularly concerning data packaging and broadcasting within the message passing interface (MPI) algorithms, to prevent potential errors that could occur from introducing new arrays into the code.

6.1.2 Expansion and Refinement of Bremsstrahlung Tables

After setting up the suppression values table, our next task was to modify the extracted data, specifically the cross-section and cumulative distribution function (CDF) values for photon emission, from the bremsstrahlung tables within EPOCH. This was achieved by adding code snippets into the "`setup_tables_bremsstrahlung`" subroutine. A common finite difference approximation was employed to estimate a derivative, facilitating the computation of the initial differential cross-sections. We then improved these initial cross-sections by multiplying them with the corresponding generated suppression functions, as specified in Equation (5.11). The magnetic suppression condition $\varepsilon_\gamma/\varepsilon_e < \gamma B_{\text{ext}}/B_{\text{cr}}$ for the MS model and $\varepsilon_\gamma/\varepsilon_e < \gamma\tilde{\mathscr{E}}_{\text{ext}}/E_{\text{cr}}$ for the EMS model were applied during this modification process.

Following this, we calculated the updated total cross-sections $\sigma_{\text{MS}}(\varepsilon_e, B_{\text{ext}})$ and $\sigma_{\text{EMS}}(\varepsilon_e, \tilde{\mathscr{E}}_{\text{ext}})$ for each ion species, now factoring in the field dependencies. This was accomplished by integrating the modified differential cross-sections over all photon energies using numerical techniques. The next step was to upgrade the original cumulative distribution functions $\text{CDF}(\varepsilon_e, \varepsilon_\gamma)$ which were defined as follows:

$$\text{CDF}(\varepsilon_e, \varepsilon_\gamma) = \frac{1}{\sigma}\int_{\varepsilon_{\gamma_{\text{cut}}}}^{\varepsilon_\gamma} \frac{d\sigma}{d\varepsilon_\gamma^*} d\varepsilon_\gamma^*$$

The modified CDFs now have new dependencies: $\text{CDF}(\varepsilon_e, \varepsilon_\gamma, \tilde{\mathscr{E}}_{\text{ext}})$ for the EMS model and $\text{CDF}(\varepsilon_e, \varepsilon_\gamma, B_{\text{ext}})$ for the MS model. The significance of these modifications in cross-sections and the CDF is that they are crucial for generating bremsstrahlung photons in the bremsstrahlung algorithm embedded in the PIC loop.

†The Newton-Raphson method is a reliable numerical technique for approximating the roots (or zeros) of a real-valued function with increasing precision. It takes advantage of the fact that a continuous and differentiable function can be approximated by a straight-line tangent.

Importantly, the integration of the generated suppression functions that depend on the prepared field tables has increased the dimensionality of these tables at this stage. The steps for implementing local electric and magnetic fields derived from the main PIC loop are detailed in the subsequent sections.

6.1.3 Suppression Models in the PIC Loop

As explained in Subsection (5.1.2), our primary focus should now shift towards identifying the macroscopic fields responsible for the electron's deflection before emission over the formation length during a simulation time-step. The EPOCH's original bremsstrahlung module is embedded within the PIC loop, enabling us to directly calculate the electron deflection angle based on the transverse component (compared to the electron velocity vector) of the Lorentz force, $\theta_{\text{pic}} = \Delta p_\perp / p$. This is assessed by the particle pusher (Buneman-Boris algorithm) within the PIC loop for each simulation time-step Δt.

Subsequently, we call the computed deflection angle, θ_{pic}, before initiating the first Monte-Carlo algorithm to check bremsstrahlung emission probability within the "`initialise_optical_depth(current_species)`" subroutine. It is noteworthy that for photons with energies of $\varepsilon_\gamma = 10$ KeV and $\varepsilon_\gamma = 100$ KeV emitted by an electron with $\varepsilon_e = 100$ MeV, the formation time is typically 5 fs and 0.5 fs, respectively. These times reduce to 0.049 fs and 0.0045 fs for photons with $\varepsilon_\gamma = 1$ MeV and $\varepsilon_\gamma = 10$ MeV, respectively, emitted by the same radiating electron. These times must be compared with the typical temporal resolution of PIC, which in our simulation setup used in the ensuing chapter is about $\Delta t = 0.018$fs. Therefore, we need to rescale the deflection angle θ_{pic} according to the formation time of the bremsstrahlung to obtain the scaled deflection angle, $\theta_{\text{EMS}} = \theta_{\text{pic}} t_{f0} / \Delta t$ for example, which serves as the input for the relevant tables.

However, this introduces an additional layer of complexity to the Monte Carlo algorithm. The formation time, t_{f0}, is dependent on the energy of the emitted photon. The emitted photon energy is determined in the final step of the EPOCH bremsstrahlung Monte-Carlo algorithm, so it is not available at this stage for estimating t_{f_0}. To overcome this complexity, we incorporate an additional Monte Carlo step to evaluate a statistically significant photon spectral energy distribution. To avoid overstating the impact of low-energy photons, we initially constructed the marginal density function $\mathscr{P}(\varepsilon_e, \varepsilon_\gamma)$ by integrating $\tilde{\mathcal{E}}_{\text{ext}}$ out of $d\sigma_{\text{EMS}}/d\varepsilon_\gamma$, for instance in the EMS model. Then, we computed a new cumulative distribution function $\text{CDF}_{\text{marg.}}(\varepsilon_e, \varepsilon_\gamma)$, utilized to sample photon energy as required for determining

$\tilde{\mathscr{E}}_{\text{ext}}$ from the rescaled deflection angle θ_{EMS} such that,

$$\tilde{\mathscr{E}}_{\text{ext}} = \frac{m_e c\gamma}{|e|t_{f0}}\theta_{\text{EMS}}. \tag{6.1}$$

We now have local fields that are ready to be used in the next steps, which involve the interpolation technique.

6.1.4 Modifying the Optical Depth and Photon Emission Calculation

As previously mentioned in Subsection (3.4.1), the embedding of two Monte Carlo techniques within the temporal loop of the PIC simulation captures the inherent stochasticity of quantum emission. One such method pertains to the assessment of optical depth, which serves to ascertain the probability of an emission event.

In the original module, we evaluated the optical depth using first-order Eulerian integration, as shown in Equation (3.15). This integration process includes a total cross-section, $\sigma_t(\varepsilon_e)$ as part of the integration. It is important to note that this cross-section now relies on external fields. It is expressed either as $\sigma_{\text{MS}}(\varepsilon_e, B_{\text{ext}})$ for the MS model or $\sigma_{\text{EMS}}(\varepsilon_e, \tilde{\mathscr{E}}_{\text{ext}})$ for the EMS model.

To account for this modification, we have expanded the one-dimensional interpolation function routine used to determine the relevant cross-section into a two-dimensional interpolation function. Similarly, the second Monte Carlo technique has been refined. The original two-dimensional interpolation function that specified the photon energy has been enlarged to a three-dimensional function. This is a response to the cumulative distribution function's dependency now being shaped not just by the energies of the electron and photon but also by the state of the field.

As we incorporated suppression models into EPOCH, we enhanced the PIC loop with specialized code snippets. These additional pieces are integrated into the bremsstrahlung module, providing access to both the average pre-emission energy levels of the radiating electron and the average field strengths experienced by the same electron prior to emission.

These parameters are subsequently recorded as new photon properties, supplementing existing attributes for later data analysis. It is important to highlight that the inclusion of these new particle properties required the support of the MPI algorithm, which we've successfully implemented. Additionally, we have implemented control flags titled "`use_magnetic_suppression`" for using the MS model and "`use_electric_magnetic_suppression`" for the EMS model in the input deck, which are set to False by default. This feature offers an extra degree of control in our simulations, particularly by allowing the activation or deactivation of suppression mechanisms.

6.2 Summary

In this chapter, we have discussed integrating magnetic suppression (MS) and electric-magnetic suppression (EMS) models into the EPOCH code, specifically its bremsstrahlung module. The integration process involved creating a new table linking suppression factors with various electric and magnetic fields, photon energies, and electron energies. We refined the derived data from bremsstrahlung tables using a finite difference approximation to estimate initial differential cross-sections, which were extended by the inclusion of suppression factors. The resultant cumulative distribution function (CDF) now considers external field dependencies.

The suppression models were integrated into the PIC loop, requiring electron deflection angle rescaling and an additional Monte Carlo step for evaluating the marginal distribution of photon spectral energy. Extensive modifications were made to the optical depth evaluation and photon emission calculation due to cross-section dependencies on external fields. New code snippets were added to the PIC loop, granting access to electron energy levels and average pre-emission field strengths.

Chapter 7

Simulation Results

This chapter presents a detailed evaluation of the results from a series of 2D-PIC simulations that we conducted using the modified bremsstrahlung modules of EPOCH — the MS and EMS modules — in order to demonstrate the bremsstrahlung suppression effects in high-intensity laser-plasma interactions under the relativistic induced transparency regime. Simulations were conducted both with and without consideration of suppression effects; the original bremsstrahlung model in EPOCH and our modified suppression models MS and EMS were used. These models also serve as simulation tools for investigating potential systematic differences in electron acceleration mechanisms resulting from varying bremsstrahlung model parameter values.

Our method of analysis comprises two primary focuses. First, we discuss the macroscopic effects of the suppression of bremsstrahlung in laser-plasma interactions and their subsequent effects on the high-energy electrons in each simulation. The second topic focuses on the microscopic effects of suppression, specifically the phase-space density distribution of high-energy electrons and their emissions. By conducting this analysis, we hope to provide new insight into the complex connection between bremsstrahlung suppression and electron acceleration, as well as a detailed assessment of our developed suppression models and their significant roles in the laser-plasma interaction's scope. Our vision is that these findings will contribute to the ongoing refinement of models and theories in the field, which will ultimately lead to advances in the practical applications of laser-plasma interactions.

7.1 Simulation Setup

As shown in Figure (4.3), the study of the MS and EMS effects in high-power laser-plasma interactions requires the presence of both strong fields and energetic electrons. To achieve these conditions, it is essential to select the laser and target parameters with great care. The regime of relativistically induced transparency (RIT) in dense plasmas, as described in detail in Section (2.1.4), in conjunction with the use of a specific type of target, namely the structured micro-channel target, can effectively meet these requirements.

As evidenced in Subsections (2.2) and (2.4.1), previous research has demonstrated that the RIT regime manipulates laser-plasma interactions to generate ultra-relativistic electrons. This generation is facilitated by a direct laser acceleration mechanism that also maintains MT-level quasi-static magnetic fields within a structured target [17]. In light of these findings, we have chosen this particular interaction regime. In the subsequent section, we provide a more detailed description of the laser and target parameters utilized in our simulation experiments.

7.1.1 Laser and Target Parameters

Our primary objective was to examine the interaction between a laser pulse of the Petawatt class and a microstructured, overdense plasma target. To do so, we utilized a laser pulse with a Gaussian profile and the diameter of the focal spot (FWHM of the intensity) $w_0 \approx 2.2\ \mu m$ in the absence of the target. The corresponding peak intensity is $I_L = 5 \times 10^{22}$ W/cm^2, with a wavelength of $\lambda_L = 800$ nm, a normalized laser amplitude of $a_0 \approx 150$, and a pulse duration of $\tau_L = 30$ fs.

The simulation domain is defined by the length and width of the computational cells, which are set to 2250 cells along the x-axis and 800 cells along the y-axis. The length of the simulation domain extends from -15 μm to 30 μm, while the width spans from -8 μm to 8 μm. The target used in the simulations has a length of 30 μm and a channel radius of $R_{ch} \approx 0.8 w_0 = 1.8\ \mu$m.

As depicted in Figure (7.1), the initial configuration of our simulation includes a 2D microstructured, overdense plasma target. The plasma target is initially comprised of a channel with fully ionized uniform carbon plasma with an electron density of $n_e = 20 n_{\mathrm{cr}}$. In practice, this kind of density corresponds to foam and plastic targets [27]. This channel is surrounded by a relativistically near-critical bulk with a density of electrons equal to $100 n_{\mathrm{cr}}$. The coordinate system is defined so that $y = 0$ corresponds to the channel's longitudinal axis.

Despite the electron density in the channel exceeding the classical critical density,

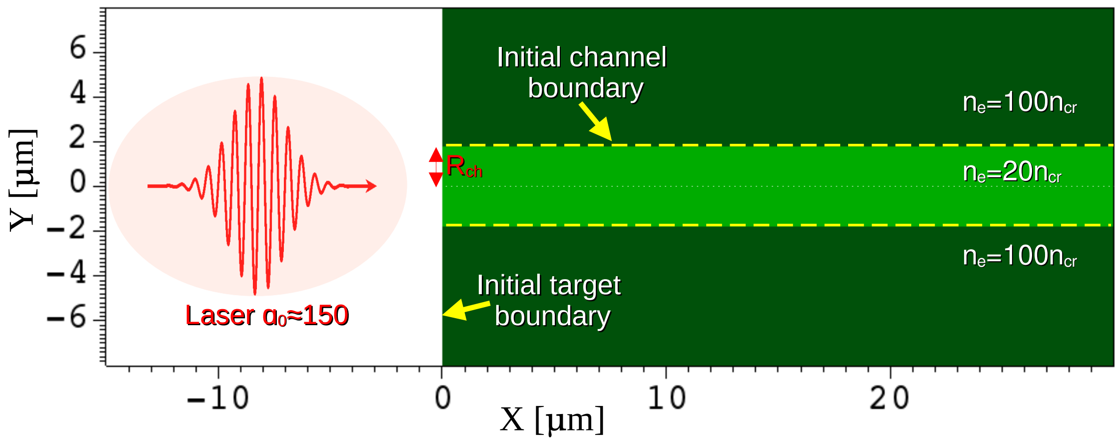

Figure 7.1: A schematic of the simulation setup where a high-intensity laser pulse $a_0 \approx 150$ is hit the entrance of a relativistically transparent channel with a radius of $R_{ch} = 1.8$ μm and $n_e = 20n_{\text{cr}}$ surrounded by a relativistically over-critical bulk $n_e = 100n_{\text{cr}}$. The boundaries of the channel and the target surface have been highlighted.

the considered high-intensity laser pulse in our simulation can propagate through the target due to the RIT regime, resulting in $n_e \ll a_0 n_{\text{cr}}$. Although materials such as aluminum or gold offer better statistics for bremsstrahlung, we chose a slightly lower Z carbon target for our simulation setup to ensure manufacturing applicability.

The implementation of a structured target with a channel offers two significant advantages. Firstly, a filled channel functions as an optical waveguide for the intense laser pulse, facilitating and stabilizing its propagation. This contrasts sharply with the use of a relativistically transparent target without a channel, where the same intensity laser pulse penetrates the plasma to create a channel but finally deviates from its axis due to hosing instability [27, 173]. The second advantage of the structured target is that the channel remains filled with dense plasma, enabling effective long-term volumetric interaction between the laser and the dense plasma, as explained in Subsection (2.4.1).

Previous studies have also demonstrated the effectiveness of similar configurations in enhancing high-energy radiation. For example, Stark et al. [27] achieved highly collimated multi-MeV photon beams by employing a combination of quasistatic magnetic fields (0.4 MT), relativistic transparency, and the DLA mechanism. In their research, they provided evidence that an MT-level quasistatic magnetic field, produced by collective effects in the RIT regime, supports the sustained acceleration of electrons. This acceleration, in turn, increases the synchrotron emission rate, resulting in a Petawatt class laser system that generates tens of TW of directed MeV photons. Wang et al. [172] investigated the conversion efficiency of laser energy to gamma-rays within the RIT regime using structured laser-irradiated targets with prefilled cylindrical channels, similar to our simulation setup. Their research revealed that the boosted electron acceleration made possible by the laser pulse and the quasistatic magnetic field improved conversion efficiency. Our chosen target configuration, therefore, has the potential to help us achieve our research objectives.

To improve the interaction between the laser and plasma channel, the focal point of the laser beam was deliberately made larger than the plasma channel's width. This condition enables the longitudinal component of the laser's electric field to continue to exist over a distance (over tens of microns) significantly greater than the Rayleigh length, $z_R = \pi w_0^2/\lambda$, which is the distance at which the beam's intensity is dropped to approximately $\frac{1}{2}(1/e^2)$ of its peak value, I_L [26].

Figure 7.2(a) illustrates the normalized azimuthal magnetic field $|\langle B_z \rangle|/B_0$ in the xy-plane at $z = 0$, generated by the longitudinal electron current within the channel. Figure 7.2(b) displays the profile of the normalized transverse quasi-static electric field $|\langle E_\perp \rangle|/E_0$, which is generated by the laser beam and averaged over one laser period. Here, E_0 and B_0 represent the maximum amplitudes of the laser field for the utilized laser intensity I_L, with approximate values of $E_0 \approx 6.13 \times 10^{14}$ V/m and $B_0 \approx 2.04$ MT, respectively. For a detailed list of parameters employed in our two-dimensional simulations, please refer to Table (7.1).

It is important to highlight that the dominant radiation mechanism in the considered regime is synchrotron radaiation [27]. Wan et al. [251] demonstrated that this emission becomes the dominant process at laser intensities $I_L \geq 10^{21}$ W/cm^2 (for 1 μm-thick Al) and $I_L \geq 10^{22}$ W/cm^2 (for 1 μm-thick Au) targets. However, recent research conducted by Martinez et al. [157] has found a regime where the roles of bremsstrahlung and synchrotron emission are reversed, leading to bremsstrahlung-dominated radiation mechanisms. Using simulations with a fixed set of laser parameters ($I_L = 10^{22}$ W/cm^2) and a solid-density copper plasma slab with a thickness of 16 nm $\leq l \leq 5$ μm, they investigated the impact of target thickness on laser-plasma interactions. By comparing synchrotron and bremsstrahlung emission, they discovered that the efficiency of bremsstrahlung gradually increases with thicker targets, scaling as $\eta \propto l^{1.5}$ in the thickness range considered, and begins to predominate synchrotron radiation at approximately ($l \approx 1-2 \mu m$). Even though the target used in this study does not provide a sufficiently strong magnetic field for investigating the magnetic suppression effect, this significant finding demonstrates the importance of studying bremsstrahlung emission in situations where synchrotron radiation has been assumed to be the predominant form of radiation.

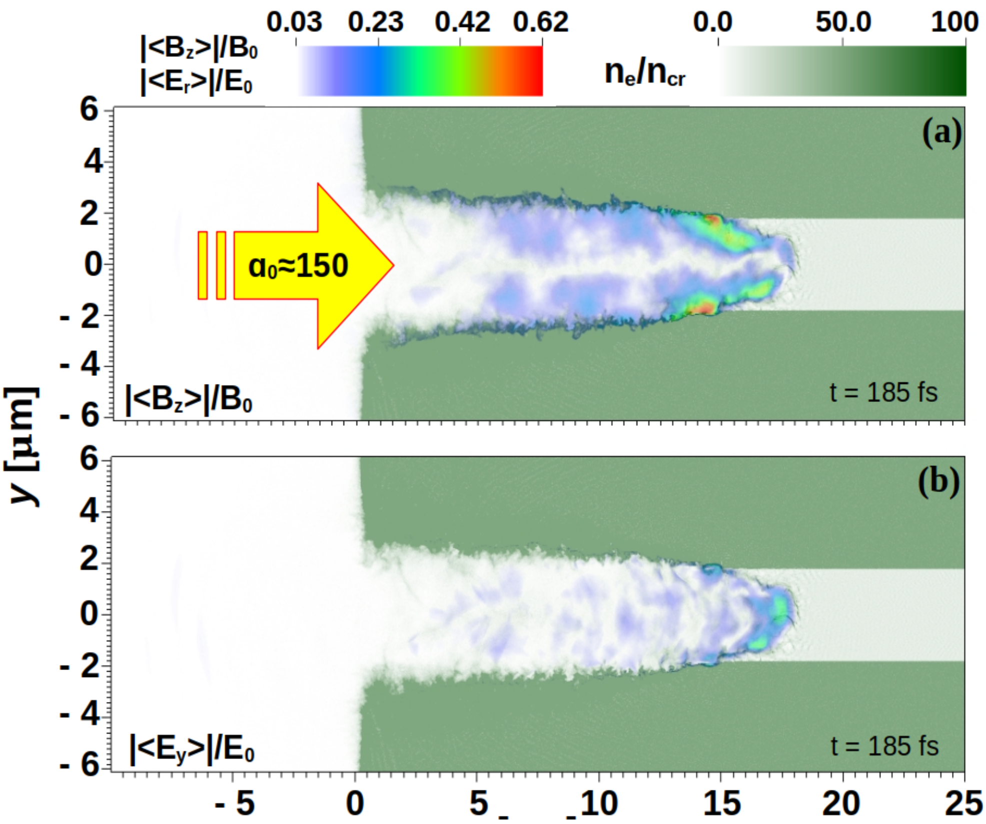

Figure 7.2: A snapshot of the simulation setup at 185 fs, illustrating a high-intensity laser pulse $I_L = 5 \times 10^{22}$ W/cm^2 ($a_0 \approx 150$) propagating through an initially uniform relativistically transparent narrow channel ($n_e = 20n_{\rm cr}$) surrounded by a relativistically over-critical bulk ($n_e = 100n_{\rm cr}$). The snapshot shows (a) the generation of a strong azimuthal magnetic field and (b) a radial electric field, both averaged over one laser period.

7.2 Analysis of Simulation Results

This section presents the analysis of results obtained from a series of 2D PIC simulations conducted to validate our implemented model in the EPOCH code and examine the impact of bremsstrahlung suppression on laser-plasma interactions. We compare the outcomes of simulations performed with and without the suppression effects, utilizing different scenarios: simulations without any suppression, conducted using the original bremsstrahlung module of the EPOCH code (referred to as EPOCH); simulations with electric and magnetic suppression, performed using our modified bremsstrahlung module in EPOCH (referred to as EMS); and simulations with only magnetic suppression, carried out with our modified bremsstrahlung module in EPOCH (referred to as MS).

To facilitate the discussion and provide a comprehensive analysis, we categorize the examination of simulation results into two subsections, focusing on the

Table 7.1: Parameters of 2D PIC simulations.

Parameters	**Values**
General parameters:	
Computational cells ($n_x \times n_y$)	2250 $\times$ 800
Length of simulation domain	(-15,30) μm
Width of simulation domain	(-8,8) μm
Spatial resolution	$50/\mu m \times 50/\mu m$
Laser parameters:	
Peak intensity	$5 \times 10^{22} W/cm^2$
Wavelength	800 nm
Pulse duration (FWHM of intensity)	30 fs
Focal spot size	2.2 μm
Location of focal plane	$x = 0$ μm
Target parameters:	
Target length (x)	30 μm
Target width (y)	16 μm
Channel radius	R_{ch}=1.8 μm
Composition	C^{+6} and electrons
Channel density (n_e)	20 n_{cr}
Bulk density (n_e)	100 n_{cr}

macroscopic and microscopic aspects of the suppression effects on bremsstrahlung emission. This categorization allows us to investigate the overall dynamics of the system from a macroscopic perspective while delving into the microscopic details of the underlying processes.

7.2.1 Macroscopic Impact of the Suppression Effects

In this subsection, we examine the high field suppression of bremsstrahlung as well as assess the macroscopic impact of these suppression effects on laser-plasma interactions. By comparing the simulation results from EPOCH, EMS, and MS scenarios, we analyze the global behavior of the system, considering parameters such as the total emitted bremsstrahlung energy, the distribution and propagation of high-energy electrons, and the spatiotemporal evolution of radiation emission. This analysis enables us to understand how the presence of electric and magnetic fields influences the overall dynamics and characteristics of bremsstrahlung emission.

Through the macroscopic examination, we evaluate the effectiveness of the suppression mechanisms in modulating bremsstrahlung emission and altering its macroscopic properties in high-intensity laser-plasma interactions. By identifying and comparing the trends observed in different simulation scenarios, we gain insights into the collective behavior and general trends exhibited in the interaction between the laser pulse and the plasma target.

- **Photon Spectra**:

The primary aspect of our first analysis is to investigate the energy emitted in the form of bremsstrahlung radiation within a defined channel[†] of the target. This particular section was chosen due to the presence of the strong azimuthal magnetic field that results from the high-intensity interaction between laser and plasma within this domain. Our study aims to quantify the total energy of the bremsstrahlung radiation generated as a consequence of the interaction between high-energy electrons and the plasma target.

In our approach, we ignored the recoil energy, that is, the energy lost when an electron emits photons, in both simulations with and without the bremsstrahlung suppression effect to maintain comparable electron distributions across these simulation runs. As the emission probability of a radiating electron is determined by its entire optical depth history [36], the emission characteristics are determined not only by the electron's immediate surrounding properties but by the full history of emissions. Consequently, we compute the average electron energy $\langle \varepsilon_e \rangle$, and the average electric $\langle \tilde{\mathcal{E}} \rangle$ and magnetic $\langle B_z \rangle$ field strengths encountered by radiating parent electrons prior to emission, between each emission event in the bremsstrahlung module of EPOCH. These values are stored as new particle properties, along with other photon characteristics, to facilitate subsequent analysis of the emitted photons.

We specifically focus on the bremsstrahlung photon emissions from a certain group of high-energy accelerated electrons within the target. These selected electrons show averaged energies between 95 MeV and 105 MeV from one emission event to the next. Additionally, we have constrained our selection to only those electrons that have been exposed to a range of magnetic fields with average values from 0.29 to 0.31 for normalized magnetic fields, denoted as $|\langle B_z \rangle|/B_0$. We have made this specific choice of electron energy and surrounding macroscopic magnetic field to examine our models under the regime of relativistically induced transparency, as depicted in Figure (4.3).

[†] The term "channel" refers to a selected section of the target designed to create an effective interaction area between the laser and plasma. This section spans from the channel's entrance ($x = 0$) to $x = 19$ μm and covers the same width as the channel's radius, i.e., from $y = -1.8$ μm to $y = 1.8$ μm.

Figure 7.3(a) compares the energy distribution of bremsstrahlung for the MS and EPOCH models. As the photon energy increases, the flux of emitted photons steadily decreases, eventually reaching zero at the bremsstrahlung endpoint, around ε_e. Clearly, when considering the suppression of bremsstrahlung photons due to a strong magnetic field, a marked difference in the count of low-energy photons (with energies below 2.7 MeV) is observed in the MS model compared to the reference runs (EPOCH). This divergence amplifies as photon energies decrease.

On the other hand, Figure 7.3(b) exhibits the cumulative count of photons with $\varepsilon_\gamma^* < \varepsilon_\gamma$ as a function of ε_γ, defined by the following equation:

$$N_\gamma(\varepsilon_\gamma^* \leq \varepsilon_\gamma) \equiv \int_{\varepsilon_{\gamma_{cut}}}^{\varepsilon_\gamma} \left(\frac{dN_\gamma}{d\varepsilon_\gamma^*}\right) d\varepsilon_\gamma^* \ . \tag{7.1}$$

While the MS simulations primarily result in a decrease in photon yield for low-energy photons, the overall spectral shapes of bremsstrahlung are exponentially inverted, resulting in a significant decrease in the total number of photons emitted. Specifically, for the subsets we examined, the reduction was $\Delta N_\gamma = 36.25\%$ for the MS model.

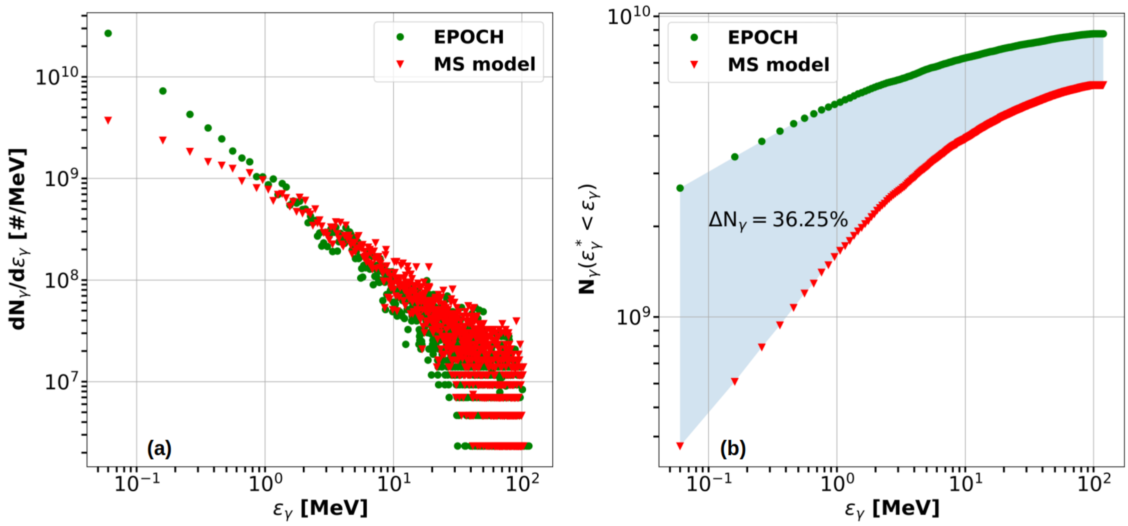

Figure 7.3: Comparative analysis of (a) the energy distribution of bremsstrahlung, and (b) their corresponding accumulated number of photons with $\varepsilon_\gamma^* < \varepsilon_\gamma$, defined by Equation (7.1), as a function of ε_γ, for the MS model. The analysis was conducted for a subset of radiating electrons with an averaged energy of between 95 MeV and 105 MeV that passed through regions with normalized fields of $0.29 - 0.31$.

In our analysis of the PIC simulation results for the EMS model, we executed further simulations using identical configurations to the previous ones. This time, however, we limited the PIC output results to a specific subset of electrons, specifically those that experienced normalized fields with average values ranging from

$0.29 - 0.31$ for $|\langle\tilde{\mathcal{E}}\rangle|/E_0$. Subsequently, we compared the simulated energy distribution of bremsstrahlung for the EMS model with the EPOCH results, as illustrated in Figure 7.4(a). The observed suppression behavior in the EMS model was almost similar to that in the MS model but with a slightly higher reduction.

Additionally, we noted a distinct deviation in the number of low-energy photons with energies below 3 MeV in the EMS model. This deviation occurred when the suppression of bremsstrahlung photons due to strong macroscopic electric and magnetic fields was included, in contrast to the reference runs (EPOCH). Our analysis further uncovered that the decrease in the number of photons denoted as ΔN_γ, amounted to 50.44%, as depicted in Figure 7.4(b).

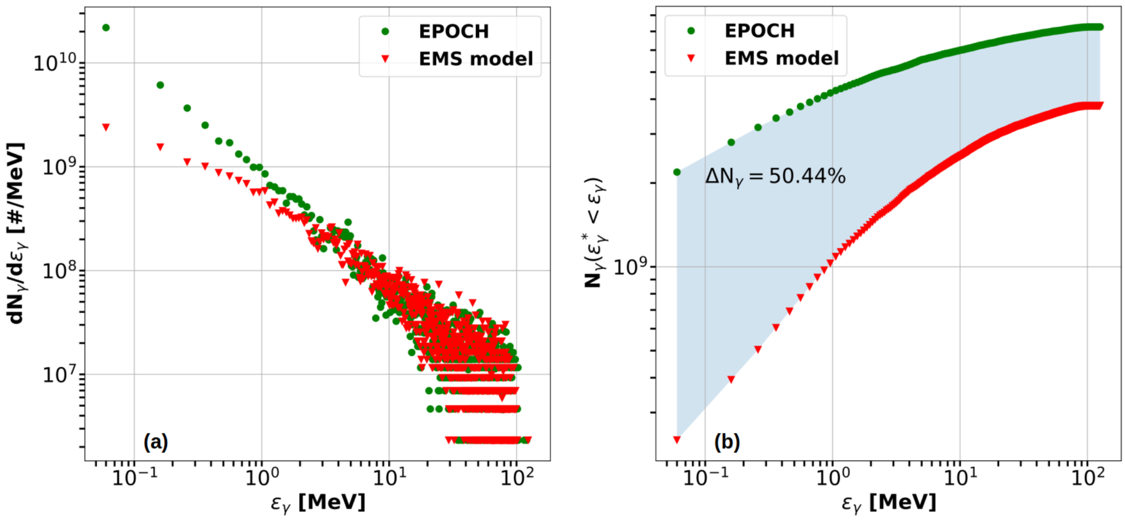

Figure 7.4: Comparison of (a) the energy distribution of bremsstrahlung, and (b) their corresponding accumulated number of photons for the EMS model. The analysis focused on a subset of radiating electrons with average energies ranging between 95 MeV and 105 MeV that traversed through regions with normalized fields of $0.29 - 0.31$.

In the subsequent phase, our focus shifted towards acknowledging the significance of macroscopic strong magnetic and electric fields in bremsstrahlung emission. To achieve this, we deliberately disregarded any limitations posed by the average field strength and proceeded to reanalyze the photons produced by high-energy electrons with average energies ranging from 95 MeV and 105 MeV. Remarkably, even under these revised conditions, we still observed a substantial reduction in bremsstrahlung. Specifically, the MS model exhibited a noteworthy suppression of $\Delta N_\gamma = 37.10\%$, while the EMS model experienced a comparable decrease of $\Delta N_\gamma = 35.65\%$. This observation demonstrates the significant effect that electric and magnetic fields have on the suppression of bremsstrahlung, even when the entire range of magnetic fields generated within the channel, including those that are not exceptionally strong, is considered. In other words, they confirmed the role of cumulative relatively weaker environmental factors, in this instance, macroscopic fields, in bremsstrahlung suppression [33]. In addition, the results highlighted the interdependence of the suppression function, electron energy, and macroscale fields.

To ensure the integrity of our findings and eliminate any potential bias resulting from prior assumptions or analysis restrictions, we conducted additional simulations. These simulations were designed to evaluate the robustness of the observed suppression effects across various scenarios, including accounting for the recoil of photon emission on the parent electron. In essence, we took into account the fact that when a charged particle emits a photon, it experiences a recoil force that can influence its subsequent behavior.

Furthermore, our analysis encompassed all emissions occurring within the initial density channel of $20n_{\mathrm{cr}}$, independent of the energies of the emitting electrons. This approach allowed us to capture a broader range of emissions and obtain a more complete picture of the phenomenon under investigation. Overall, our findings revealed a significant suppression of low-energy emissions. When comparing the accumulated number of photons, we observed a reduction of $\Delta N_\gamma = 17.43\%$ for the MS effect and $\Delta N_\gamma = 19.11\%$ for the EMS effect, compared to $\Delta N_\gamma = 18.35\%$ and $\Delta N_\gamma = 20.77\%$ when the recoil was disregarded.

We extended our investigation to assess the suppressive effects of bremsstrahlung in a different scenario: a bulk foam target lacking a channel with an initial electron density of $n_e = 20n_{\mathrm{cr}}$. In this particular study, our analysis encompassed all electrons and emissions throughout the entire simulation box, ensuring the inclusion of every electron and photon generated within the system. The objective of this study was to examine the impact of the EMS and MS models on the overall count of emitted photons, eliminating the complicating influence of a channel. Notably, our findings revealed a comprehensive reduction in the total number of photons, amounting to $\Delta N_\gamma = 15.27\%$ for the EMS model and $\Delta N_\gamma = 14.14\%$ for the MS model.

The process of benchmarking played a crucial role in our study by validating the accuracy of our simulation model and its ability to capture the underlying physics. In order to achieve this, we compared the simulation results with theoretical predictions, aiming to provide confidence in the reliability of our findings.

We quantified the extent of suppression in the PIC simulations by analyzing the ratio of the spectral density of generated photons, calculated from histograms, both with and without the inclusion of suppression effects. These measurements are

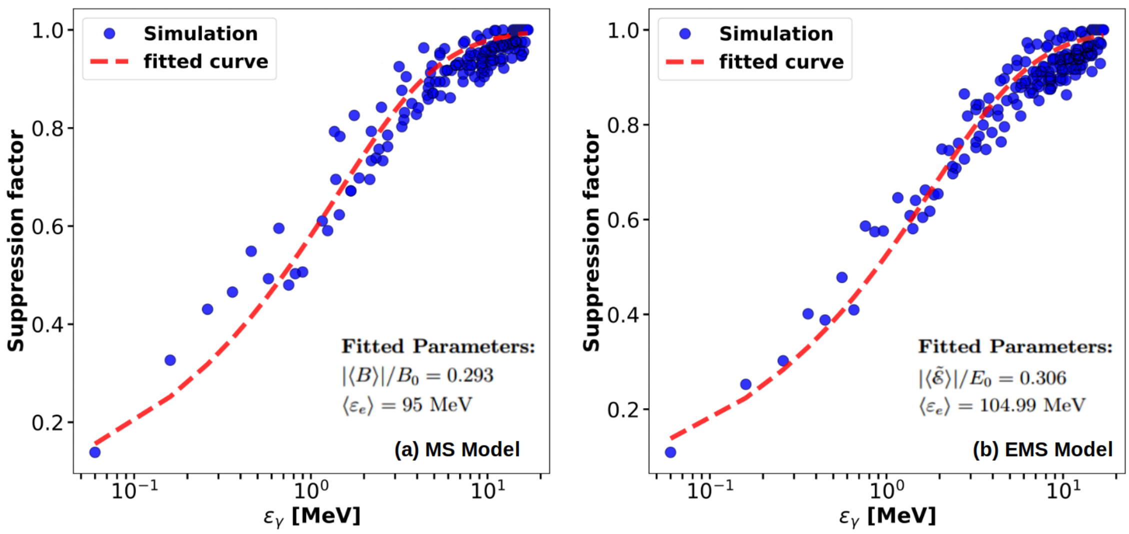

Figure 7.5: Panels (a) and (b) show curve-fitting (red dashed curve) of PIC-simulation data (filled blue circles) for the suppression factors obtained from two suppression models, MS and EMS, respectively.

depicted by the filled blue circles in Figures 7.5(a) and (b). By fitting these data points, obtained from simulations that accounted for specific electron energy and field subsets, with the analytical function defined by equation (5.8), we were able to determine the suppression factor. Employing analytical functions and optimization techniques to fit simulation data provides a robust method of quantifying the impact of suppression effects on bremsstrahlung radiation. In this process, we treated photon energy as the independent variable for the suppression function while simultaneously determining optimal values for the average electron energy and macroscopic fields. It is worth noting that the optimized values for the parameters used in the curve-fitting process have successfully recovered the previously defined subsets utilized to constrain the photon analysis. This outcome signifies the accuracy of our methodology.

- **Spatio-Temporal Evolution of Bremsstrahlung Emission**:

In this analysis, we examined how the distribution and intensity of radiation produced by our simulation experiments vary across different locations within the channel and as time progresses. To this end, we studied the evolution of low-energy bremsstrahlung emissions (less than 10 MeV) produced by high-energy electrons (with energies exceeding 95 MeV) when they interact with the plasma channel. These electrons emit bremsstrahlung emissions along their respective trajectories through the channel, with an observed peak at 185 fs.

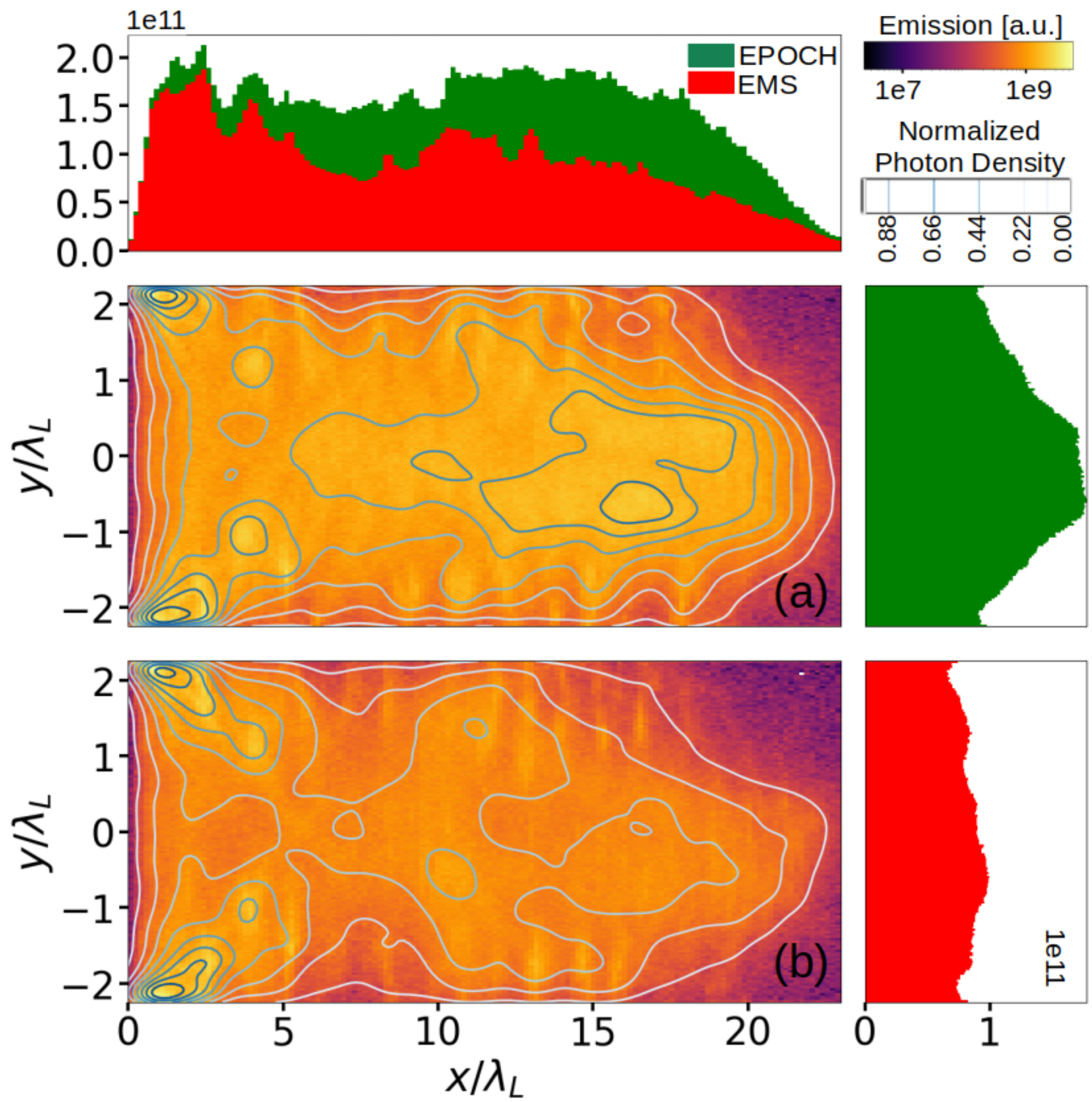

Figure 7.6: The colored map of the density of emissions below 10 MeV emitted by the electrons with energy greater than 95 MeV integrated until t = 185 fs for simulations from (a) EPOCH and (b) the EMS model. The overlaid contour lines represent regions of equal photon density, providing a clear visualization of the spatial distribution of the photon density within the plasma channel. Marginal histograms of vertical and horizontal photon distribution are included, revealing variations in density across models.

Figure (7.6) visualizes the cumulative photon counts per cell, integrated up to a time of 185 fs. We utilized heat mapping to enhance the comparative analysis between the EPOCH and EMS models. Remarkably, the model incorporating the suppression effect—Figure 7.6(b)—appears to manifest less concentrated low-energy emissions within the channel as opposed to the model devoid of suppression, EPOCH—Figure 7.6(a).

To support this observation, we used contour lines to depict constant levels of normalized photon density within the plasma channel, with each line representing a unique density level†. According to the contour plots, the EPOCH model exhibits denser lines, thereby implying a greater concentration and density of photons. In contrast, the EMS model shows a more dispersed and suppressed distribution of photons. This finding is corroborated by the marginal histograms of the vertical and horizontal distributions of the bremsstrahlung photons, which exhibit a significant reduction of photons in the EMS model compared to the EPOCH model. This evidence significantly advances our understanding of suppression mechanisms at a macroscopic level and could provide valuable insights for subsequent microscopic-level inquiries.

Momentum Distribution of Electrons:

In the scope of our macroscopic analysis, another critical aspect to examine is the dynamics of electrons emitting radiation, with a specific focus on understanding the effects of bremsstrahlung suppression on the emitting electrons. This investigation centers on analyzing the spatial and temporal distributions of high-energy electrons during the bremsstrahlung process. We examined how these high-energy electrons are distributed within phase space, while their energy loss through the bremsstrahlung process is modified by the implementation of a suppression mechanism.

To better illustration of this effect, we presented a heat-map plot representing the momentum distribution of all electrons at a specified moment and comparing it between the EPOCH and EMS models. In particular, Figures 7.7(a) and (b) exhibit the momentum distribution (p_x, p_y) at 185 fs. From a macroscopic perspective, noticeable differences in the phase-space density distribution (particularly the highlighted areas) point to variations in the electron acceleration dynamics along both the x and y directions. Nevertheless, a detailed examination at the microscopic scale might be imperative to show the inherent patterns embedded within these variations.

7.2.2 Microscopic Impact of the Suppression Effects

In this subsection, we explore the microscopic impact of bremsstrahlung suppression effects on laser-plasma interactions. Here, we focus on the detailed processes and mechanisms underlying the suppression of bremsstrahlung emission at the in-

†Remember that the term 'density' in this context refers to the distribution of the data points, not physical density.

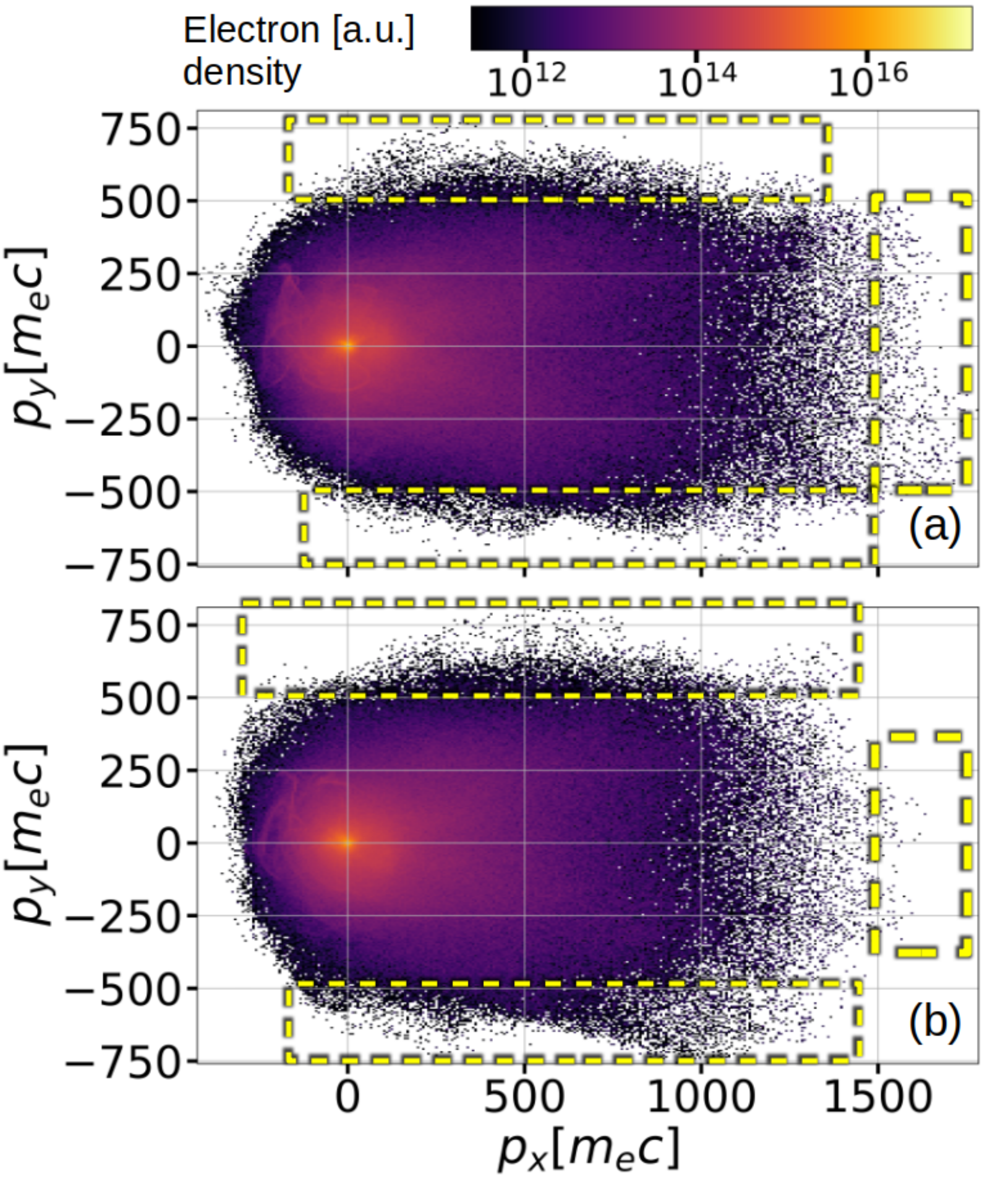

Figure 7.7: A snapshot of the phase space of all electrons for (a) EPOCH and (b) the EMS model at t = 185 fs. The Highlighted yellow areas aim to compare the maximum momenta in both X and Y directions between two models.

dividual particle level. By analyzing the characteristics and dynamics of individual electrons and the influence of suppression mechanisms on electron acceleration, we gain a deeper understanding of the microscopic phenomena driving the suppression of bremsstrahlung emission.

To accomplish this, we initiate our analysis by studying the temporal behavior of a select few high-energy electrons. This involves tracking the trajectories of these electrons and observing their movements within the plasma target, paying special attention to the locations where bremsstrahlung emission occurs.

To further investigate the effects of each field component on the suppression of bremsstrahlung, we trace the electric and azimuthal magnetic fields exerting influence on three sampled high-energy electrons throughout their trajectories. This tracing process enables us to perform a more detailed examination of how each field component impacts the overall process of bremsstrahlung suppression. Through this analysis of the microscopic dynamics of emitting electrons, we aim to answer a critical question: Does the reduction of bremsstrahlung-associated energy losses prove advantageous for electron acceleration within the given experimental setup? Let us now begin our exploration by examining the dynamics of high-energy electrons and their bremsstrahlung emissions.

- **Tracking high-energy electrons and their bremsstrahlung emissions:**

In order to delve deeper into the microscopic level of the suppression effect, we conducted an analysis of the trajectories followed by highly energetic electrons that were accelerated within the channel. In this study, we examined the behavior of these electrons by tracking their paths in reverse until we reached the origin of their acceleration. We used the EPOCH particle-tracking diagnostic tool to accomplish this, which allowed us to keep track of and gather information on the positions, velocities, and energies of specific electrons at various time intervals.

For this investigation, we randomly selected eight electrons with energy levels exceeding 500 MeV at $t = 185$ fs, employing both the EPOCH and EMS models. The resulting trajectories of these electrons are depicted in Figures 7.8(a) and 7.8(b), represented by distinct black and color-coded lines. It is worth noting that three trajectories were carefully chosen and highlighted using color-coded lines to facilitate a closer examination of their interaction with the macroscopic fields encountered along their paths (as discussed further in the subsequent subsection). Our analysis revealed that, in both cases, the sampled electrons originate from the peripheral region of the channel near its entrance. They are subsequently accelerated in the forward direction by the intense laser pulse. Additionally, we observed a phenomenon consistent with Gong's findings [17], namely that these trajectories remain confined within a magnetic boundary denoted as $R_{MB}(\approx 1\ \mu m)$. This magnetic boundary is noticeably smaller than the initial radius of the channel, $R_{ch} = 1.8\ \mu m$.

Furthermore, our findings revealed a noticeable disparity between emission events in the two simulations: the trajectory paths in the simulation incorporating suppression effects (Figure 7.8(b)) exhibited fewer emission vertices compared to the simulation without suppression effects (Figure 7.8(a)). This observation strongly suggests that the presence of macroscopic fields indeed leads to a reduction in bremsstrahlung radiation. Overall, our study of energetic electron trajectories and

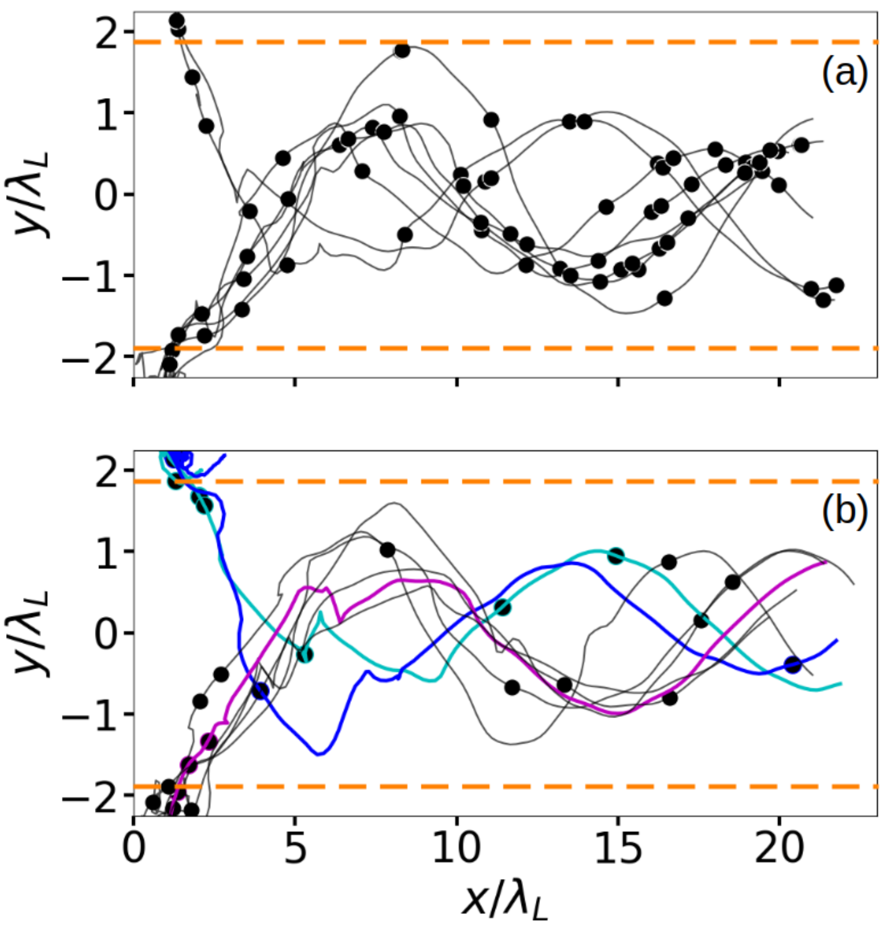

Figure 7.8: Tracking the trajectory of eight electrons emitting at energy levels above 500 MeV, represented by black and color-coded lines, and indicating their bremsstrahlung vertices with filled-black circles as they move within the channel. This display is integrated until $t = 185$ fs and represents simulations from (a) EPOCH and (b) the EMS model. The orange dashed lines represent the channel's walls.

associated bremsstrahlung emissions gives information on the complicated interplay of electric and magnetic fields, as well as the impact of suppression effects on electron acceleration and bremsstrahlung radiation.

Tracing electric and magnetic fields:

We conducted a comparative study of suppression levels in the MS and EMS models, as detailed in the preceding section and throughout our photon spectra analysis. As these models could be influenced by the strengths of macroscopic fields, we traced the electric and magnetic fields acting on the color-highlighted electrons shown in Figure 7.8(b) as they navigated through the plasma. This investigation examined the temporal history of the normalized transverse electric ($E_\perp/E_0$) and magnetic ($V_\parallel B_z/E_0$) components of the Lorentz force, as well as their differences.

These components reveal the force acting on the electrons along their trajectory, shedding light on the deflection angle significant to the bremsstrahlung suppression mechanism.

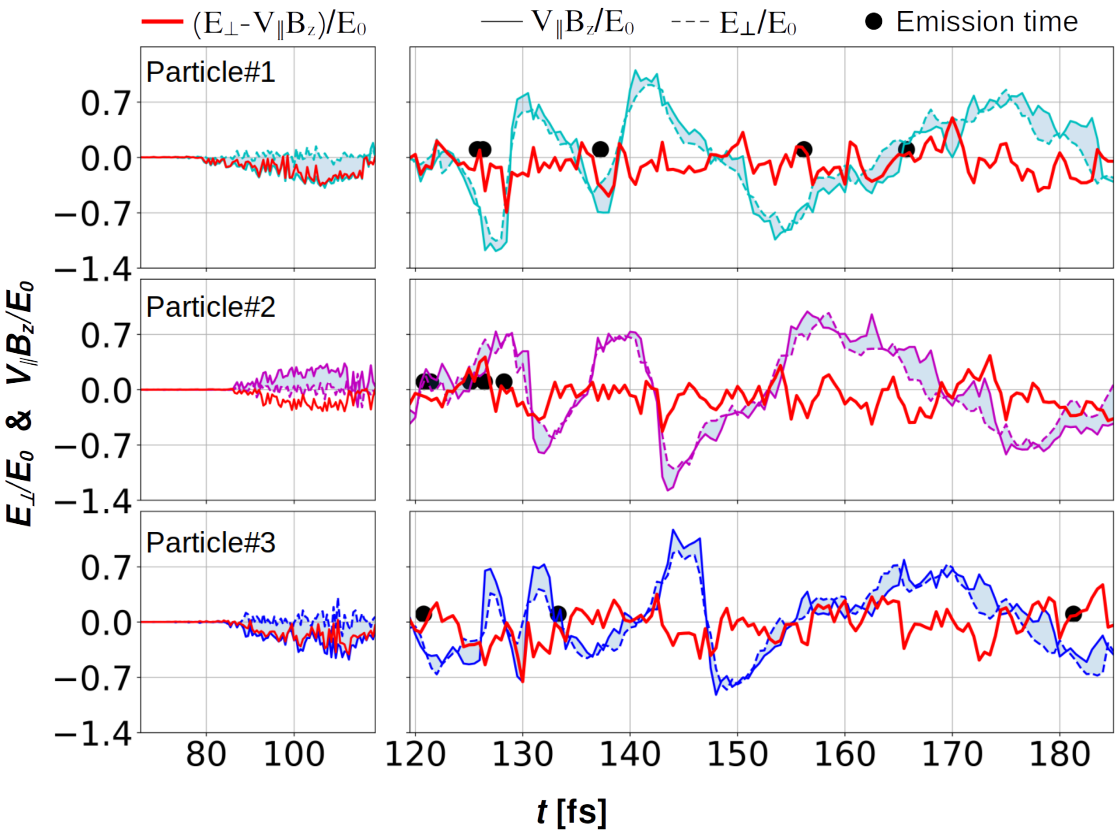

Figure 7.9: Comparing normalized transverse components of the Lorentz force (with respect to the electron trajectory), $E_{\perp}/E_0$ and $V_{\parallel}B_z/E_0$, acting on the three highlighted electrons in Figure 7.8(b).

The tracing analysis illustrated two distinct types of interactions between the electrons and the electric and magnetic fields. Until about $t \approx 120$ fs, the electrons were subjected to acceleration from fields at the channel entrance, where the magnetic and electric field components exhibited substantial imbalance. However, once the electrons entered the channel, they encountered acceleration from the electric and magnetic fields. Notably, the transverse Lorentz force component from the plane wave showed substantial compensation between the electric and magnetic field components for all electron trajectories, as shown in Figure(7.9).

Despite the EMS model averaging a lower field strength than the MS model, the bremsstrahlung photon yield remains comparable between the two. This may initially seem counterintuitive, but can be explained by the slow scaling of the suppression factor (see Figure (4.3)). For the electron energy and field strength ranges occurring in the relativistically induced transparency regime, the expected differ-

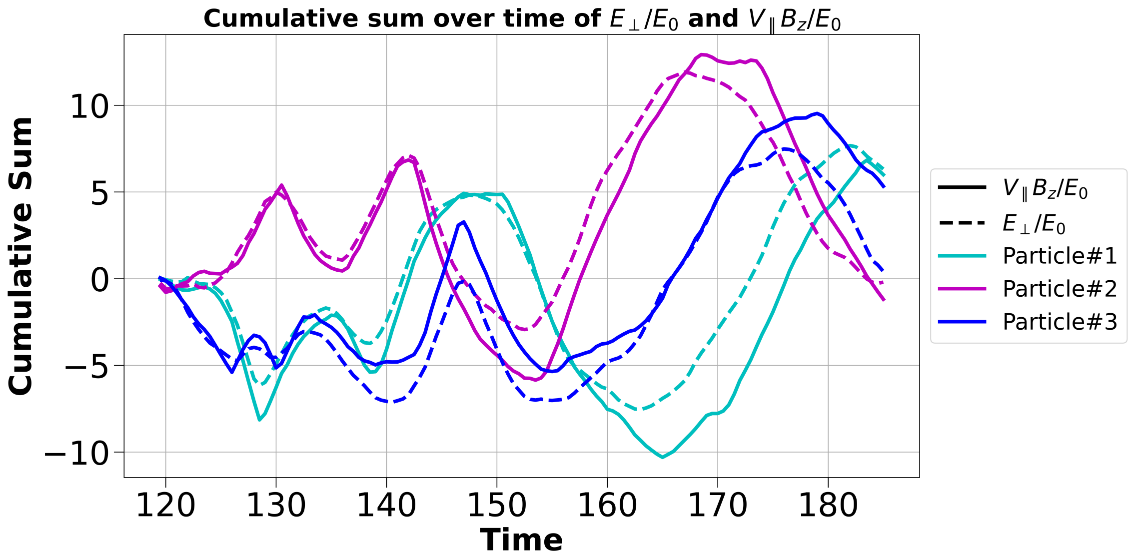

Figure 7.10: Cumulative summation over time of transverse electric field $E_{\perp}/E_0$ and magnetic field $V_{\parallel}B_z/E_0$ components for three high-energy electron trajectories. The figure illustrates the dynamic interplay between these fields and the particles, highlighting the alternating dominance of each field on particle trajectories and the resulting high-field suppression effects.

ences in bremsstrahlung yield between the two models are negligible. Thus, a similar overall bremsstrahlung yield is expected for both models.

To further understand these interactions, we examined the cumulative sum of the transverse electric and magnetic field components for each particle over time, as shown in Figure (7.10). This analysis provides an accumulative perspective of these fields' influence on the particles' trajectories, underscoring the dynamic and complex nature of electron dynamics in electromagnetic fields. The alternating dominance observed in the plot indicates a temporal fluctuation in the effects of transverse electric and magnetic field components on the electrons. During certain intervals, the cumulative effect of the transverse electric field component appears dominant (i.e., $E_{\perp} > V_{\parallel}B_z$), potentially causing a more pronounced alteration in the particles' trajectories. Conversely, there are periods when the cumulative sum of the transverse magnetic field component becomes dominant, suggesting a stronger cumulative influence from the magnetic field.

While this analysis was conducted for only three high-energy electron samples, the fluctuations and oscillations seen in the cumulative summation highlight the dynamic interplay between the particles and the transverse electric and magnetic fields. The lack of consistent dominance by either field highlights the complexity of this interaction and the consequent need for further detailed investigations. Nevertheless, from the current results, we infer that both fields considerably impact the particles over their trajectories, leading to high-field suppression effects.

- **Phase-Space Density Distribution of High-Energy Electrons:**

Our research has particularly focused on the behavior of high-energy electrons subject to the EMS model. The primary objective was to ascertain if there were systematic differences in the acceleration between the two EPOCH and the EMS models under investigation. To this end, we examined the phase-space distribution of electron momenta (x, p_x) and (x, p_y) at a specific moment in time—185 fs. This is illustrated in Figure (7.11), which includes a wide segment window encompassing the entire region from the entry point of the channel to the furthest penetration of the laser in the channel up to the simulation time.

The figure highlights the peaks of momentum in both x and y components with yellow-dashed lines. A notable observation was the difference in the phase location of these peaks between the two models. To examine these variances further, we zoomed into the Figure (7.11) using narrower segment windows and multiple time snapshots—145, 155, 165, 175, and 185 fs. This is represented in Figures (7.12-7.16).

Our analysis was primarily concentrated on the x segment windows located around the peak of laser intensity. This choice was predicated on the observation that the magnetic field generated by accelerated electrons essentially limits injections into the channel to its entrance.

The analyses performed indicated notable disparities in the electron dynamics between the two simulations, as can be seen from the yellow-dashed lines in Figure (7.11) and the smaller segments. One plausible explanation for these discrepancies could be variations in recoil energies employed by the EMS effect, which could subsequently alter the dephasing between the electron and accelerating fields. However, these discrepancies did not demonstrate any systematic pattern. This leads us to conclude that while bremsstrahlung suppression does not categorically enhance or degrade electron acceleration, it unquestionably influences the specific characteristics of electron acceleration dynamics.

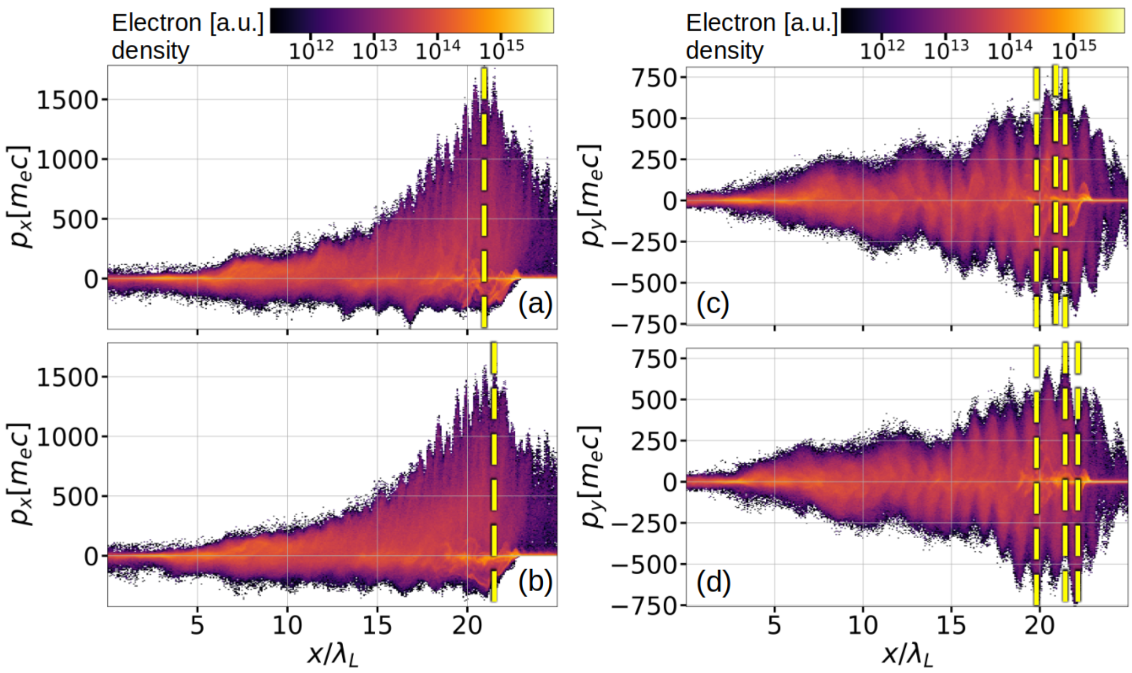

Figure 7.11: Phase-space density distribution of accelerated electrons with energy above 95 MeV at 185 fs using the EPOCH and EMS models. The maximal momenta are found at different positions, suggesting distinct acceleration histories.

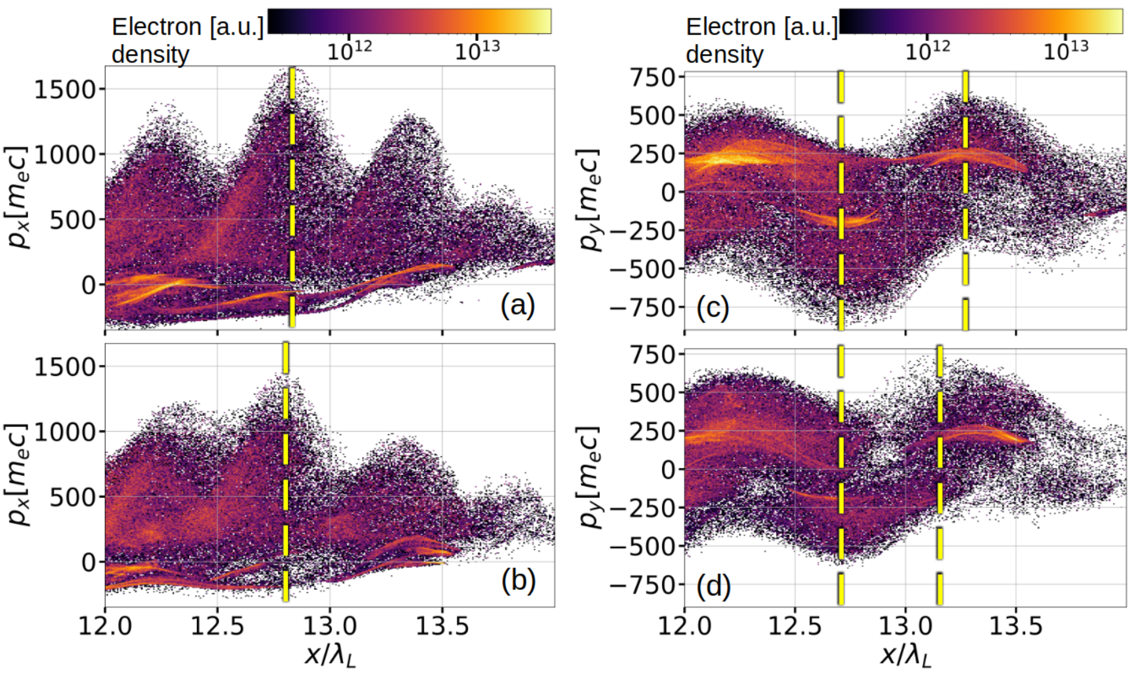

Figure 7.12: Snapshot at 145 fs showing variations in phase-space density distribution between the two models.

7.3 Summary

This chapter presented an examination of the simulation results for the behavior of high-energy electrons in three different models: the EPOCH, the MS, and the

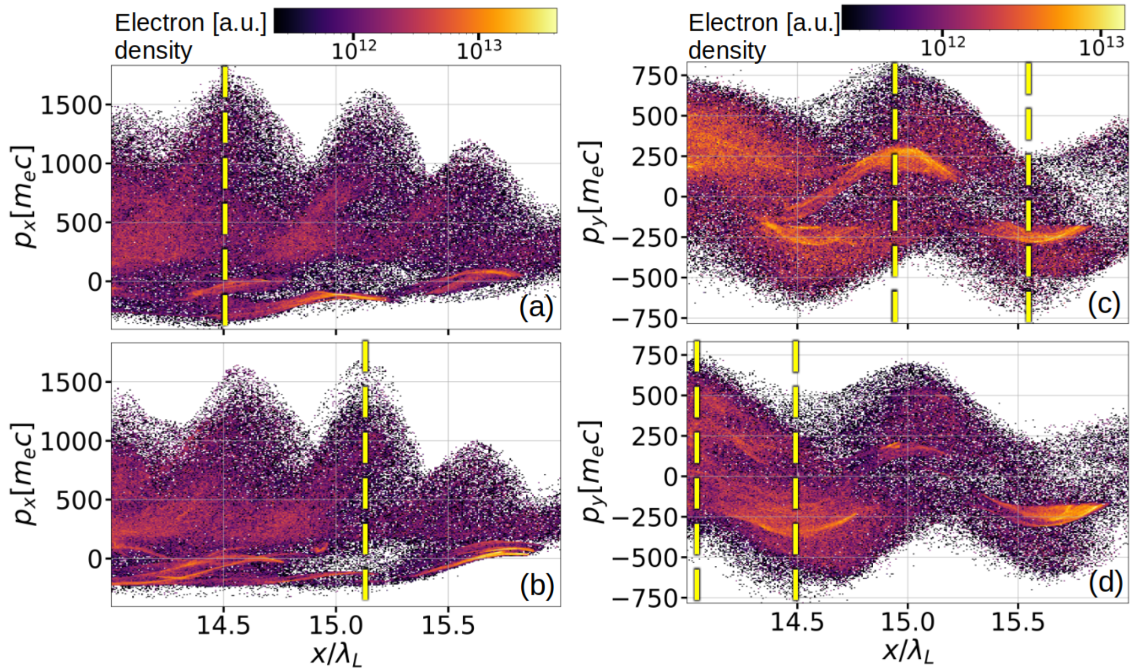

Figure 7.13: Snapshot at 155 fs illustrating the distinct acceleration patterns in each model.

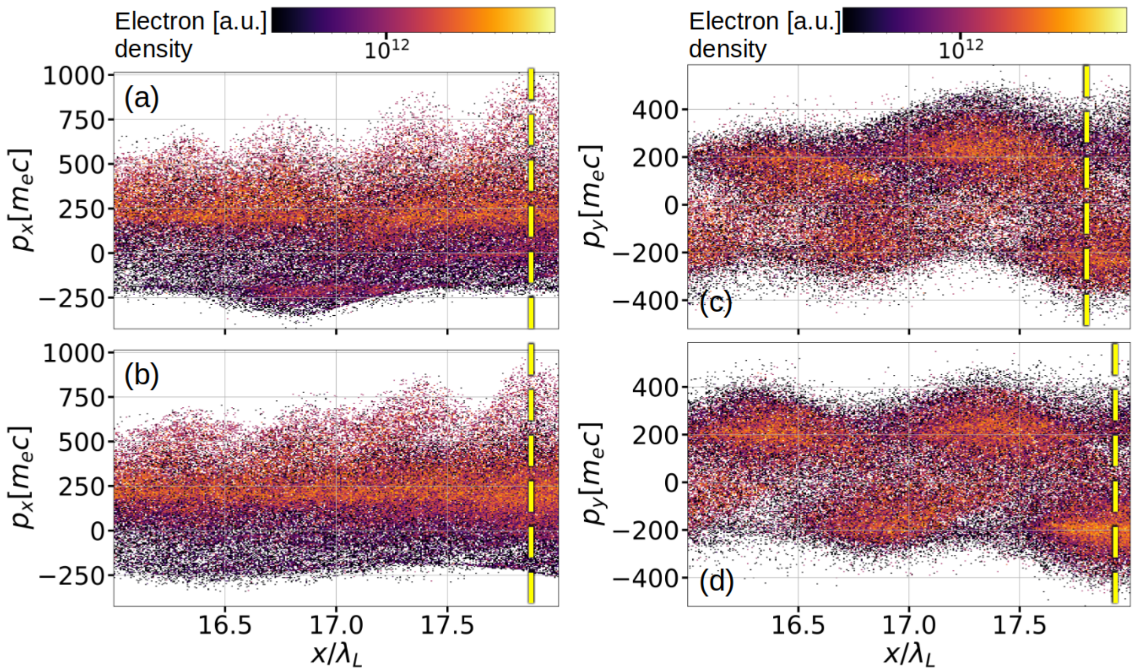

Figure 7.14: Phase-space density distribution at 165 fs showing the spatial differences in maximal momenta.

EMS models. The objective of this study was to demonstrate the suppression of bremsstrahlung emission due to high fields and to detect systematic differences in electron acceleration between the models. The simulations were set up based on specific laser and target parameters, with an emphasis on capturing the impact of the suppression effects at both macroscopic and microscopic levels.

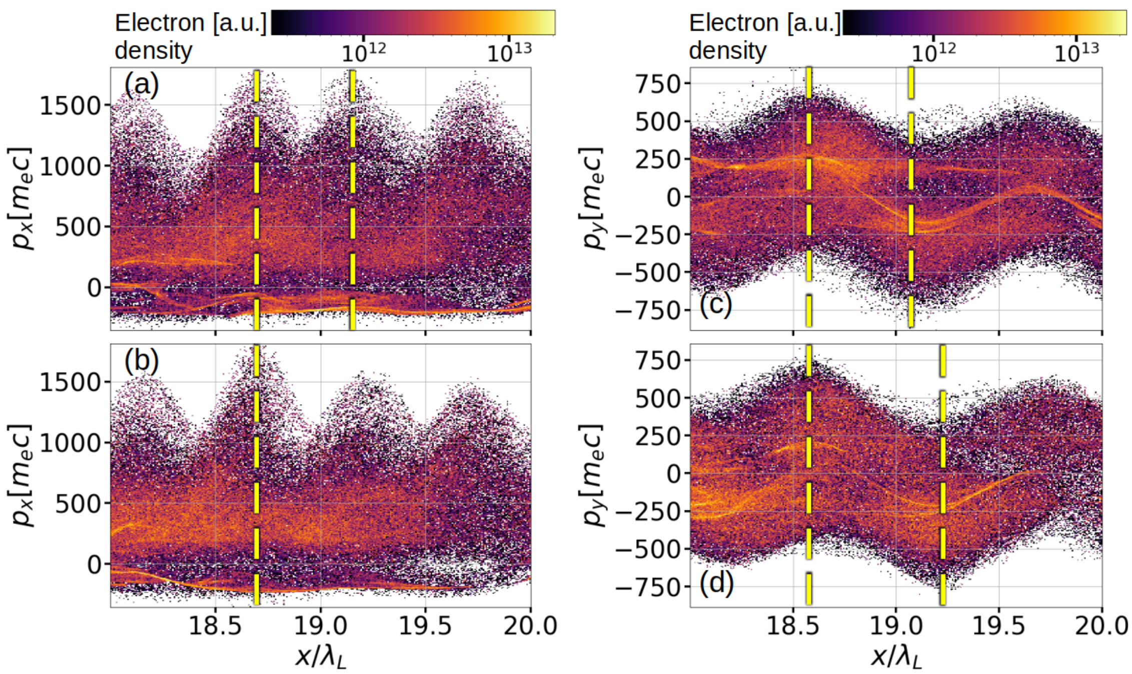

Figure 7.15: Phase-space density distribution at 175 fs exhibiting the variances in momentum positions.

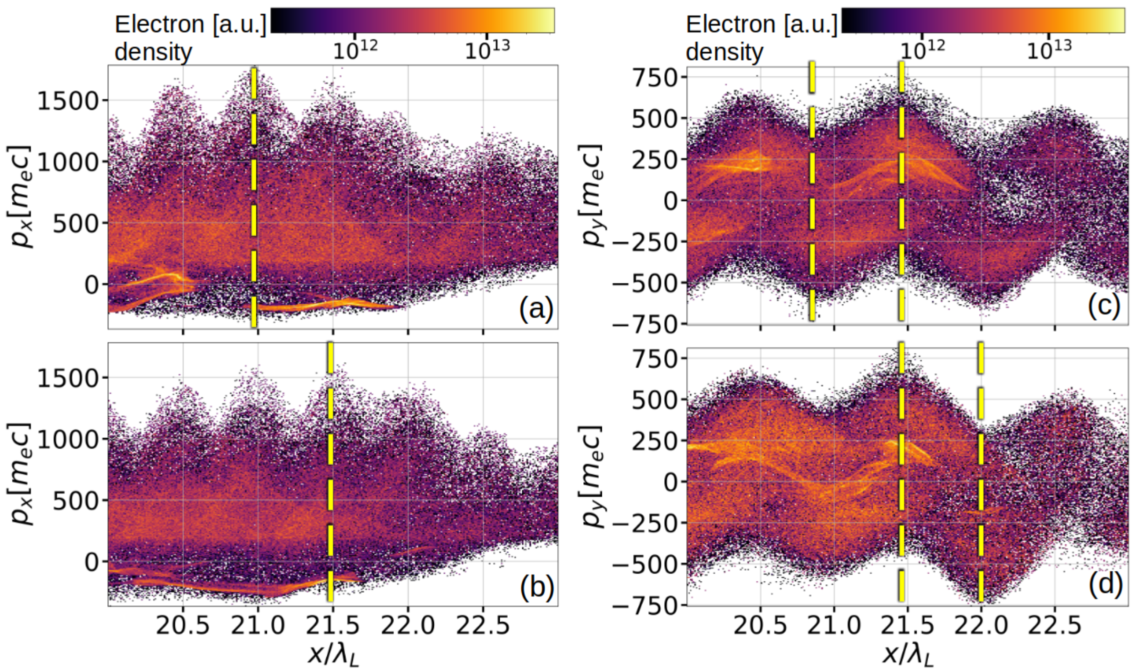

Figure 7.16: Final comparison at 185 fs displaying the subtle changes in acceleration histories for the two models.

At the macroscopic level, we examined the evolution of the total kinetic energy of the electrons and the number of high-energy electrons in each simulation. Despite the differences in the models, the results were found to be statistically comparable, indicating that bremsstrahlung suppression doesn't significantly affect the macroscopic outcomes of laser-plasma interactions.

At the microscopic level, however, the situation was more complex. By focusing on the phase-space distribution of high-energy electrons, significant differences between the EPOCH and EMS models were identified. These discrepancies were particularly noticeable around the peak of laser intensity. We hypothesized that variations in the recoil energies from the EMS effect could lead to different dephasing behaviors between the electrons and accelerating fields, thus impacting the dynamics of electron acceleration. In fact, when dephasing occurs, the electrons no longer experience the full effect of the accelerating electric field, leading to a decrease in their energy gain. This limits the efficiency and effectiveness of the acceleration process.

In summary, our findings suggest that while the suppression of bremsstrahlung radiation does not substantially impact overall electron acceleration, it does influence the specific dynamics of this process. This could have implications for experimental designs where detailed acceleration patterns are crucial.

Chapter 8

Summary and Conclusion

This chapter will conclude our investigation by providing a summary of the most important research results in regard to the research objectives and research questions, as well as their significance and contribution. In addition, it will assess the study's limitations and suggest avenues for further research.

This thesis initiated an exploration into the impact of high fields on bremsstrahlung emission within high-intensity laser-plasma interactions, specifically under the regime of relativistic-induced transparency. The significance of this research is rooted in the potential to enhance our understanding of the bremsstrahlung process in laser-plasma physics, in extreme astrophysical-like conditions, and its applications. These range from laser-driven accelerators to high-energy-density physics.

The investigation began with proposing an extended suppression mechanism model influenced by the presence of strong electric and magnetic fields in high-intensity laser-plasma interactions. This model was integrated into the particle-in-cell code as a new feature for simulation experiments that involve high fields, generating energetic electrons and photons. Subsequently, we conducted computational simulations using three distinct models: the original bremsstrahlung model in the EPOCH code, the modified model by the magnetic suppression (MS) effect, and the newly proposed model by the electric and magnetic suppression (EMS) effect. The models served to examine the behavior of bremsstrahlung emissions generated under relativistic transparency conditions, focusing on both macroscopic and microscopic dynamics. Structured targets were utilized for this purpose, due to their proven abilities in generating collimated energetic electrons and producing strong magnetic fields in simulations.

At the macroscopic level, the distribution energy of the bremsstrahlung emissions and the number of low-energy photons were analyzed across all three models. The results indicated that the presence of macroscopic electric and magnetic fields significantly affected the overall outcomes of bremsstrahlung photons in laser-plasma interactions. However, at the microscopic level, the phase-space density distribution of high-energy electrons highlighted some differences, particularly between the EPOCH and EMS models. These variations were noticeable around the peak of accelerated electrons, suggesting disparities in electron dynamics between the two simulations. Variations in the recoil energies employed by the EMS effect were found to influence the dephasing between the electron and accelerating fields, thereby altering the dynamics of electron acceleration.

A key limitation of this research was the specific choice of plasma target—structured targets—in this case. The need for strong magnetic fields for this investigation limited our choice to only those targets capable of generating energetic electrons and desired magnetic fields. In a real-world scenario, our considered regime tends to produce synchrotron radiation more significantly as compared to generating bremsstrahlung. However, despite the dominance of synchrotron emission over bremsstrahlung in our considered regime, our results provide new insights into bremsstrahlung emission in high-intensity laser-plasma interactions. Moreover, the use of Monte-Carlo simulation routines in both original and modified models might have led to inherent biases in the data, affecting the outcomes.

This study lays the groundwork for future research on the specific effects of bremsstrahlung suppression under various laser-plasma conditions. Additional research could explore the behavior of high-energy electrons at different points of laser intensity or investigate the impacts of varying laser and plasma parameters. Furthermore, this suppression mechanism could be employed to detect strong magnetic fields by having a suitable target, which, in addition to having bremsstrahlung as the dominant emission mechanism, also possesses high fields.

The investigation undertaken in this thesis has yielded new insights into the effects of high fields on bremsstrahlung suppression and consequently on high-energy electron dynamics in the realm of laser-plasma interaction. Although the suppression does not significantly impact overall electron acceleration, it does influence the specific characteristics of electron acceleration dynamics. This has potential implications for experimental designs where detailed acceleration patterns are essential. Moreover, this study suggests that the conventional implementation of bremsstrahlung used by PIC codes may require adjustment to include the discussed suppression effect. The findings from this research emphasize the need for a nuanced understanding of the role of high fields in photon generation and their impact on high-energy electrons and their behavior under various conditions. As our understanding of laser-plasma interactions continues to evolve, we can look forward to further developments in this captivating field of study.

Appendix A

Born Approximation

This discussion examines the mathematical foundations of the Born approximation, a simplification technique frequently used in quantum mechanics. By considering interactions between particles as perturbations of free particle states, the Born approximation aids in the computation of scattering processes. This method is especially useful when the interaction potential is weak and the momentum transfer is small. However, accuracy may be weakened by potent interactions and significant momentum transfers. These derivations are a greatly condensed version of those in several references [216, 238, 246, 252]; readers interested in deeper discussions are encouraged to consult these sources.

Scattering problems typically involve plane wave states for the incident particle and scattered wave states for the outgoing particle. Assume that a plane wave can describe the incident wave function as follows:

$$\psi_i(\mathbf{r}) = e^{i\mathbf{k}\cdot\mathbf{r}}, \tag{A.1}$$

where $\mathbf{k}$ is the wave vector of the incident particle. The final scattering state, denoted as $\psi_f(\mathbf{r})$, can be expressed as a superposition of the incident plane wave and a scattered wave:

$$\psi_f(\mathbf{r}) \approx e^{i\mathbf{k}\cdot\mathbf{r}} + \mathcal{S}(\theta, \phi)\frac{e^{ikr}}{r}, \tag{A.2}$$

where $\mathcal{S}(\theta, \phi)$ is the scattering amplitude that depends on the scattering angles (θ, ϕ). The first term represents the incoming plane wave, while the second term corresponds to the scattered wave, which exhibits a radial dependence of $e^{i\mathbf{k}'\cdot\mathbf{r}}/r$.

Initial and final scattering states are related via the Lippmann-Schwinger equation, which is given for a particle scattered by a potential $V(\boldsymbol{r})$:

$$\psi_f(\mathbf{r}) = \psi_i(\mathbf{r}) + \int d^3r' \mathcal{G}_0(\mathbf{r}, \mathbf{r}')V(\mathbf{r}')\psi_f(\mathbf{r}'), \tag{A.3}$$

where $\mathcal{G}_0(\mathbf{r}, \mathbf{r}')$ is the free-space Green's function for the Schrödinger equation and can be written as:

$$\mathcal{G}_0(\mathbf{r}, \mathbf{r}') = -\frac{1}{4\pi} \frac{e^{ik|\mathbf{r}-\mathbf{r}'|}}{|\mathbf{r}-\mathbf{r}'|}, \tag{A.4}$$

In fact, Expression (A.3) can be considered as the general solution of the Schrödinger equation for scattering wavefunction. Using (A.4), the common form of the Lippmann-Schwinger equation in far-field (i.e., $|\mathbf{r}-\mathbf{r}'| \sim r - \hat{\mathbf{r}} \cdot \mathbf{r}' + \dots$) is expressed by,

$$\psi_f(\mathbf{r}) = e^{i\mathbf{k}\cdot\mathbf{r}} - \frac{1}{4\pi} \frac{e^{ikr}}{r} \int d^3r' e^{-i\mathbf{k}'\cdot\mathbf{r}'} V(\mathbf{r}') \psi_f(\mathbf{r}'), \tag{A.5}$$

The Born approximation simplifies the Lippmann-Schwinger equation by assuming that the scattered wave $\psi_f(\mathbf{r})$ is only weakly affected by the potential $V(\boldsymbol{r})$. In this approximation, $\psi_f(\mathbf{r})$ is replaced with $\psi_i(\mathbf{r})$ on the right side of the equation:

$$\psi_f^{(q)}(\mathbf{r}) = e^{i\mathbf{k}\cdot\mathbf{r}} - \frac{1}{4\pi} \frac{e^{ikr}}{r} \int d^3r' e^{-i\mathbf{k}'\cdot\mathbf{r}'} V(\mathbf{r}') \psi_i^{(q-1)}(\mathbf{r}),, \tag{A.6}$$

For the first Born approximation, $\psi_i^{(0)}(\mathbf{r}) = e^{i\mathbf{k}\cdot\mathbf{r}}$, where scattering wavefunction corresponds to incident plane wave without perturbation,(A.6) can be simplified as follows:

$$\psi_f^{(1)}(\mathbf{r}) = e^{i\mathbf{k}\cdot\mathbf{r}} - \frac{1}{4\pi} \frac{e^{ikr}}{r} \int d^3r' e^{i\mathbf{q}\cdot\mathbf{r}'} V(\mathbf{r}'), \tag{A.7}$$

where $\boldsymbol{q} = \boldsymbol{k} - \boldsymbol{k'}$ which represents the momentum transfer with the incident and scattered wave vectors $\boldsymbol{k}$ and $\boldsymbol{k'}$, respectively. With comparing (A.7) with the scattered wave component of $\psi_f(\boldsymbol{r})$ in Equation A.2, the scattering amplitude $\mathcal{S}(\theta, \phi)$ is extracted as,

$$\mathcal{S}(\theta, \phi) \approx -\frac{1}{4\pi} \int d^3r' e^{i\mathbf{q}\cdot\mathbf{r}'} V(\mathbf{r}'), \tag{A.8}$$

Note that using this scattering amplitude, one could estimate differential cross-section per solid angle, $d\Omega$, as follows:

$$\frac{d\sigma}{d\Omega} = |\mathcal{S}(\theta, \phi)|^2 \tag{A.9}$$

While the Born approximation significantly simplifies the calculation of the scattering amplitude for weakly interacting particles, it is critical to note that this approximation may not yield accurate results for strong scattering potentials or when higher-order effects are significant. Thus, the applicability of the Born approximation should always be evaluated in the context of the specific scattering problem at hand. Nonetheless, the Born approximation serves as a powerful tool in quantum mechanics, especially for problems involving weak interactions and small momentum transfers.

Bibliography

[1] Joseph K Daugherty and Alice K Harding. "Pair production in superstrong magnetic fields". In: (1983).

[2] Alice K Harding. "Physics in strong magnetic fields near neutron stars". In: *Science* 251.4997 (1991), pp. 1033–1038.

[3] Mikhail A Liberman and B Johansson. "Properties of matter in ultrahigh magnetic fields and the structure of the surface of neutron stars". In: *Physics-Uspekhi* 38.2 (1995), p. 117.

[4] Matthew G Baring and Alice K Harding. "Radio-quiet pulsars with ultrastrong magnetic fields". In: *The Astrophysical Journal* 507.1 (1998), p. L55.

[5] DT Wickramasinghe and Lilia Ferrario. "Magnetism in isolated and binary white dwarfs". In: *Publications of the Astronomical Society of the Pacific* 112.773 (2000), p. 873.

[6] Roberto Turolla, Silvia Zane, and AL Watts. "Magnetars: the physics behind observations. A review". In: *Reports on Progress in Physics* 78.11 (2015), p. 116901.

[7] Yulan Liu. "Interstellar Scintillation Studies of EPTA Pulsars". In: (2022).

[8] Fernando Camilo et al. "Discovery of two high magnetic field radio pulsars". In: *The Astrophysical Journal* 541.1 (2000), p. 367.

[9] Colin N Danson et al. "Petawatt and exawatt class lasers worldwide". In: *High Power Laser Science and Engineering* 7 (2019), e54.

[10] Jin Woo Yoon et al. "Achieving the laser intensity of 5.5× 10 22 W/cm 2 with a wavefront-corrected multi-PW laser". In: *Optics express* 27.15 (2019), pp. 20412–20420.

[11] François Lureau et al. "High-energy hybrid femtosecond laser system demonstrating 2× 10 PW capability". In: *High Power Laser Science and Engineering* 8 (2020), e43.

[12] Christophe Radier et al. “10 PW peak power femtosecond laser pulses at ELI-NP”. In: *High Power Laser Science and Engineering* 10 (2022), e21.

[13] Barbara F Lasinski et al. “Particle-in-cell simulations of ultra intense laser pulses propagating through overdense plasma for fast-ignitor and radiography applications”. In: *Physics of Plasmas* 6.5 (1999), pp. 2041–2047.

[14] SV Bulanov et al. “Ion acceleration in a dipole vortex in a laser plasma corona”. In: *Plasma physics reports* 31 (2005), pp. 369–381.

[15] Tatsufumi Nakamura et al. “High-energy ions from near-critical density plasmas via magnetic vortex acceleration”. In: *Physical review letters* 105.13 (2010), p. 135002.

[16] Jaehong Park et al. “Ion acceleration in laser generated megatesla magnetic vortex”. In: *Physics of Plasmas* 26.10 (2019), p. 103108.

[17] Z Gong et al. “Direct laser acceleration of electrons assisted by strong laser-driven azimuthal plasma magnetic fields”. In: *Physical Review E* 102.1 (2020), p. 013206.

[18] Predhiman Kaw and John Dawson. “Relativistic nonlinear propagation of laser beams in cold overdense plasmas”. In: *The Physics of Fluids* 13.2 (1970), pp. 472–481.

[19] SE Harris. “Electromagnetically induced transparency in an ideal plasma”. In: *Physical review letters* 77.27 (1996), p. 5357.

[20] F Cattani et al. “Threshold of induced transparency in the relativistic interaction of an electromagnetic wave with overdense plasmas”. In: *Physical Review E* 62.1 (2000), p. 1234.

[21] VV Goloviznin and TJ Schep. “Self-induced transparency and self-induced opacity in laser-plasma interactions”. In: *Physics of Plasmas* 7.5 (2000), pp. 1564–1571.

[22] M Tushentsov et al. “Electromagnetic energy penetration in the self-induced transparency regime of relativistic laser-plasma interactions”. In: *Physical review letters* 87.27 (2001), p. 275002.

[23] VI Eremin, AV Korzhimanov, and AV Kim. “Relativistic self-induced transparency effect during ultraintense laser interaction with overdense plasmas: Why it occurs and its use for ultrashort electron bunch generation”. In: *Physics of Plasmas* 17.4 (2010), p. 043102.

[24] Sasi Palaniyappan et al. “Dynamics of relativistic transparency and optical shuttering in expanding overdense plasmas”. In: *Nature Physics* 8.10 (2012), pp. 763–769.

[25] E Siminos et al. “Effect of electron heating on self-induced transparency in relativistic-intensity laser-plasma interactions”. In: *Physical Review E* 86.5 (2012), p. 056404.

[26] Z Gong et al. “Highly collimated electron acceleration by longitudinal laser fields in a hollow-core target”. In: *Plasma Physics and Controlled Fusion* 61.3 (2019), p. 035012.

[27] DJ Stark, Toma Toncian, and AV Arefiev. “Enhanced multi-MeV photon emission by a laser-driven electron beam in a self-generated magnetic field”. In: *Physical review letters* 116.18 (2016), p. 185003.

[28] HX Chang et al. “Brilliant petawatt gamma-ray pulse generation in quantum electrodynamic laser-plasma interaction”. In: *Scientific reports* 7.1 (2017), p. 45031.

[29] T Wang et al. “Power scaling for collimated γ-ray beams generated by structured laser-irradiated targets and its application to two-photon pair production”. In: *Physical Review Applied* 13.5 (2020), p. 054024.

[30] Yutong He et al. “Dominance of γ-γ electron-positron pair creation in a plasma driven by high-intensity lasers”. In: *Communications Physics* 4.1 (2021), p. 139.

[31] Y He et al. “A single-laser scheme for observation of linear Breit–Wheeler electron–positron pair creation”. In: *New Journal of Physics* 23.11 (2021), p. 115005.

[32] Y He and A Arefiev. “Algorithm for computing the electron-positron yield from the linear Breit-Wheeler process in high-intensity laser-plasma interactions”. In: *Computer Physics Communications* (2023), p. 108657.

[33] Spencer Klein. “Suppression of bremsstrahlung and pair production due to environmental factors”. In: *Reviews of Modern Physics* 71.5 (1999), p. 1501.

[34] Spencer R Klein. “Bremsstrahlung and pair creation: Suppression mechanisms and how they affect EHE air showers”. In: *AIP Conference Proceedings CONF-9711122*. Vol. 433. 1. American Institute of Physics. 1998, pp. 132–147.

[35] TD Arber et al. “Contemporary particle-in-cell approach to laser-plasma modelling”. In: *Plasma Physics and Controlled Fusion* 57.11 (2015), p. 113001.

[36] Jiří Vyskočil, Ondřej Klimo, and Stefan Weber. “Simulations of bremsstrahlung emission in ultra-intense laser interactions with foil targets”. In: *Plasma Physics and Controlled Fusion* 60.5 (2018), p. 054013.

[37] Jérôme Faure et al. “A laser–plasma accelerator producing monoenergetic electron beams”. In: *Nature* 431.7008 (2004), pp. 541–544.

[38] Stuart PD Mangles et al. “Monoenergetic beams of relativistic electrons from intense laser–plasma interactions”. In: *Nature* 431.7008 (2004), pp. 535–538.

[39] H Schwoerer et al. “Laser-plasma acceleration of quasi-monoenergetic protons from microstructured targets”. In: *Nature* 439.7075 (2006), pp. 445–448.

[40] Victor Malka et al. “Principles and applications of compact laser–plasma accelerators”. In: *Nature physics* 4.6 (2008), pp. 447–453.

[41] Wim Leemans and Eric Esarey. “Laser-driven plasma-wave electron accelerators”. In: *Phys. Today* 62.3 (2009), pp. 44–49.

[42] Eric Esarey, Carl B Schroeder, and Wim P Leemans. “Physics of laser-driven plasma-based electron accelerators”. In: *Reviews of modern physics* 81.3 (2009), p. 1229.

[43] Olle Lundh et al. “Few femtosecond, few kiloampere electron bunch produced by a laser–plasma accelerator”. In: *Nature Physics* 7.3 (2011), pp. 219–222.

[44] Victor Malka. “Laser plasma accelerators”. In: *Laser-Plasma Interactions and Applications*. Springer, 2013, pp. 281–301.

[45] Xiaoming Wang et al. “Quasi-monoenergetic laser-plasma acceleration of electrons to 2 GeV”. In: *Nature communications* 4.1 (2013), p. 1988.

[46] Simon Martin Hooker. “Developments in laser-driven plasma accelerators”. In: *Nature Photonics* 7.10 (2013), pp. 775–782.

[47] T Tajima and V Malka. “Laser plasma accelerators”. In: *Plasma Physics and Controlled Fusion* 62.3 (2020), p. 034004.

[48] FV Hartemann et al. “High-energy scaling of Compton scattering light sources”. In: *Physical Review Special Topics-Accelerators and Beams* 8.10 (2005), p. 100702.

[49] Yannick Glinec et al. “High-resolution γ-ray radiography produced by a laser-plasma driven electron source”. In: *Physical review letters* 94.2 (2005), p. 025003.

[50] Jean Galy et al. “Bremsstrahlung production with high-intensity laser matter interactions and applications”. In: *New journal of Physics* 9.2 (2007), p. 23.

[51] H-P Schlenvoigt et al. “A compact synchrotron radiation source driven by a laser-plasma wakefield accelerator”. In: *Nature Physics* 4.2 (2008), pp. 130–133.

[52] Matthias Fuchs et al. “Laser-driven soft-X-ray undulator source”. In: *Nature physics* 5.11 (2009), pp. 826–829.

[53] Stefan Kneip et al. “Bright spatially coherent synchrotron X-rays from a table-top source”. In: *Nature Physics* 6.12 (2010), pp. 980–983.

[54] Sébastien Corde et al. “Femtosecond x rays from laser-plasma accelerators”. In: *Reviews of Modern Physics* 85.1 (2013), p. 1.

[55] S Chen et al. “MeV-energy X rays from inverse Compton scattering with laser-wakefield accelerated electrons”. In: *Physical review letters* 110.15 (2013), p. 155003.

[56] M Roth et al. “Bright laser-driven neutron source based on the relativistic transparency of solids”. In: *Physical review letters* 110.4 (2013), p. 044802.

[57] Félicie Albert and Alec GR Thomas. “Applications of laser wakefield accelerator-based light sources”. In: *Plasma Physics and Controlled Fusion* 58.10 (2016), p. 103001.

[58] A Nishiguchi et al. “Convective amplification of magnetic fields in laser-produced plasmas by the Nernst effect”. In: *Physical review letters* 53.3 (1984), p. 262.

[59] C Courtois et al. “Creation of a uniform high magnetic-field strength environment for laser-driven experiments”. In: *Journal of applied physics* 98.5 (2005), p. 054913.

[60] OV Gotchev et al. “Laser-driven magnetic-flux compression in high-energy-density plasmas”. In: *Physical review letters* 103.21 (2009), p. 215004.

[61] Shinsuke Fujioka et al. “Kilotesla magnetic field due to a capacitor-coil target driven by high power laser”. In: *Scientific reports* 3.1 (2013), pp. 1–7.

[62] JJ Santos et al. “Laser-driven platform for generation and characterization of strong quasi-static magnetic fields”. In: *New Journal of Physics* 17.8 (2015), p. 083051.

[63] K Jiang, A Pukhov, and CT Zhou. “Magnetic field amplification to gigagauss scale via hydrodynamic flows and dynamos driven by femtosecond lasers”. In: *New Journal of Physics* 23.6 (2021), p. 063054.

[64] DR Farley et al. “Radiative jet experiments of astrophysical interest using intense lasers”. In: *Physical Review Letters* 83.10 (1999), p. 1982.

[65] Bruce A Remington et al. “A review of astrophysics experiments on intense lasers”. In: *Physics of Plasmas* 7.5 (2000), pp. 1641–1652.

[66] Hideaki Takabe. “Astrophysics with intense and ultra-intense lasers “laser astrophysics””. In: *Progress of Theoretical Physics Supplement* 143 (2001), pp. 202–265.

[67] Yuri P Zakharov. “Collisionless laboratory astrophysics with lasers”. In: *IEEE transactions on plasma science* 31.6 (2003), pp. 1243–1251.

[68] Bruce A Remington. “High energy density laboratory astrophysics”. In: *Plasma Physics and Controlled Fusion* 47.5A (2005), A191.

[69] Bruce A Remington, R Paul Drake, and Dmitri D Ryutov. “Experimental astrophysics with high power lasers and Z pinches”. In: *Reviews of Modern Physics* 78.3 (2006), p. 755.

[70] T Ditmire et al. “Laboratory simulations of astrophysical blastwaves using intense laser interactions”. In: *Quantum Electronics and Laser Science Conference*. Optica Publishing Group. 2007, JThG4.

[71] T Zh Esirkepov and SV Bulanov. “Fundamental physics and relativistic laboratory astrophysics with extreme power lasers”. In: *European Astronomical Society Publications Series* 58 (2012), pp. 7–22.

[72] A Di Piazza et al. “Extremely high-intensity laser interactions with fundamental quantum systems”. In: *Reviews of Modern Physics* 84.3 (2012), p. 1177.

[73] Hye-Sook Park et al. “Studying astrophysical collisionless shocks with counterstreaming plasmas from high power lasers”. In: *High Energy Density Physics* 8.1 (2012), pp. 38–45.

[74] Hideaki Takabe and Yasuhiro Kuramitsu. “Recent progress of laboratory astrophysics with intense lasers”. In: *High Power Laser Science and Engineering* 9 (2021), e49.

[75] F Pegoraro et al. “Magnetic fields from high-intensity laser pulses in plasmas”. In: *Plasma Physics and Controlled Fusion* 39.12B (1997), B261.

[76] M Tatarakis et al. “Measurements of ultrastrong magnetic fields during relativistic laser–plasma interactions”. In: *Physics of Plasmas* 9.5 (2002), pp. 2244–2250.

[77] G Gregori et al. "Generation of scaled protogalactic seed magnetic fields in laser-produced shock waves". In: *Nature* 481.7382 (2012), pp. 480–483.

[78] É Falize et al. "High-energy density laboratory astrophysics studies of accretion shocks in magnetic cataclysmic variables". In: *High Energy Density Physics* 8.1 (2012), pp. 1–4.

[79] NL Kugland et al. "Visualizing electromagnetic fields in laser-produced counter-streaming plasma experiments for collisionless shock laboratory astrophysics". In: *Physics of Plasmas* 20.5 (2013), p. 056313.

[80] A Ciardi et al. "Astrophysics of magnetically collimated jets generated from laser-produced plasmas". In: *Physical review letters* 110.2 (2013), p. 025002.

[81] VS Belyaev et al. "Promising lines of investigations in the realms of laboratory astrophysics with the aid of powerful lasers". In: *Physics of Atomic Nuclei* 76 (2013), pp. 404–422.

[82] Ph Korneev, Emmanuel d'Humières, and Vladimir Tikhonchuk. "Collisionless plasma interpenetration in a strong magnetic field for laboratory astrophysics experiments". In: *Physics of Plasmas* 21.2 (2014), p. 022117.

[83] B Albertazzi et al. "Laboratory formation of a scaled protostellar jet by coaligned poloidal magnetic field". In: *Science* 346.6207 (2014), pp. 325–328.

[84] G Gregori, Brian Reville, and Francesco Miniati. "The generation and amplification of intergalactic magnetic fields in analogue laboratory experiments with high power lasers". In: *Physics Reports* 601 (2015), pp. 1–34.

[85] BJ Zhu et al. "Strong magnetic fields generated with a simple open-ended coil irradiated by high power laser pulses". In: *Applied Physics Letters* 107.26 (2015), p. 261903.

[86] Jena Meinecke et al. "Developed turbulence and nonlinear amplification of magnetic fields in laboratory and astrophysical plasmas". In: *Proceedings of the National Academy of Sciences* 112.27 (2015), pp. 8211–8215.

[87] B Khiar et al. "Laser-produced magnetic-Rayleigh-Taylor unstable plasma slabs in a 20 T magnetic field". In: *Physical Review Letters* 123.20 (2019), p. 205001.

[88] M Murakami et al. "Generation of megatesla magnetic fields by intense-laser-driven microtube implosions". In: *Scientific reports* 10.1 (2020), p. 16653.

[89] Francis F Chen. *Introduction to plasma physics*. Springer Science & Business Media, 2012.

[90] William Kruer. *The physics of laser plasma interactions.* crc Press, 2019.

[91] Setsuo Ichimaru. *Basic principles of plasma physics: a statistical approach.* CRC Press, 2018.

[92] Dino A Jaroszynski, RA Bingham, and RA Cairns. *Laser-plasma interactions.* CRC Press, 2009.

[93] TJ M Boyd, TJM Boyd, and JJ Sanderson. *The physics of plasmas.* Cambridge university press, 2003.

[94] José A Bittencourt. *Fundamentals of plasma physics.* Springer Science & Business Media, 2004.

[95] Frederik Böhle. "Near-single-cycle laser for driving relativistic plasma mirrors at kHz repetition rate-development and application". PhD thesis. Université Paris Saclay (COmUE), 2017.

[96] Paul M Bellan. *Fundamentals of plasma physics.* Cambridge university press, 2008.

[97] Robert J Goldston. *Introduction to plasma physics.* CRC Press, 2020.

[98] Donna Strickland and Gerard Mourou. "Compression of amplified chirped optical pulses". In: *Optics communications* 55.6 (1985), pp. 447–449.

[99] Gerard A Mourou, Toshiki Tajima, and Sergei V Bulanov. "Optics in the relativistic regime". In: *Reviews of modern physics* 78.2 (2006), p. 309.

[100] Sterling Backus et al. "High power ultrafast lasers". In: *Review of scientific instruments* 69.3 (1998), pp. 1207–1223.

[101] Jean-Claude Diels and Wolfgang Rudolph. *Ultrashort laser pulse phenomena.* Elsevier, 2006.

[102] Paul McKenna et al. *Laser-plasma interactions and applications.* Springer, 2013.

[103] Colin Danson et al. "Petawatt class lasers worldwide". In: *High power laser science and engineering* 3 (2015), e3.

[104] William M Steen and Jyotirmoy Mazumder. *Laser material processing.* springer science & business media, 2010.

[105] Todd Ditmire et al. "Nuclear fusion from explosions of femtosecond laser-heated deuterium clusters". In: *Nature* 398.6727 (1999), pp. 489–492.

[106] M Roth et al. "Fast ignition by intense laser-accelerated proton beams". In: *Physical review letters* 86.3 (2001), p. 436.

[107] Stefano Atzeni and Jürgen Meyer-ter-Vehn. *The physics of inertial fusion: beam plasma interaction, hydrodynamics, hot dense matter*. Vol. 125. OUP Oxford, 2004.

[108] George H Miller, Edward I Moses, and Craig R Wuest. "The National Ignition Facility: enabling fusion ignition for the 21st century". In: *Nuclear fusion* 44.12 (2004), S228.

[109] Kristian Herrlin et al. "Generation of x rays for medical imaging by high-power lasers: preliminary results." In: *Radiology* 189.1 (1993), pp. 65–68.

[110] KWD Ledingham et al. "High power laser production of short-lived isotopes for positron emission tomography". In: *Journal of Physics D: Applied Physics* 37.16 (2004), p. 2341.

[111] VS Cherkassky et al. "Imaging techniques for a high-power THz free electron laser". In: *Nuclear Instruments and Methods in Physics Research Section A: Accelerators, Spectrometers, Detectors and Associated Equipment* 543.1 (2005), pp. 102–109.

[112] Ivan Vladimirovich Yakovlev. "Stretchers and compressors for ultra-high power laser systems". In: *Quantum Electronics* 44.5 (2014), p. 393.

[113] *High-power Lasers*. `https://www.americanscientist.org/article/high-power-lasers`. Illustration by Barbara Aulicino.

[114] Thomas Brabec and Ferenc Krausz. "Intense few-cycle laser fields: Frontiers of nonlinear optics". In: *Reviews of Modern Physics* 72.2 (2000), p. 545.

[115] Ursula Keller. "Recent developments in compact ultrafast lasers". In: *nature* 424.6950 (2003), pp. 831–838.

[116] Pierre Agostini and Louis F DiMauro. "The physics of attosecond light pulses". In: *Reports on progress in physics* 67.6 (2004), p. 813.

[117] S Gales et al. "The extreme light infrastructure—nuclear physics (ELI-NP) facility: new horizons in physics with 10 PW ultra-intense lasers and 20 MeV brilliant gamma beams". In: *Reports on Progress in Physics* 81.9 (2018), p. 094301.

[118] Artem V Korzhimanov et al. "Horizons of petawatt laser technology". In: *Physics-Uspekhi* 54.1 (2011), p. 9.

[119] Ganesh Tiwari et al. "Beam distortion effects upon focusing an ultrashort petawatt laser pulse to greater than 10 22 W/cm 2". In: *Optics Letters* 44.11 (2019), pp. 2764–2767.

[120] Paul Gibbon. *Short pulse laser interactions with matter: an introduction.* World Scientific, 2005.

[121] Hideaki Takabe. *The Physics of laser plasmas and applications-Volume 1: physics of laser matter interaction.* Springer Nature, 2020.

[122] F Chen Francis. *Introduction to plasma physics and controlled fusion.* 2016.

[123] SV Bulanov, F Pegoraro, and AM Pukhov. "Two-dimensional regimes of self-focusing, wake field generation, and induced focusing of a short intense laser pulse in an underdense plasma". In: *Physical review letters* 74.5 (1995), p. 710.

[124] Donald Umstadter. "Relativistic laser–plasma interactions". In: *Journal of Physics D: Applied Physics* 36.8 (2003), R151.

[125] T Ditmire et al. "Interaction of intense laser pulses with atomic clusters". In: *Physical Review A* 53.5 (1996), p. 3379.

[126] Paul Gibbon and Eckhart Förster. "Short-pulse laser-plasma interactions". In: *Plasma physics and controlled fusion* 38.6 (1996), p. 769.

[127] Andrea Macchi et al. "Laser acceleration of ion bunches at the front surface of overdense plasmas". In: *Physical review letters* 94.16 (2005), p. 165003.

[128] A Pukhov and J Meyer-ter-Vehn. "Relativistic magnetic self-channeling of light in near-critical plasma: three-dimensional particle-in-cell simulation". In: *Physical review letters* 76.21 (1996), p. 3975.

[129] RHH Scott et al. "A study of fast electron energy transport in relativistically intense laser-plasma interactions with large density scalelengths". In: *Physics of Plasmas* 19.5 (2012), p. 053104.

[130] Patrick Mora. "Plasma expansion into a vacuum". In: *Physical Review Letters* 90.18 (2003), p. 185002.

[131] Toshiki Tajima and John M Dawson. "Laser electron accelerator". In: *Physical review letters* 43.4 (1979), p. 267.

[132] P Sprangle et al. "Laser wakefield acceleration and relativstic optical guiding". In: *AIP Conference Proceedings.* Vol. 175. 1. American Institute of Physics. 1988, pp. 231–239.

[133] Wei Lu et al. "Generating multi-GeV electron bunches using single stage laser wakefield acceleration in a 3D nonlinear regime". In: *Physical Review Special Topics-Accelerators and Beams* 10.6 (2007), p. 061301.

[134] Chris E Clayton et al. “Self-guided laser wakefield acceleration beyond 1 GeV using ionization-induced injection”. In: *Physical review letters* 105.10 (2010), p. 105003.

[135] Hyung Taek Kim et al. “Enhancement of electron energy to the multi-GeV regime by a dual-stage laser-wakefield accelerator pumped by petawatt laser pulses”. In: *Physical review letters* 111.16 (2013), p. 165002.

[136] NE Andreev et al. “On laser wakefield acceleration in plasma channels”. In: *Nuclear Instruments and Methods in Physics Research Section A: Accelerators, Spectrometers, Detectors and Associated Equipment* 410.3 (1998), pp. 469–476.

[137] Phillip Sprangle et al. “Wakefield generation and GeV acceleration in tapered plasma channels”. In: *Physical Review E* 63.5 (2001), p. 056405.

[138] K Nakamura et al. “GeV electron beams from a centimeter-scale channel guided laser wakefield accelerator”. In: *Physics of Plasmas* 14.5 (2007), p. 056708.

[139] Mark J Hogan. “Electron and positron beam–driven plasma acceleration”. In: *Reviews of Accelerator Science and Technology* 9 (2016), pp. 63–83.

[140] Altan Cakir and Oguz Guzel. “A Brief Review of Plasma Wakefield Acceleration”. In: *arXiv preprint arXiv:1908.07207* (2019).

[141] Hyung Taek Kim et al. “Multi-gev laser wakefield electron acceleration with pw lasers”. In: *Applied Sciences* 11.13 (2021), p. 5831.

[142] Alexander Pukhov. “Three-dimensional electromagnetic relativistic particle-in-cell code VLPL (Virtual Laser Plasma Lab)”. In: *Journal of plasma physics* 61.3 (1999), pp. 425–433.

[143] C Gahn et al. “Multi-MeV electron beam generation by direct laser acceleration in high-density plasma channels”. In: *Physical Review Letters* 83.23 (1999), p. 4772.

[144] Stuart PD Mangles et al. “Electron acceleration in cavitated channels formed by a petawatt laser in low-density plasma”. In: *Physical review letters* 94.24 (2005), p. 245001.

[145] AV Arefiev et al. “Beyond the ponderomotive limit: Direct laser acceleration of relativistic electrons in sub-critical plasmas”. In: *Physics of Plasmas* 23.5 (2016), p. 056704.

[146] AV Arefiev, APL Robinson, and VN Khudik. “Novel aspects of direct laser acceleration of relativistic electrons”. In: *Journal of Plasma Physics* 81.4 (2015), p. 475810404.

[147] Alexander Pukhov. "Strong field interaction of laser radiation". In: *Reports on progress in Physics* 66.1 (2002), p. 47.

[148] Yannick Glinec et al. "Direct observation of betatron oscillations in a laser-plasma electron accelerator". In: *Europhysics Letters* 81.6 (2008), p. 64001.

[149] Oliver Jansen et al. "Leveraging extreme laser-driven magnetic fields for gamma-ray generation and pair production". In: *Plasma Physics and Controlled Fusion* 60.5 (2018), p. 054006.

[150] Julia M Mikhailova et al. "Isolated attosecond pulses from laser-driven synchrotron radiation". In: *Physical review letters* 109.24 (2012), p. 245005.

[151] LM Chen et al. "Bright betatron X-ray radiation from a laser-driven-clustering gas target". In: *Scientific reports* 3.1 (2013), p. 1912.

[152] CM Brenner et al. "Laser-driven x-ray and neutron source development for industrial applications of plasma accelerators". In: *Plasma Physics and Controlled Fusion* 58.1 (2015), p. 014039.

[153] Philip Willmott. *An introduction to synchrotron radiation: techniques and applications*. John Wiley & Sons, 2019.

[154] E Esarey et al. "Synchrotron radiation from electron beams in plasma-focusing channels". In: *Physical Review E* 65.5 (2002), p. 056505.

[155] Antoine Rousse et al. "Production of a keV X-ray beam from synchrotron radiation in relativistic laser-plasma interaction". In: *Physical review letters* 93.13 (2004), p. 135005.

[156] O Jansen et al. "Collimated gamma-ray beams from structured laser-irradiated targets–how to increase the efficiency without increasing the laser intensity". In: *arXiv preprint arXiv:1908.06467* (2019).

[157] Bertrand Martinez, Emmanuel d'Humières, and Laurent Gremillet. "Synchrotron radiation from ultrahigh-intensity laser-plasma interactions and competition with Bremsstrahlung in thin foil targets". In: *Physical Review Research* 2.4 (2020), p. 043341.

[158] Eberhard Haug and Werner Nakel. *The elementary process of bremsstrahlung*. Vol. 73. World Scientific, 2004.

[159] Silvia Cipiccia et al. "A tuneable ultra-compact high-power, ultra-short pulsed, bright gamma-ray source based on bremsstrahlung radiation from laser-plasma accelerated electrons". In: *Journal of Applied Physics* 111.6 (2012), p. 063302.

[160] RD Edwards et al. “Characterization of a gamma-ray source based on a laser-plasma accelerator with applications to radiography”. In: *Applied Physics Letters* 80.12 (2002), pp. 2129–2131.

[161] C Courtois et al. “High-resolution multi-MeV x-ray radiography using relativistic laser-solid interaction”. In: *Physics of Plasmas* 18.2 (2011), p. 023101.

[162] A Giulietti et al. “Intense γ-ray source in the giant-dipole-resonance range driven by 10-TW laser pulses”. In: *Physical review letters* 101.10 (2008), p. 105002.

[163] C Zulick et al. “High resolution bremsstrahlung and fast electron characterization in ultrafast intense laser–solid interactions”. In: *New Journal of Physics* 15.12 (2013), p. 123038.

[164] CD Armstrong et al. “Bremsstrahlung emission profile from intense laser-solid interactions as a function of laser focal spot size”. In: *Plasma Physics and Controlled Fusion* 61.3 (2019), p. 034001.

[165] Xu Miaohua, Liang Tianjiao, and Zhang Jie. “Bremsstrahlung diagnostics of hot electrons in laser-plasma interactions”. In: *Acta Physica Sinica* 55 (2006).

[166] Anthony L Meadowcroft and Ray D Edwards. “High-energy bremsstrahlung diagnostics to characterize hot-electron production in short-pulse laser-plasma experiments”. In: *IEEE Transactions on Plasma Science* 40.8 (2012), pp. 1992–2001.

[167] International Bureau of Weights et al. *The international system of units (SI)*. US Department of Commerce, Technology Administration, National Institute of . . ., 2001.

[168] Chryssa Kouveliotou, Robert C Duncan, and Christopher Thompson. “Magnetars”. In: *Scientific American* 288.2 (2003), pp. 34–41.

[169] SC Wilks et al. “Energetic proton generation in ultra-intense laser–solid interactions”. In: *Physics of plasmas* 8.2 (2001), pp. 542–549.

[170] Erich S Weibel. “Spontaneously growing transverse waves in a plasma due to an anisotropic velocity distribution”. In: *Physical Review Letters* 2.3 (1959), p. 83.

[171] M Nakatsutsumi et al. “Self-generated surface magnetic fields inhibit laser-driven sheath acceleration of high-energy protons”. In: *Nature communications* 9.1 (2018), p. 280.

[172] T Wang et al. “Structured targets for detection of Megatesla-level magnetic fields through Faraday rotation of XFEL beams”. In: *Physics of plasmas* 26.1 (2019), p. 013105.

[173] HG Rinderknecht et al. “Relativistically transparent magnetic filaments: scaling laws, initial results and prospects for strong-field QED studies”. In: *New Journal of Physics* 23.9 (2021), p. 095009.

[174] Luke Ceurvorst et al. “Mitigating the hosing instability in relativistic laser-plasma interactions”. In: *New Journal of Physics* 18.5 (2016), p. 053023.

[175] IY Dodin and NJ Fisch. “Correction to the Alfvén-Lawson criterion for relativistic electron beams”. In: *Physics of plasmas* 13.10 (2006), p. 103104.

[176] Yutaka Ohira et al. “Two-dimensional particle-in-cell simulations of the non-resonant, cosmic-ray-driven instability in supernova remnant shocks”. In: *The Astrophysical Journal* 698.1 (2009), p. 445.

[177] Xue-Ning Bai et al. “Magnetohydrodynamic-particle-in-cell method for coupling cosmic rays with a thermal plasma: application to non-relativistic shocks”. In: *The Astrophysical Journal* 809.1 (2015), p. 55.

[178] Hui Liu et al. “Particle-in-cell simulation of a Hall thruster”. In: *Journal of Physics D: Applied Physics* 43.16 (2010), p. 165202.

[179] P Coche and L Garrigues. “A two-dimensional (azimuthal-axial) particle-in-cell model of a Hall thruster”. In: *Physics of Plasmas* 21.2 (2014), p. 023503.

[180] Agustin F Lifschitz et al. “Particle-in-cell modelling of laser–plasma interaction using Fourier decomposition”. In: *Journal of Computational Physics* 228.5 (2009), pp. 1803–1814.

[181] Victor Malka et al. “Laser-driven accelerators by colliding pulses injection: A review of simulation and experimental results”. In: *Physics of Plasmas* 16.5 (2009), p. 056703.

[182] A Pukhov and J Meyer-ter-Vehn. “Relativistic laser-plasma interaction by multi-dimensional particle-in-cell simulations”. In: *Physics of Plasmas* 5.5 (1998), pp. 1880–1886.

[183] J Meyer-ter-Vehn. “Fast ignition of ICF targets: an overview”. In: *Plasma physics and controlled fusion* 43.12A (2001), A113.

[184] A Pukhov and J Meyer-ter-Vehn. “Laser hole boring into overdense plasma and relativistic electron currents for fast ignition of ICF targets”. In: *Physical review letters* 79.14 (1997), p. 2686.

[185] Oscar Buneman. “Dissipation of currents in ionized media”. In: *Physical Review* 115.3 (1959), p. 503.

[186] John Dawson. “One-dimensional plasma model”. In: *The Physics of Fluids* 5.4 (1962), pp. 445–459.

[187] Alexander Pukhov. “Particle-in-cell codes for plasma-based particle acceleration”. In: *arXiv preprint arXiv:1510.01071* (2015).

[188] John M Dawson. “Particle simulation of plasmas”. In: *Reviews of modern physics* 55.2 (1983), p. 403.

[189] Charles K Birdsall. “Particle-in-cell charged-particle simulations, plus Monte Carlo collisions with neutral atoms, PIC-MCC”. In: *IEEE Transactions on plasma science* 19.2 (1991), pp. 65–85.

[190] Charles K Birdsall and A Bruce Langdon. *Plasma physics via computer simulation*. CRC press, 2004.

[191] David Tskhakaya et al. “The Particle-In-Cell Method”. In: *Contributions to Plasma Physics* 47.8-9 (2007), pp. 563–594.

[192] Kane Yee. “Numerical solution of initial boundary value problems involving Maxwell’s equations in isotropic media”. In: *IEEE Transactions on antennas and propagation* 14.3 (1966), pp. 302–307.

[193] A Bruce Langdon. “Effects of the spatial grid in simulation plasmas”. In: *Journal of Computational Physics* 6.2 (1970), pp. 247–267.

[194] Roger W Hockney and James W Eastwood. *Computer simulation using particles*. crc Press, 2021.

[195] Charles K Birdsall and Dieter Fuss. “Clouds-in-clouds, clouds-in-cells physics for many-body plasma simulation”. In: *Journal of Computational Physics* 3.4 (1969), pp. 494–511.

[196] Karl S Kunz and Raymond J Luebbers. *The finite difference time domain method for electromagnetics*. CRC press, 1993.

[197] Che Ting Chan, QL Yu, and KM Ho. “Order-N spectral method for electromagnetic waves”. In: *Physical Review B* 51.23 (1995), p. 16635.

[198] Jay P Boris et al. “Relativistic plasma simulation-optimization of a hybrid code”. In: *Proc. Fourth Conf. Num. Sim. Plasmas*. 1970, pp. 3–67.

[199] Ernst Hairer et al. “Geometric numerical integration”. In: *Oberwolfach Reports* 3.1 (2006), pp. 805–882.

[200] Yasuhiko Sentoku and Andreas J Kemp. "Numerical methods for particle simulations at extreme densities and temperatures: Weighted particles, relativistic collisions and reduced currents". In: *Journal of computational Physics* 227.14 (2008), pp. 6846–6861.

[201] F Pérez et al. "Improved modeling of relativistic collisions and collisional ionization in particle-in-cell codes". In: *Physics of Plasmas* 19.8 (2012), p. 083104.

[202] A Gonoskov et al. "Extended particle-in-cell schemes for physics in ultrastrong laser fields: Review and developments". In: *Physical review E* 92.2 (2015), p. 023305.

[203] Marija Vranic et al. "Particle merging algorithm for PIC codes". In: *Computer Physics Communications* 191 (2015), pp. 65–73.

[204] R Nuter et al. "Field ionization model implemented in particle in cell code and applied to laser-accelerated carbon ions". In: *Physics of Plasmas* 18.3 (2011), p. 033107.

[205] Roland Duclous, John G Kirk, and Anthony R Bell. "Monte Carlo calculations of pair production in high-intensity laser–plasma interactions". In: *Plasma Physics and Controlled Fusion* 53.1 (2010), p. 015009.

[206] Mathieu Lobet et al. "Generation of high-energy electron-positron pairs in the collision of a laser-accelerated electron beam with a multipetawatt laser". In: *Physical Review Accelerators and Beams* 20.4 (2017), p. 043401.

[207] D Wu et al. "Particle-in-cell simulations of laser-plasma interactions at solid densities and relativistic intensities: the role of atomic processes". In: *High Power Laser Science and Engineering* 6 (2018), e50.

[208] Stephen M Seltzer and Martin J Berger. "Bremsstrahlung spectra from electron interactions with screened atomic nuclei and orbital electrons". In: *Nuclear Instruments and Methods in Physics Research Section B: Beam Interactions with Materials and Atoms* 12.1 (1985), pp. 95–134.

[209] Francesc Salvat, José M Fernández-Varea, and Josep Sempau. "PENELOPE-2006: A code system for Monte Carlo simulation of electron and photon transport". In: *Workshop proceedings*. Vol. 4. 6222. Citeseer. 2006, p. 7.

[210] Y Sentoku et al. "Particle simulation on x-ray emissions from ultra-intense laser produced plasmas". In: *Physics of Plasmas* 5.12 (1998), pp. 4366–4372.

[211] Tao Wang. *Kinetic modelling of enhanced electron acceleration and gamma-ray emission in high-power laser interactions with structured targets*. University of California, San Diego, 2020.

[212] R Ward and NJ Sircombe. “Fast particle Bremsstrahlung effects in the PIC code EPOCH: enhanced diagnostics for laser-solid interaction modelling”. In: *Technical Report* (2014).

[213] Archana Sampath. “Strong-field QED and collisional effects in electron beam-plasma interaction”. PhD thesis. Ruprecht-Karls-Universität Heidelberg, 2020.

[214] Warwick Plasma Physics Group. *EPOCH Manuals*. Accessed: 2023-05-12. 2023. URL: `https://github.com/Warwick-Plasma/EPOCH_manuals.git`.

[215] George B Rybicki and Alan P Lightman. *Radiative processes in astrophysics*. John Wiley & Sons, 1991.

[216] John David Jackson. *Classical electrodynamics*. 1999.

[217] HW Koch and JW Motz. “Bremsstrahlung cross-section formulas and related data”. In: *Reviews of modern physics* 31.4 (1959), p. 920.

[218] RL Gluckstern and MH Hull Jr. “Polarization dependence of the integrated bremsstrahlung cross section”. In: *Physical Review* 90.6 (1953), p. 1030.

[219] Longhuan Kim and RH Pratt. “Numerical calculation of classical bremsstrahlung”. In: *Physical review A* 36.1 (1987), p. 45.

[220] Lev Davidovich Landau. *The classical theory of fields*. Vol. 2. Elsevier, 2013.

[221] Hans Bethe and Walter Heitler. “On the stopping of fast particles and on the creation of positive electrons”. In: *Proceedings of the Royal Society of London. Series A, Containing Papers of a Mathematical and Physical Character* 146.856 (1934), pp. 83–112.

[222] Yung-Su Tsai. “Pair production and bremsstrahlung of charged leptons”. In: *Reviews of Modern Physics* 46.4 (1974), p. 815.

[223] Lev Davidovich Landau and II Pomeranchuk. “The limits of applicability of the theory of bremsstrahlung by electrons and of the creation of pairs at large energies”. In: *Dokl. Akad. Nauk SSSR*. Vol. 92. 1953, p. 535.

[224] Ulrik I Uggerhøj. “The interaction of relativistic particles with strong crystalline fields”. In: *Reviews of modern physics* 77.4 (2005), p. 1131.

[225] ML Ter-Mikaelian. “The interference emission of high-energy electrons”. In: *Zh. Eksp. Teor. Fiz* 25 (1953), p. 296.

[226] Vladimir N Baier and Valerij Mihajlovič Katkov. “Concept of formation length in radiation theory”. In: *Physics reports* 409.5 (2005), pp. 261–359.

[227] Peter Arnold and Shahin Iqbal. “The LPM effect in sequential bremsstrahlung”. In: *Journal of High Energy Physics* 2015.4 (2015), pp. 1–86.

[228] Christian Flohr Nielsen. "Elementary Particles and their Interaction with Strong Electromagnetic Fields". In: ().

[229] Mikhail Leonovich Ter-Mikaelian. *High-energy electromagnetic processes in condensed media*. 29. John Wiley & Sons, 1972.

[230] PL Anthony et al. "Measurement of dielectric suppression of bremsstrahlung". In: *Physical review letters* 76.19 (1996), p. 3550.

[231] Ajit Kumar. *Fundamentals of quantum mechanics*. Cambridge University Press, 2018.

[232] Analı´a Nilda Cillis et al. "Influence of the LPM effect and dielectric suppression on particle air showers". In: *Physical Review D* 59.11 (1999), p. 113012.

[233] Hans A Bethe. "Moliere's theory of multiple scattering". In: *Physical review* 89.6 (1953), p. 1256.

[234] VM Galitsky and II Gurevich. "Coherence effects in ultra-relativistic electron bremsstrahlung". In: *Il Nuovo Cimento (1955-1965)* 32 (1964), pp. 396–407.

[235] PL Anthony et al. "An accurate measurement of the Landau-Pomeranchuk-Migdal effect". In: *Physical Review Letters* 75.10 (1995), p. 1949.

[236] SR Klein et al. "A measurement of the LPM effect". In: *AIP Conference Proceedings*. Vol. 302. 1. American Institute of Physics. 1994, pp. 172–197.

[237] VN Baier and VM Katkov. "The Landau-Pomeranchuk-Migdal effect in a thin target". In: *arXiv preprint hep-ph/9712524* (1997).

[238] VN Baier and VM Katkov. "Theory of the landau-pomeranchuk-migdal effect". In: *Physical Review D* 57.5 (1998), p. 3146.

[239] BG Zakharov. "Fully quantum treatment of the Landau-Pomeranchik-Migdal effect in QED and QCD". In: *Journal of Experimental and Theoretical Physics Letters* 63 (1996), pp. 952–957.

[240] VN Baier and VM Katkov. "Landau-Pomeranchuk-Migdal effect and transition radiation in structured targets". In: *Physical Review D* 60.7 (1999), p. 076001.

[241] Todor Stanev and HP Vankov. "Nature of the highest energy cosmic rays". In: *Physical Review D* 55.3 (1997), p. 1365.

[242] M Takeda et al. "Extension of the cosmic-ray energy spectrum beyond the predicted Greisen-Zatsepin-Kuz'min cutoff". In: *Physical Review Letters* 81.6 (1998), p. 1163.

[243] P Auger Collaboration1CRICyT Mendoza et al. “LPM effect and pair production in the geomagnetic field: a signature of ultra-high energy photons in the Pierre Auger Observatory”. In: *Astroparticle Physics* 14.2 (2000), pp. 121–130.

[244] AA Lagutin, RI Raikin, and TL Serebryakova. “Air shower universality from 1014 to 1022 eV”. In: *Journal of Physics: Conference Series*. Vol. 409. 1. IOP Publishing. 2013, p. 012092.

[245] Tatyana Serebryakova et al. “Lateral distributions of electrons in air showers initiated by ultra-high energy gamma quanta taking into account LPM and geomagnetic field effects”. In: *Journal of Physics: Conference Series*. Vol. 1181. 1. IOP Publishing. 2019, p. 012088.

[246] Mikhail Leonovich Ter-Mikaelian. *High-energy electromagnetic processes in condensed media*. 29. John Wiley & Sons, 1972.

[247] PL Anthony et al. “Bremsstrahlung suppression due to the Landau-Pomeranchuk-Migdal and dielectric effects in a variety of materials”. In: *Physical Review D* 56.3 (1997), p. 1373.

[248] V Anguelov and H Vankov. “Electromagnetic showers in a strong magnetic field”. In: *Journal of Physics G: Nuclear and Particle Physics* 25.8 (1999), p. 1755.

[249] S Kawaguchi et al. “Behavior of individual electromagnetic cascade shower with the LPM effect in geomagentic field”. In: *International Cosmic Ray Conference*. Vol. 2. 2001, p. 470.

[250] RA Becker-Szendy et al. *Quantum-mechanical suppression of bremsstrahlung*. Tech. rep. P00020893, 1993.

[251] Feng Wan et al. “Photon emission by bremsstrahlung and nonlinear Compton scattering in the interaction of ultraintense laser with plasmas”. In: *The European Physical Journal D* 71 (2017), pp. 1–8.

[252] Michael Peskin. *An introduction to quantum field theory*. CRC press, 2018.

Acknowledgement

Finally, I would like to express my heartfelt gratitude and appreciation to the following individuals who have contributed significantly to the completion of this Ph.D. thesis:

First and foremost, I am deeply indebted to my supervisor, PD. Toma Toncian, for his invaluable guidance and support throughout the entire research journey. Their expertise, insightful feedback, and patience have been instrumental in shaping this work.

I am also grateful to Prof. Dr. Thomas E. Cowan for my support in HZDR and to Dr. Ulf Zastrau for hosting me at the HED group in EuXFEL. As well as to Prof. Alexey Arefiev for his valuable contributions, insightful discussions, and constructive feedback. Their expertise and guidance have enriched this research and provided valuable perspectives.

I would like to extend my sincere appreciation to my friends and colleagues (Dr. Pouneh Saffari, Dr. Zheng Gong, and Dr. Lingen Huang) who have supported me along the way. Their stimulating conversations, encouragement, and willingness to assist have been truly invaluable.

Last but certainly not least, I am forever grateful to my loving wife, Forough, and our precious daughter, Hannah. Their unwavering love, patience, and understanding have sustained me throughout this challenging journey. Their belief in me and their constant support has been my greatest source of strength.

I am indebted to all those who have played a part, big or small, in making this thesis possible. Your contributions have been vital, and I am honored to have had the privilege to work with and learn from each and every one of you.